New discoveries in liquid drop impacts

by

Li Zhang

A dissertation submitted in partial fulfillment
of the requirements for the degree of
Doctor of Philosophy
(Physics)
in The University of Michigan
2012

Doctoral Committee:

Assistant Professor Robert D. Deegan, Chair
Professor Charles R. Doering
Professor Mark E. Newman
Professor Marc Perlin
Professor William W. Schultz

The knowledge of all things is possible. —Leonardo da Vinci

To Flora

ACKNOWLEDGEMENTS

I want to show gratitude to those who helped shape this dissertation. First I would like to thank my advisor Dr. Robert D. Deegan who taught me many invaluable lessons as a scientist and a friend. The skills I acquired under his guidance will undoubtedly benefit me in the future. I want to thank other members on my dissertation committee who took a valuable portion of time and effort going through my treatise.

I need to mention Jonathon Koss for creating user-friendly programs and data processing for my project. Thanks goes to Jameson Toole for paving the foundation of certain research areas. An integral part of my research was conducted at the Advanced Photon Source (APS) of Argonne National Laboratory, in collaboration with research scientist Dr. Kamel Fazzaa. I much appreciate his sacrificed weekends and some great ideas. Claudio Falcon helped me with some data acquisition that deserves recognition.

Last but not least, I want to thank my friends here in the Ann Arbor area and my family half a world away for supporting me in various ways. This dissertation is dedicated to Flora for changing me in a good way.

TABLE OF CONTENTS

DEDICATION ii

ACKNOWLEDGEMENTS iii

LIST OF FIGURES vii

LIST OF TABLES xvi

LIST OF APPENDICES xvii

CHAPTER

I. Introduction 1

1.1 History and applications 1
1.1.1 Historic overview 1
1.1.2 Applications 3
1.2 Physics of liquid drop impacts 4
1.2.1 Compressible phase and continuum model 4
1.2.2 Governing equations 5
1.2.3 Parametrization of the problem 8
1.2.4 Instabilities 10
1.3 Phenomenology of liquid drop impacts 12
1.3.1 Diversities and generalities 12
1.3.2 Dry substrate impact 13
1.3.3 Wet substrate impact 18
1.4 Approaches to the problem 31
1.4.1 Analytical solutions 31
1.4.2 Numerical simulations 33
1.4.3 Experimental methods 36
1.5 Outline of the thesis 38

II. X-ray studies on liquid drop impacts 41

2.1 Introduction . . . 41
2.2 Experimental setup . . . 43
2.3 Procedure for data processing . . . 44
2.4 Limitations of the method . . . 48
2.5 Dynamics of lamella . . . 50
2.5.1 Crown radius . . . 50
2.5.2 Base radius . . . 51
2.5.3 Thickness of lamella . . . 52
2.5.4 Velocity of lamella . . . 55
2.6 Miscellaneous studies . . . 59
2.6.1 Instability on ejecta sheet . . . 59
2.6.2 Bubble trapped under drop . . . 60
2.6.3 Interface between liquid drop and layer . . . 60
2.6.4 Particle image velocimetry . . . 60

III. Wavelength selection in crown splash . . . 64

3.1 Introduction . . . 64
3.2 Experimental Methods . . . 66
3.3 Experimental Results . . . 71
3.3.1 Splash morphologies . . . 71
3.3.2 Crown splashes . . . 71
3.4 Rayleigh-Plateau Instability . . . 76
3.5 Other Mechanisms . . . 84
3.5.1 Rayleigh-Taylor Instability . . . 84
3.5.2 Richtmyer-Meshkov Instability . . . 87
3.5.3 Nonlinear Instabilities . . . 87
3.6 Discussion & Conclusion . . . 87

IV. Parametric studies on liquid drop impacts onto a deep pool 90

4.1 Introduction . . . 90
4.2 Experimental System . . . 91
4.3 Experimental results . . . 93
4.3.1 Phenomenology of the ejecta sheet . . . 93
4.3.2 Dynamics of the ejecta sheet . . . 96
4.3.3 Secondary Droplets . . . 100
4.4 Conclusions . . . 101

V. Effects of ambient gas pressure on liquid drop impacts . . . 103

5.1 Introduction . . . 103
5.2 Experimental Setup . . . 104
5.3 Results . . . 105
5.3.1 Boundary shifts in phase diagram . . . 105

5.3.2 Formation of ejecta sheet . . . 105
5.3.3 Instability of ejecta sheet . . . 106
5.3.4 Interaction between ejecta sheet and lamella . . . 109
5.3.5 Crown splash . . . 111
5.3.6 Aerodynamics of ejecta sheet . . . 112
5.4 Discussions . . . 113

VI. Inadequacy of conventional scaling . . . 115

6.1 Introduction . . . 115
6.2 Experimental Setup . . . 116
6.3 Results & Discussion . . . 118
6.3.1 Inadequacy of conventional scaling . . . 118
6.3.2 Role of the surrounding gas . . . 122
6.3.3 The trapped disk of gas . . . 124
6.3.4 Connection between gas disk and ejecta . . . 125
6.3.5 Multiplicity of jets . . . 128
6.4 Conclusions . . . 128

VII. Conclusion . . . 129

APPENDICES . . . 132

BIBLIOGRAPHY . . . 138

LIST OF FIGURES

Figure

1.1 Various drop impacts: a: Deformation of a water drop falling on a solid substrate. Drawing in the margin of folio 33r in the Codex Hammer (previously Codex Leicester,1506—1510) by Leonardo da Vinci (1508), who noted the axisymmetry of the impacted drop imprint pattern. Radial fingers are also visible. b: The famous Edgerton′s photograph (circa 1937) of milk drops. Courtesy of Harold & Ester Edgerton Foundation and Palm Press, Inc. c: "Permanent splashes" left where a projectile has entered an Armour-Plate. From *Worthington* [1908]. d: Meteor crater near Flagstaff, Arizona 2

1.2 Illustration of several linear instabilities. a: Rayleigh-Plateau instability, b: Rayleigh-Taylor instability, c: Kelvin-Helmhotlz instability. 11

1.3 Morphology of drop impact on a dry surface. From *Rioboo et al.* [2001]. Courtesy of Begell House. 13

1.4 Left: Morphology of wet substrate impact, a: crown splash, b,c: crown splash & microdroplet splash, d: no splash, e: microdroplet splash, Right: Phase diagram indicating the qualitatively different regimes of drop impact with $h = 0.2$. Adapted from *Deegan et al.* [2008] 19

1.5 Outcomes of a drop impact on a wetted solid surface. a: deposition without formation of crown, b: formation of crown without break-up, c: splashing without crown, d: splashing with crown. Adapted from: *Rioboo et al.* [2003] 20

1.6 a: Time evolution of lamella viewed from an angle above substrate, scale bar: 1mm, b: A cartoon of cross section through impact center. 1, residual top of impacting drop; 2, wall; 3, section of lamella propagating outward; 4, cross-section of free rim; 5, liquid layer on wall. 22

1.7 Left: comparison between thin layer (a, $h = 0.05$) and thick layer (b, $h = 0.5$) from *Wang and Chen* [2000]. Right: Worthington jet after impact on a deep liquid pool (c, $h \gg 1$), adapted from *Worthington* [1908] 24

1.8 a: Ejecta sheet predicted by *Weiss and Yarin* [1999] at We=2000 and $h = 0.125$. The different curves correspond to various times after impact. b: Ejecta sheet observed by *Thoroddsen* [2002] at We=4170, Re=1080 long before lamella formation. Scale bar: 1 mm c: Ejecta sheet breaking into microdroplets. Scale bar: 0.5 mm. 26

1.9 Left: Sketch of the rim bounding a sheet; Right: various scenarios of secondary droplets generated from rim of lamella 29

1.10 a: Spreading ethanol drops stroboscopically illuminated for a single drop. b: Splashing ethanol drops illuminated by a single flash for a train of impacting drops. From *Yarin and Weiss* [1995] 36

1.11 Images from optical (left) and X-ray (right) technique on same impact. 38

2.1 Comparison between optical images (left) and X-ray images (right). Scale bar: 1 mm for optical images, 100 μm for X-ray images. . . . 42

2.2 Experimental setup for X-ray phase contrast imaging on drop impact 44

2.3 Original images (left) and grids on extracted profiles (right) for same impact at different times showing backbone (blue) and ribs (red), impact axis shifted to better illustrate definition of crown radius and base radius. 45

2.4 Obtaining the backbone and the ribs. a: Extracted profile with four selected points, b: SC mapping turns every point inside original profile into a rectangle and four points into vertices, c: A uniform grid put onto the rectangle, d: Grid mapped back to original space via reverse SC mapping. Solid blue: backbone; Solid red: ribs 46

2.5 Left: meniscus effect extends outside frame, blue solid line represents original layer surface, curve due to meniscus is ignored beyond the location indicated by white arrow. Right: amplified top portion of the lamella with overshooting fringes (black arrow), blue dashed line indicates our choice of liquid-air boundary. 48

2.6 Dimensionless crown radius r_c/D fit to Equation 2.5 at four different dimensionless depths for each velocity: 0.1 (circles), 0.2 (squares), 0.4 (stars) and infinity (diamonds) with pre-factor C in the box. Solid line is the best fit 52

2.7 Dimensionless base radius r_b/D fit to Equation 2.7 and scaled by pre-factor B (value shown in the box) at four different velocities. Four dimensionless depths h for each velocity: 0.1 (circles), 0.2 (squares), 0.4 (stars) and infinity (diamonds). Solid line represents $\tilde{t}^{0.4}$ 53

2.8 Dimensionless thickness of lamella δ/D at $y0 = 0.02$ cm at four different velocities . Four dimensionless depths h for each velocity: 0.1 (circles), 0.2 (squares), 0.4 (stars) and infinity (diamonds). 54

2.9 Procedure for finding velocity at an arbitrary location on lamella . . 55

2.10 First row: profiles of lamella at different times after impact for $U =$ 175 cm/s, $Re = 520$, $We = 250$ and $h = 0.2$ with backbone. Second to fifth row: horizontal (v_r)velocity, vertical (v_z) velocity, velocity component parallel to the backbone (v_{para}) and velocity component perpendicular to the backbone (v_{perp}) at various arc lengths. Red dots represent the same set in a column. 57

2.11 Dimensionless velocity of the base v_b/U fit to Equation 2.7 and scaled by pre-factor E (value shown in the box) at four different velocities . Four dimensionless depths h for each velocity: 0.1 (circles), 0.2 (squares), 0.4 (stars) and infinity (diamonds). Solid line represents $\tilde{t}^{-0.6}$ 58

2.12 Development of instability on ejecta sheet from impact between liquid drop of water-glycerol mixture and a deep pool of same liquid at velocity $U = 190$ cm/s, $D = 0.2463$ cm, $Re = 3764$ and $We = 142$. Scale bar:100 microns 59

2.13 Left: X-ray images of bubble trapped underneath drop of water-glycerol mixture impacting a deep pool of same liquid. $U = 190$ cm/s, $D = 0.2463$ cm, $Re = 3764$ and $We = 142$. Scale bar:100 microns; Right: optical images of bubble from *Thoroddsen et al.* [2003], $U = 49$ cm/s, $D = 0.424$ cm, $Re = 138$ and $We = 14$. Scale bar: 500 microns 61

2.14 Interface (black arrow) between two fluids after a drop of SO1 of diameter $D = 0.1645$ cm hitting a deep liquid pool of SO2 at velocity $U = 220$ cm/s . Scale bar:100 microns 62

2.15 Drop impacts with particles for PIV measurement. White arrow indicates a trackable particle. Scale bar:100 microns 63

3.1 Crown splash (silicon oil: $Re = 966$, $We = 874$, $h = 0.2$). 67

3.2 Apparatus for observing the evolution of crown splashes. A drop forms and detaches from a hypodermic needle held a fixed height above a thin layer of the same liquid. The needle is gravity fed from a reservoir. As the drop falls towards the liquid layer, it interrupts a laser sheet focused onto a photodetector which initiates a countdown on a delay generator. After a preprogrammed time, the delay generator fires a flash onto a diffusion screen, and a back-lit image of the impact event is recorded from below through the transparent substrate or from the side. 68

3.3 Crown splash ($Re = 894, We = 722$, & $h = 0.1$) from below at $t = 1.85$ ms and $t = 3.15$ ms after impact showing the one-to-one correspondence between instability wavelength and the number of droplets. The arrows define rim radius as seen from below r_o^B and rim's radial distance from the impact center R. 70

3.4 *Left:* Images illustrating the crown sheet at 250 and 2100 μs after impact. *Right:* Cartoon of sheet cross-section. At early times, the leading edge of the sheet is almost horizontal. The shape changes as the rim retracts relative to the fluid (though still moving away from the center in the laboratory frame) and entrains the fluid in the sheet. Eventually the entire flat portion of the sheet is entrained in the rim. The kink in the late time sheet is a wave generated when the rim reaches the vertical section of the sheet. Scale bar equals 2 mm. . . 70

3.5 Qualitative character of impact for $h = 0.2$. No splash (black small circles), crown droplets with (open circles) and without (squares) microdroplets, and microdroplets without crown droplets (diamonds). The filled squares indicates the parameter set for all experiments at $h = 0.2$ reported here. Spatially periodic crown splashes form exclusively in the Crown droplets regime. 72

3.6 Morphologies of splashes outside of the crown splash regime: (a) water ($Re = 6044$, $We = 254$, $h = 0.2$) produces a highly irregular crown sheet and splash (b) glycerol/water mixture ($Re = 2566$, $We = 314$, $h = 0.2$) produces droplets immediately upon impact, long before the crown sheet forms, (c) silicon oil ($Re = 1392$, $We = 1266$, $h = 0.2$) produces a trapped torus of air (d) isopropanol for $Re = 1354$, $We = 406$, $h = 0.2$ produces a wavy crown sheet and continuously ejects droplets as the crown grows upward. 73

3.7 Profiles of the outer rim corrugation at successive times (from bottom to top: 115, 365, 605, 1105, 1605, 2085 μs after impact), starting from a smooth profile and growing to a highly corrugated state. Note that the corrugation nucleates at different places and these domains merge at later times. The noise on the early time profiles are digitization artifacts: the camera pixel size is 6.0 μm. 74

3.8 Normalized power spectra versus wavenumber for various times after impact for parameter set number 1. The solid curve is the average of multiple experiments and the dashed curve is the prediction from the Rayleigh-Plateau model. The peaks at low wavenumber arise from digitization effects and small non-parallelism of the camera sensor and the impact plane; for example, the largest of these peaks corresponds to the $m = 2$ mode. 75

3.9 I: An undisturbed straight liquid cylinder with uniform radius r and stream radius $S = \infty$, II: A slightly perturbed (exaggerated drawing) liquid cylinder with r and S dependent on local geometry. 77

3.10 Peak wavelength (*top*) and power (*bottom*) versus time: measured (circles) and the predicted values from the Rayleigh-Plateau (solid line,squares) and the Rayleigh-Taylor (dashed line) models for parameter set number 1. 80

3.11 Horizontal distance of the rim from the impact center (top) and radius of the rim (bottom) measured from below (circles) and from side (squares) versus time for parameter set number 1. The solid line is a cubic spline of the side data and the dashed line is the geometric mean of the rim radius r_o. 82

3.12 Ratio of measured to theoretically expected peak wavelength versus time for the Rayleigh-Plateau model for all experiments: number 1 (hexagons), number 2 (circles), number 3 (stars), number 4 (diamonds), number 5 (squares), number 6 (triangles). Note that the most accurate data is for parameter set number 1. 83

3.13 Acceleration (top) measured from the trajectory of the rim and inverse Bond number (bottom) versus time. For most of the splash inverse Bond number is large compared to one, indicating the dominant role of capillarity over inertial forces. 86

4.1 X-ray phase contrast images of splash at (a) $We = 396$ & $Re = 5703$ with 0.65 cSt silicone oil, (b) $We = 324$ & $Re = 2191$ with 1.5 cSt silicone oil, and (c) $We = 451$ & $Re = 710$ with 5 cSt silicone oil. (a) & (b) show a thin jet (the ejecta sheet) and a thicker jet (the lamella sheet). (c) shows the ejecta sheet and lamella sheet combined into a single contiguous sheet. Note that the leading edge of all jets are engorged due to Taylor-Culick contraction. The wayward halo departing from the lamella in (b) is an example of an artifact produced by the phase contrast technique. 93

4.2 Time evolution of jets for (a) $Re = 1330$, $We = 117$; (b) $Re = 1511$, $We = 282$; (c) $Re = 2931$, $We = 256$; (d)$Re = 4975$, $We = 735$. These parameters are plotted in Fig 4.3 with an unfilled circle, square, star and diamond, respectively. The time after impact is given in the lower righthand corner of each image and the scale bar the is given in the first panel of (a). The black corresponds to the fluid. The various white patches are lighting artifacts. 94

4.3 Phase diagram as a function of We and Re indicating number of jets resulting from drop impact. The behavior of each experiment is indicated with a symbol: circles for a non-cresting capillary, squares for a single jet comprised of both the ejecta sheet and lamella sheet, stars for separate ejecta sheet and lamella, and diamonds for separate ejecta sheet and lamella when the ejecta sheet dissociates into secondary droplets. Unfilled symbols correspond to the particular experiments depicted in Fig 4.2. 95

4.4 Example of the radial r and vertical z position of the ejecta sheet versus time, and the procedure for determining the emergence time t_j. The data for the position of the leading edge plotted versus time after impact (circles) were fit to a parabola (solid line). The speed of the jet was determined by from the derivative of the fit, and plotted in the (c) with a (red) solid line. The speed of the front for the particular impact speed (see Appendix A) is plotted with a (blue) dashed line. The intersection of the front and jet speed was taken as the emergence time. 97

4.5 The emergence time t_j, radial position r_j, and speed u_j of the ejecta sheet plotted versus impact velocity. Symbols correspond to different fluids: red circles for SO1 (0.49 cP), green diamond for SO2 (0.82 cP), blue square for SO3 (1.3 cP), pink triangles for SO4 (2.7 cP). The error bars represent the variability of the data for a fixed set of parameters which is primarily due to the uncertainty in time of first contact between the drop the layer. 98

4.6 (a & b) Scaled emergence time t_j and speed u_j versus impact speed U plotted on a log-log scale. The solid lines are fits to power laws which yield exponents of -2.6 and 1.8, respectively. (c) Mean radius dictated by mass balance versus the emergence position, both scaled by the radius of the drop. 99

4.7 Multiple generations of emitted microdroplets from a single impact event for 0.65Cst silicone oil at $We = 798$ & $Re = 8019$ in a reduced pressure environment (0.17 atm) at 60, 100, 500, 700 μs after impact with earliest time at top. 101

5.1 Overlapped phase diagrams from various We-Re combinations in vacuum(blue) and air(red). Solid lines are approximate boundaries separating various regimes. 106

5.2 X-ray images showing neck region between impacting SO1 drop with diameter $D = 0.18$ cm and a deep pool in atmosphere. a: with a lower velocity a bulge forms ($We = 160$, $Re = 3740$), b: with a higher velocity ejecta sheet forms ($We = 210$, $Re = 4200$), c: with even higher velocity ejecta sheet corrugates and eventually folds back to impacting drop ($We = 470$, $Re = 6400$). The scale bar: 100 μm. 107

5.3 Comparison between splash of SO1 drops of $D = 0.17$ cm in normal(a,c,e) and reduced(b,d,f) pressure at three impact speed and dimensionless time $\tilde{t} = 0.2$ and $\tilde{t} = 0.5$. (a)(b): $U = 165$ cm/s, $We = 220$, $Re = 4200$ (c)(d): $U = 270$ cm/s, $We = 600$, $Re = 7000$ (e)(f): $U = 320$ cm/s, $We = 850$, $Re = 8500$. The scale bar stands for 0.5 mm. 108

5.4 Duality of experimental results in atmosphere: a,b have same impact condition: $D = 0.18$ cm, $U = 284$ cm/s, $We = 700$, $Re = 7800$. The scale bar is 100 microns. 110

5.5 Microdroplets (marked as 1) and droplets from lamella (marked as 2) in a: atmosphere and b: partial vacuum. Impact velocity $U = 320$ cm/s, drop diameter $D = 0.17$cm, $We = 800$, $Re = 8000$ and $\tilde{t} = 1$. scale bar: 1 mm. 111

5.6 Crown splashes created by SO6 with same drop diameter $D = 0.18$ cm, dimensionless layer depth $h = 0.16$ and impact velocity $U = 320$ cm/s at $We = 880$, $Re = 1170$ in normal air pressure(a) and reduced air pressure(b).The scale bars stand for 0.5 mm. 112

6.1 Optical images of drop impact with (a) a glycerol-water mixture at $Re = 5450$, $We = 330$ and (b) a low viscosity silicone oil at $Re = 5330$, $We = 340$ at the indicated normalized time $\tilde{t} = Ut/D$. Despite almost identical experimental conditions the event in (a) produces a splash of microdroplets (solid arrows) and intermediate droplets (dashed arrows), while the event in (b) produces no secondary droplets. The images are scaled to equal drop diameters ($D = 0.22$ cm and $D = 0.18$ cm for the GW and SO, respectively), i.e. to the same non-dimensional length scale. 119

6.2 (a) Reynolds number threshold for onset of splashing, defined as the appearance of secondary droplets, in GW (red circles) and SO (blue diamonds) versus density of the surrounding gas. These data correspond to helium, air and SF_6 going from left to right. (b) Reynolds number threshold for onset of instability in GW (circles) and SO (diamonds) versus density of the surrounding gas. Note: the symmetry-breaking criterion gives a lower threshold than splashing criterion because at lower values of Re the ejecta is reabsorbed before the instability produces fragmentation. 120

6.3 Ejecta sheet emerging from the neck connecting a drop (dark gray) and the pool (black) for (a) GW at $Re = 4540$, $We = 230$ and (b) SO at $Re = 4430$, $We = 230$ at the indicated scaled time $\tilde{t} = Ut/D$. The images are scaled to equal drop diameters ($D = 0.22$ cm and $D = 0.18$ cm for the GW and SO, respectively). The scale bars correspond to 100 μm. The X-rays are highly attenuated after traversing the full width of the pool and thus the pool appears as a black band at the bottom of each image. 121

6.4 (a) Reynolds number threshold determined optically versus viscosity contrast for GW (red circle), pyridine (green triangle) and SO (blue diamond) in air at 1 atm. (b) Maximum disk radius normalized by the drop radius versus Stokes number for GW (red circles), Pyridine (green triangles) and SO (blue diamonds). The dashed curve is the best fit to power law which yields and exponent of 0.5. Note: R_b increases with Λ. 125

6.5 (a) Example of ejecta thickness measurement. (b) Thickness of ejecta sheet normalized by the drop radius versus Reynolds number for GW (red circles) and SO (blue diamonds). Note: the thickness is systematically larger for SO than GW at the same Re. Inset: same data plotted on a log-log scale. Dashed lines are best fits to a power law ARe^{α} which yield $A = 0.25 \times 10^{11}$ and $\alpha = -3.4$ for SO and $A = 1.3 \times 10^{11}$ and $\alpha = -3.6$ for GW. 126

6.6 X-Ray phase contrast images showing ejecta (1), secondary ejecta (2) and lamella (3) of GW splash at $We = 230$, $Re = 4540$ with scaled time $\tilde{t} = Ut/D$. The scales bars in (a) and (g) equal 100 μm. The sequences (a-f) and (g-j) are from different impact events with the same experimental conditions. Note: the primary ejecta sheet is present in only the first two frames before being absorbed into drop between frame (b) and (c) leaving the ripples on the drop surface visible i (c). The lamella comes out much later in frame (h). (a) $\tilde{t}$=0.13; (b) $\tilde{t}$=0.17; (c) $\tilde{t}$=0.21; (d) $\tilde{t}$=0.24; (e) $\tilde{t}$=0.28; (f) $\tilde{t}$=0.32; (g) $\tilde{t}$=0.34; (h) $\tilde{t}$=0.50; (i) $\tilde{t}$=0.66; (j) $\tilde{t}$=0.82. 127

A.1 Graphic illustrating the geometry of a sphere crossing a plane. When a drop collides with a liquid surface, the volume in region I is displaced. Provided the liquid substrate remains equal or above its initial flat configuration, which it does in our experiments, the minimum radius which can contain this volume is r_m. We call the edge of domain III the *front*. 133

B.1 Schematic of the gas as the drop approaches the pool when (a) the drop is far from pool and (b) the air squeezed between the two bodies causes the interfaces to distort. 135

LIST OF TABLES

Table

3.1 Parameters for experiments. 71

4.1 Physical properties of experimental fluids. 91

5.1 Physical properties of experimental fluids and value of Σ, Λ in air (1 atm) and vacuum (0.16 atm) 104

6.1 Physical properties of experimental fluids. 116

6.2 Physical properties of experimental gases. 117

6.3 *Re* threshold in air as determined with X-ray and optical imaging. . 122

LIST OF APPENDICES

Appendix

A. Illustration of a drop penetrating the layer 133

B. Estimation of the size of gas disk trapped between the drop and the liquid 135

CHAPTER I

Introduction

1.1 History and applications

1.1.1 Historic overview

In this dissertation I will discuss the drop impact problem in which a liquid drop impacts onto a solid or liquid layer. A common example is a rain drop that hits the ground or a water puddle and presents two features observable with naked eyes. First, a crater forms and expands outward from the center of impact; second, multiple droplets form off the crown. Qualitative studies on drop impact events date back to Leonardo da Vinci, who observed and recorded the deformation of a water drop falling on a solid substrate (Fig 1.1a). In the late 19th century, Worthington applied flash photography to the first systematic study of drop impacts; his book (*Worthington* [1908]) contains many fascinating photographs of this phenomena. *Edgerton and Killian* [1954] pioneered ultra-high-speed photography that laid the groundwork for modern experimental studies on drop impacts. In particular, Edgerton's photograph named "Milk Drop Coronet" (Fig 1.1b) shows both the formation of a crater and the generation of secondary droplets. *Harlow and Welch* [1964] developed the earliest numerical *Marker-and-Cell* (MAC) code to solve the full Navier-Stokes equations for a viscous, incompressible fluid and applied it to drop impact problems (*Harlow*

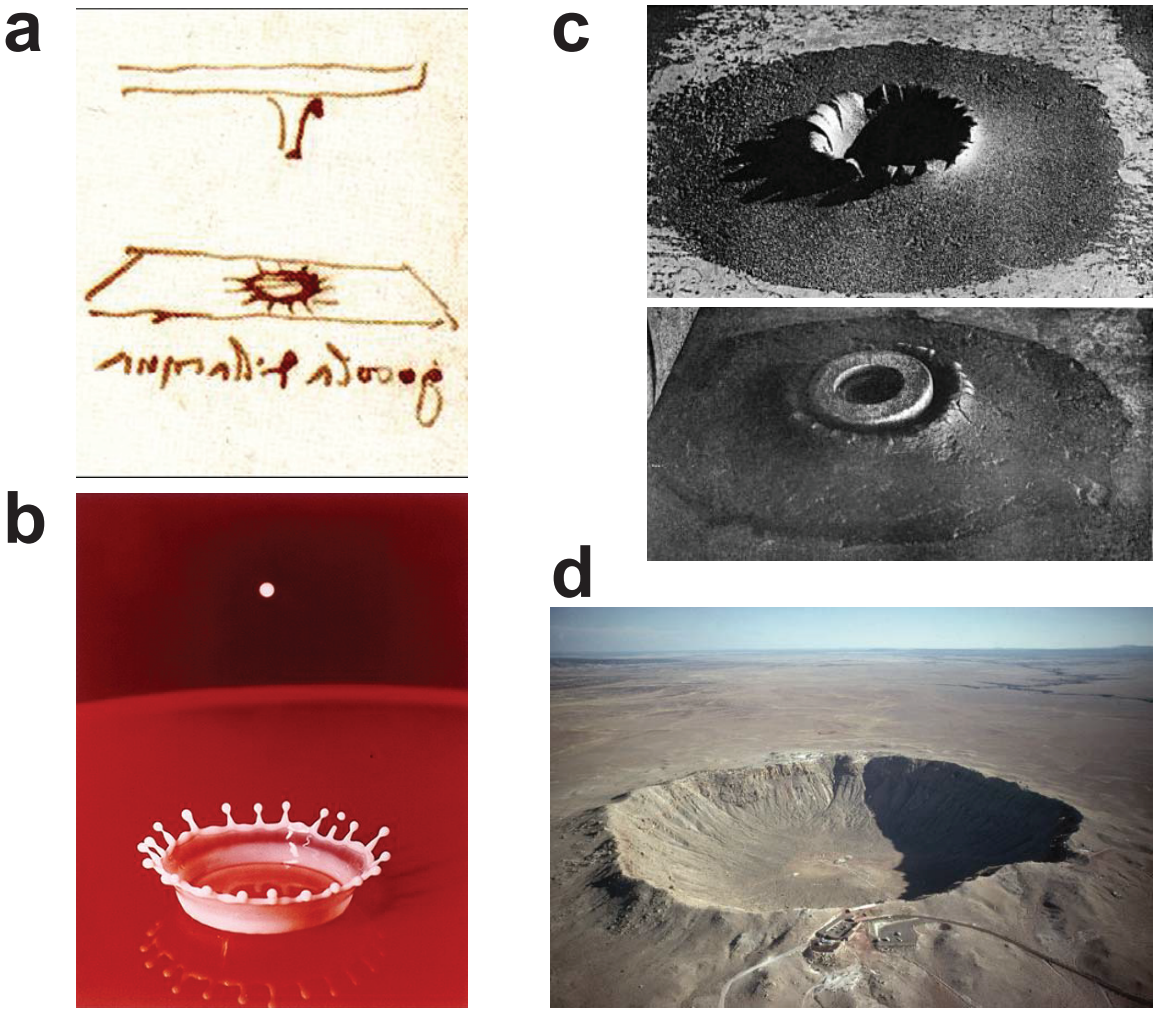

Figure 1.1: Various drop impacts: a: Deformation of a water drop falling on a solid substrate. Drawing in the margin of folio 33r in the Codex Hammer (previously Codex Leicester,1506—1510) by Leonardo da Vinci (1508), who noted the axisymmetry of the impacted drop imprint pattern. Radial fingers are also visible. b: The famous Edgerton′s photograph (circa 1937) of milk drops. Courtesy of Harold & Ester Edgerton Foundation and Palm Press, Inc. c: "Permanent splashes" left where a projectile has entered an Armour-Plate. From *Worthington* [1908]. d: Meteor crater near Flagstaff, Arizona

and Shannon [1967]). Since then, numerical studies on drop impacts have greatly advanced our understanding on the phenomenon in addition to fast- developing experimental techniques.

1.1.2 Applications

Recent years have seen many studies stimulated by an increasing need to understand drop impacts on solid and liquid surfaces. In the realm of engineering, spray cooling (*Pasandideh-Fard et al.* [2001]) is based on transferring heat from a hot substrate to impacting drops and can be found in sprinkler systems, cooling of turbine blades and quenching of metal castings. The manufacturing of flat displays relies on ink jet printing, where tiny polymer droplets of the size of a pixel impact on an impermeable solid substrate (*Van Dam and Le Clerc* [2004]). In agriculture, pesticide spraying (*Spillman* [1984]) requires knowledge of the spreading behavior of pesticide on foliage to reduce the quantity of pesticide applied per unit area. The prevention of soil erosion due to rain also demands understanding of liquid drop impacts (*Al-Durrah and Bradford* [1982]). In natural environments, rain drops on large water bodies trap and transfer air deep beneath the surface, which is crucial to the oxygen supply of the life forms within (*Wanninkhof et al.* [2009]). The bird's nest fungi use the force of falling water drops to liberate the spores from cup-shaped fruiting bodies (*Brodie* [1975]).

The physics behind drop impact applies to a wider range of materials than fluids. For example, when a solid projectile hits an armor plate in the hypervelocity range (approximately more than 3000 meters per second), solid materials flow like fluids, and the influence of their elasticity, yield stress and plasticity is negligible compared to inertial effects. In such a case, material is pushed from the contact region between the impacting projectile and the plate; a crater is also formed (Fig 1.1c). Its similarities to a classic splash scenario (such as a splash created by a rain drop) led Worthington to call it "permanent splash" . Such impacts are especially relevant in the field of space exploration, where hypervelocity impacts by space debris can result in anything from minor component degradation to complete destruction of a spacecraft. On a larger scale, the Arizona Meteor Crater was formed by a nickel-iron meteorite about 50

meters across striking the plain at a speed of several kilometers per second, at which vaporization became a dominant factor (Fig 1.1d). Studies on liquid drop impacts in general help understand those events.

1.2 Physics of liquid drop impacts

We start with an idealized model problem of the liquid drop impact on a pre-existing uniform layer of liquid. The drop is considered spherical with radius R and velocity U just before contacting the liquid layer. Both the drop and the layer are made of the same Newtonian fluid, and the impact speed is perpendicular to the layer surface (normal impact). I will first discuss the compressible effects and the validity of continuum fluid dynamics. Next, I will establish the governing equations for the model problem, from which I construct dimensionless groups based on dimensional analysis. Last, I will discuss several linear instabilities pertinent to the problem.

1.2.1 Compressible phase and continuum model

For a very short time after the impact, the geometry of the problem is independent of the liquid properties. An important length scale is the contact radius between the drop and the layer $r_c \simeq \sqrt{2URt}$ (see Appendix A). When the expansion of r_c is faster than the speed of sound c_0 in the liquid, the compressibility effects become important. Therefore we calculate the critical time before which compressibility effects are important from $\frac{dr_c}{dt} = c_0$. We obtain $t_c \simeq RU/2{c_0}^2$ (see *Bowden and Field* [1964]; *Rein* [1993]; *Yarin and Weiss* [1995]). For $R \sim 1$ mm, $U \sim 1$ m/s and $c_0 \sim 10^3$ m/s we obtain $r_c \sim 1$ μm and $t_c \sim 1$ ns, which already shows that compressibility effects are very short compared to the timescale of a typical impact ($R/U \sim 1$ ms). In addition, the volume compressed by the shock wave at time t_c after impact can be estimated by $\pi {r_c}^2 c_0 t_c \simeq \pi/2 R^3 (U/c_0)^3 = \frac{3}{8}(U/c_0)^3 V_{drop}$, with V_{drop} being the volume of the impacting drop. This shows that with $U/c_0 = O(10^{-3}) \ll 1$, compressibility affects a very

small volume fraction of the impacting drop, i.e. that its effects can be neglected. The estimates show that the impact Mach number $M = U/c_0$ is important for quantifying compressibility effects. For high-speed velocity impacts of Mach number of order one, this effect is significant (*Lesser* [1983]). The drops in our discussion here are normally generated by falling through air and therefore possess a much smaller Mach number. Therefore the liquid in our problem is treated as incompressible. At the early compressible stage estimated above with a small contact area of $r_c \sim 1$ μm, the number of molecules is about $\pi {r_c}^2/\pi a^2 \sim 10^8$ (a is a molecular size of the order of 10^{-10} m). Hence the continuum fluid dynamics is valid to fully describe the problem from the earliest stage (*Lesser* [1981]) and throughout the entire impact event.

1.2.2 Governing equations

As a two-phase flow, the drop impact problem is governed by two sets of equations that describe the motion of liquid and gas respectively. Henceforth, we use the subscript i to distinguish variables for the liquid ($i = 1$) from those of the gas (i=2).

Both liquid and gas follow the conservation of mass, which is described by the continuity equation with no source or sink:

$$\frac{D\rho_i}{Dt} + \rho\left(\nabla \cdot \mathbf{u}_i\right) = 0 \tag{1.1}$$

where ρ_i is the density, and $\mathbf{u}_i$ is the velocity field. According to the analysis on compressible phase, we can further simplify this relationship by treating the liquid (i=1) as incompressible ($\frac{D\rho_i}{Dt} = 0$) and therefore drop the first term:

$$\nabla \cdot \mathbf{u}_1 = 0 \tag{1.2}$$

The conservation of momentum is expressed by the Navier-Stokes equations:

$$\rho_i \left(\frac{\partial \mathbf{u}_i}{\partial t} + \mathbf{u}_i \cdot \nabla \mathbf{u}_i \right) = -\nabla p_i + \nabla \cdot \mathbf{T}_i + \mathbf{f}_i \tag{1.3}$$

where p_i is the pressure, $\mathbf{T}_i$ is the stress tensor, and $\mathbf{f}_i$ are the body forces acting on the fluid. For an incompressible Newtonian fluid $\nabla \cdot \mathbf{T}_i = \eta_i \nabla^2 \mathbf{u}_i$, where η_i is the dynamic viscosity of the fluid, which leads to

$$\rho_i \left(\frac{\partial \mathbf{u}_i}{\partial t} + \mathbf{u}_i \cdot \nabla \mathbf{u}_i \right) = -\nabla p_i + \eta_i \nabla^2 \mathbf{u}_i + \mathbf{f}_i \tag{1.4}$$

In the context of drop impact, the total body force $\mathbf{f}_i$ consists of gravity acting on vertical direction $\tilde{\mathbf{z}}$. Therefore, the Navier-Stokes equations take the form:

$$\rho_i \left(\frac{\partial \mathbf{u}_i}{\partial t} + \mathbf{u}_i \cdot \nabla \mathbf{u}_i \right) = -\nabla p_i + \eta_i \nabla^2 \mathbf{u}_i + \rho_i g \tilde{\mathbf{z}} \tag{1.5}$$

Let D be the diameter of the drop ($D = 2R$), we non-dimensionalize time with D/U, length with D, velocity with U, and pressure with $\rho_i U^2$:

$$\frac{\partial \tilde{\mathbf{u}}_i}{\partial \tilde{t}} + \tilde{\mathbf{u}}_i \cdot \tilde{\nabla} \tilde{\mathbf{u}}_i = -\tilde{\nabla} \tilde{p}_i + \frac{1}{Re_i} \tilde{\nabla}^2 \tilde{\mathbf{u}}_i + \frac{1}{Fr_i} \mathbf{z} \tag{1.6}$$

where $Re_i = \rho_i \, UD/\eta_i$, $Fr = U^2/gD$ and $\mathbf{z}$ is the unit vector in vertical direction. The former denotes the relative importance of the inertial and the viscous effect, while the latter measures the effects from gravity.

Equations 1.2 and 1.6 must be solved subject to boundary conditions. On the liquid-wall interface no liquid passes through the wall. If the wall is moving with velocity $\mathbf{U}$ and the velocity of a fluid particle right next to the wall is $\mathbf{u}_1$, then the normal components of these velocities must be the same:

$$\mathbf{u}_1 \cdot \mathbf{n} = \mathbf{U} \cdot \mathbf{n} \tag{1.7}$$

where $\mathbf{n}$ is the unit normal to the surface. One often chooses a frame of reference in

which the boundaries are at rest, or $\mathbf{U} = 0$; this boundary condition then becomes

$$\mathbf{u}_1 \cdot \mathbf{n} = 0 \tag{1.8}$$

Another condition is the "no-slip" condition that matches the tangential velocity of liquid to that of the surface,

$$\mathbf{u}_1 \times \mathbf{n} = \mathbf{U} \times \mathbf{n} \tag{1.9}$$

and, when $\mathbf{U} = 0$,

$$\mathbf{u}_1 \times \mathbf{n} = \mathbf{0} \tag{1.10}$$

Across the liquid-gas interface, the velocity vector is continuous, therefore

$$\mathbf{u}_1 = \mathbf{u}_2 \tag{1.11}$$

The general stress balance equation on the liquid-gas interface is

$$\mathbf{n} \cdot \mathbf{T}_1 - \mathbf{n} \cdot \mathbf{T}_2 = \gamma \mathbf{n} \left(\nabla \cdot \mathbf{n} \right) - \nabla \gamma \tag{1.12}$$

where γ is the interfacial surface tension, which can be treated as a constant in our problem. Therefore we drop the last item in Equation 1.12.

The tangential stress balance is obtained by taking (1.12) $\cdot \mathbf{t}$:

$$\eta_1 \frac{\partial}{\partial n} \mathbf{u}_1 \cdot \mathbf{t} = \eta_2 \frac{\partial}{\partial n} \mathbf{u}_2 \cdot \mathbf{t} \tag{1.13}$$

Similarly, the normal stress balance comes from (1.12) $\cdot \mathbf{n}$:

$$p_2 - p_1 + \eta_1 \frac{\partial}{\partial n} \mathbf{u}_1 \cdot \mathbf{n} - \eta_2 \frac{\partial}{\partial n} \mathbf{u}_2 \cdot \mathbf{n} = \frac{1}{\gamma} \kappa \tag{1.14}$$

where κ is the local curvature of the surface.

Non-dimensionalization of Equation 1.14 using $\rho_1 U^2$ yields:

$$\tilde{p_2} - \tilde{p_1} + \frac{1}{Re_1}\frac{\partial}{\partial n}\mathbf{u}_1 \cdot \mathbf{n} - \frac{\eta_2}{\eta_1}\frac{1}{Re_1}\frac{\partial}{\partial n}\mathbf{u}_2 \cdot \mathbf{n} = \frac{1}{We}\tilde{\kappa} \tag{1.15}$$

where the Weber number is defined as $We = \rho_1 D U^2/\gamma$. It compares the relative importance of surface tension and inertial effects.

Approximations are sometimes made by ignoring the gas completely, from the fact that the dynamics viscosity of a gas is small compared with that of a liquid. Equation 1.13 can thus be written as

$$\frac{\partial}{\partial n}\mathbf{u} \cdot \mathbf{t} = 0 \tag{1.16}$$

which is referred to as the vanishing shear stress at a free liquid surface. Equation 1.14 becomes

$$p_2 - p_1 + \eta_1 \frac{\partial}{\partial n}\mathbf{u}_1 \cdot \mathbf{n} = \frac{1}{\gamma}\kappa \tag{1.17}$$

1.2.3 Parametrization of the problem

Dimensional analysis plays an important role in describing physical systems. Generally speaking, a physical system can be completely described by N physical variables expressed in the combination of $M(< N)$ independent fundamental physical quantities such as the length, the time and the mass. According to the *Buckingham-pi theorem*, the system can equivalently be described by $N - M$ dimensionless variables constructed from original variables, which are the so-called dimensionless groups. The concept of dimensionless groups greatly simplifies the classification of system behaviors: two systems with same dimensionless groups have the same behavior to within a scale factor. There are two important notes on dimensionless groups: first, it is es-

sential to include all relevant physical variables or the resulting dimensionless groups are incomplete; second, there are multiple ways to construct dimensionless groups. However, the physically meaningful ones often lead to better understanding of the problem.

The construction of dimensionless groups is a convenient way to describe our model problem without solving the Navier-Stokes equation and boundary conditions. To create dimensionless groups, we start by listing all relevant physical variables. Liquid properties are described by the surface tension γ, the density ρ_1, and the dynamic viscosity η_1. The spherical liquid drop has diameter D and impact velocity U generated by gravitational acceleration g. The liquid layer is described by layer depth H. The existence of gas brings in two additional variables: the density ρ_2, and the dynamic viscosity η_2 (of the gas). Hence, the system is fully described by N =9 physical variables. All variables can be expressed in terms of three fundamental physical quantities: the time, the length and the mass (M=3). According to the Buckingham-pi theorem, the dimensionless group consists of six numbers ($N-M$=6) that fully describe the problem. We have already defined Re= $\rho_1 UD/\eta_1$, We= $\rho_1 DU^2/\gamma$ and $Fr = U^2/gD$. The gravity-related effects are described by the Froude number Fr. In our problem gravity effects are typically not important due to the short time span of the event: on the order of a millisecond. On the other hand, gravity acts on a timescale that is on the order of seconds. Therefore, gravity has very little contribution to the outcome of the impact. The dimensionless depth $h = H/D$ is defined to signify the amount of liquid in the layer that the impacting drop encounters. Additionally, two more dimensionless numbers represent the influence from gas: $\Lambda = \eta_2/\eta_1$, and $\Sigma = \rho_2/\rho_1$.

There are many ways to construct dimensionless groups, and some are more convenient than others in describing certain problems. The Ohnesorge number is defined as $Oh = We^{1/2}/Re$; it describes the relative importance of the viscous forces and the

surface tension. A higher Oh indicates more influence of viscous forces than surface tension. The Bond number $Bo = \rho_1 a R^2/\gamma$, where a is the acceleration associated with a body force (such as gravity). It is a measure of the importance of surface tension forces compared to body forces. A higher Bond number indicates that the system is relatively unaffected by the surface tension effects. Another important dimensionless number is defined as $K = We \cdot Oh^{-2/5}$, which is frequently used to describe the threshold of splashing (as we shall see later).

Two drop impacts with the same dimensionless numbers have the same outcome up to scaling factors, in both length and time. For example, it is natural to compare two different drop impact events at the same "half time" when half of the drop has submerged into the substrate (we have already implicitly scaled length by doing so). Likewise, it is usually convenient to scale time t with penetration time $\tau = D/U$ so that $\tilde{t} = t/\tau = tU/D$. The concept of a dimensionless time $\tilde{t}$ is convenient for describing various stages during an impact event without involving real units of time.

It is worth mentioning that, for a long time, the conventional view on the problem ignored the influence from the gas, based on the low density ρ_2 and dynamic viscosity η_2 of the gas relative to those of the liquid; typically $\Lambda = \eta_2/\eta_1 \approx 10^{-2}$) and $\Sigma = \rho_2/\rho_1 \approx 10^{-3}$. This is also referred to as the *conventional parametrization*, which reduces the total number of dimensionless groups from 6 to 4, dropping Λ and Σ. As we shall see in Chapter V and VI, the influence of the gas cannot be ignored in certain problems, and the conventional parametrization must be replaced by the complete parametrization with all 6 dimensionless groups.

1.2.4 Instabilities

Several linear instabilities in fluid dynamics are relevant to our study: the Rayleigh-Plateau instability, the Rayleigh-Taylor instability, the Richtmyer-Meshkov instability and the Kelvin-Helmholtz instability.

The Rayleigh-Plateau instability (*Rayleigh* [1878]) explains how a cylindrical liquid jet breaks into smaller liquid packets. It is triggered by the existence of tiny perturbations in the liquid jet, which can be decomposed into a series of sinusoidal modes. The Rayleigh-Plateau theory predicts the growth rate of each mode based exclusively on the wavelength of that mode and the radius of the liquid jet. The most amplified mode sets the dominant wavelength on the jet, which determines the size of the smaller liquid packets due to eventual break-up of the jet.

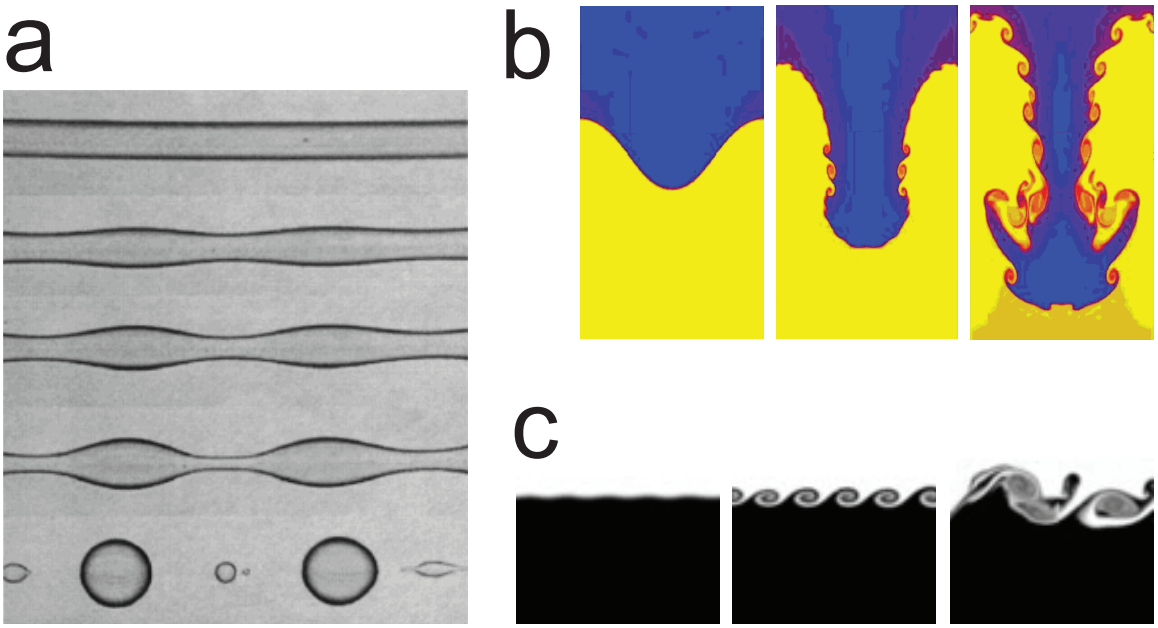

Figure 1.2: Illustration of several linear instabilities. a: Rayleigh-Plateau instability, b: Rayleigh-Taylor instability, c: Kelvin-Helmhotlz instability.

The Rayleigh-Taylor instability (*Rayleigh* [1883]) develops on the interface between two fluids of different densities, which occurs when the lighter fluid accelerates into the heavier fluid. Consider two completely plane-parallel layers of immiscible fluid, the heavier above the light one and both subject to gravity. The equilibrium is unstable to certain perturbations. An unstable disturbance will grow and lead to a release of potential energy, as the heavier material moves down under the effective gravitational field, and the lighter material is displaced upwards. The Richtmyer-Meshkov instability can be considered as the impulsive-acceleration limit of the Rayleigh-Taylor

instability (*Richtmyer* [1960]).

The Kelvin-Helmhotlz instability (*Kelvin* [1871]) can occur when there is velocity shear in a single continuous fluid, or when there is a velocity difference across the interface between two fluids. For sufficiently short enough wavelengths, if surface tension is ignored, two fluids in parallel motion with different velocities and densities yield an interface that is unstable for all speeds. With surface tension, the interface is stable until a threshold of velocity difference is reached. This instability is manifested as waves - for example, waves caused by wind on the surface of a pond.

1.3 Phenomenology of liquid drop impacts

1.3.1 Diversities and generalities

Many factors influence the outcome of a drop impact event: the drop may hit a dry or wet solid surface, or a deep pool of liquid; the size and shape of the drop; liquid properties such as density, viscosity, surface tension and viscoelasticity; the impact velocity and angle with respective to the surface, etc. Generally speaking, the results of a drop impact are extremely diverse, involved and surprising due to the vast parameter space.

There are, however, features common to almost all liquid drop impacts. First, as the liquid drop approaches a surface, air flows beneath the bottom of the drop and creates a pressure gradient under which the liquid-air interface deforms: the high pressure region near the axis retards the approach of the bottom of the drop, while the periphery of the drop experiences less pressure and travels faster. Therefore, a centrally located "dimple" in the drop is formed (*Francois and Mysels* [1962],*Platikanov* [1964],*Thoroddsen et al.* [2011]). Liquid is pushed outward from the contact region between the drop and the surface due to the inertia effects after impact. The literature refers to such phenomena as *jetting*, and the expanding liquid is defined as a *jet*.

The jet is subject to surface tension that restrains its expansion, and develops a corrugation which signifies the onset of a symmetry breaking instability. The amplitudes of the corrugations grow with time, sometimes leading to the emission of secondary droplets, a phenomenon defined as *splashing*.

The details of a liquid drop impact event depend on particular impact conditions. I will start by differentiating drop impacts on a dry substrate from those on a wet substrate. The former show relatively more complex behaviors due to the influence of the surface properties, i.e., wettability and roughness, which are not so important in the latter. Below I describe various features of both scenarios. My research focuses exclusively on impacts on a wet substrate.

1.3.2 Dry substrate impact

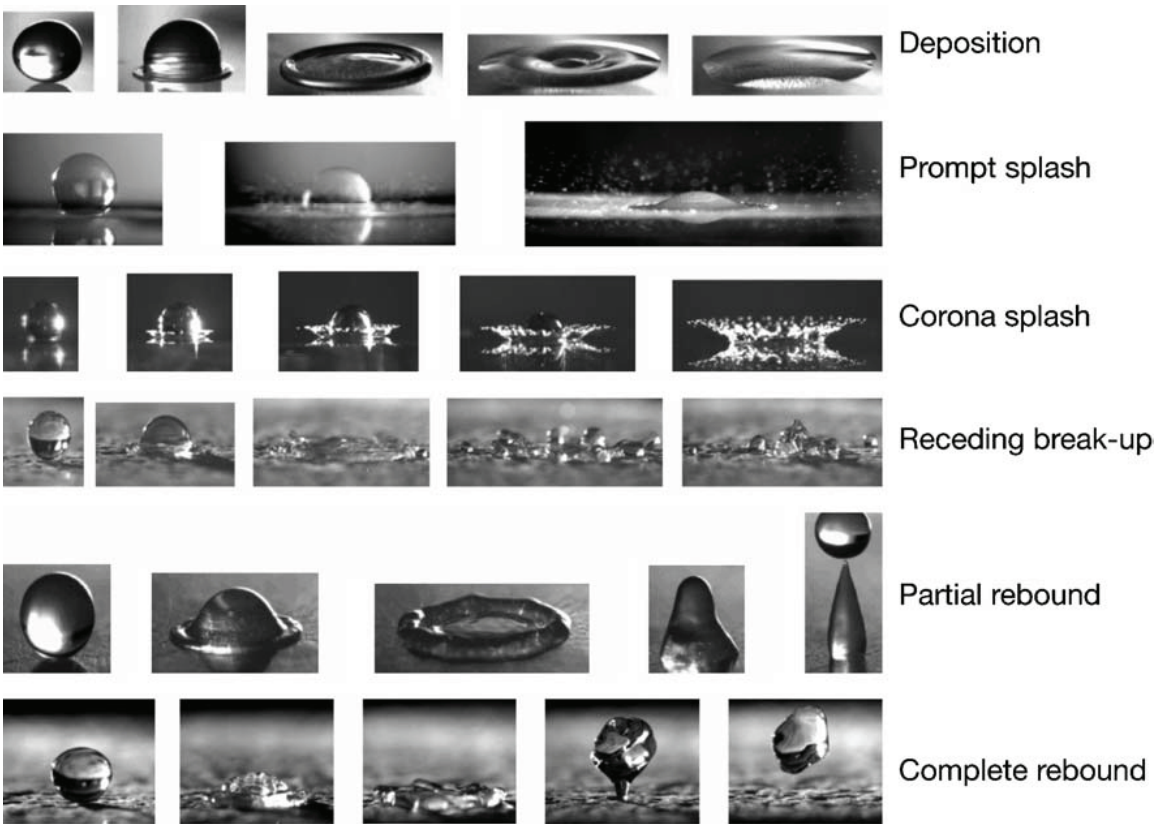

Figure 1.3: Morphology of drop impact on a dry surface. From *Rioboo et al.* [2001]. Courtesy of Begell House.

Rioboo et al. [2001] revealed six possible outcomes of a drop impact event on a dry wall: deposition, prompt splash, corona splash, receding break-up, partial rebound and complete rebound. The process of a dry surface impact can be roughly separated into two stages: deposition and recoil. When a drop impacts a solid surface, the drop first spreads until it reaches a maximum diameter, a process defined as *deposition*. The spreading part of the drop is defined as *lamella*. Once the lamella reaches maximum diameter, capillary forces become dominant and the drop starts retracting in the *recoil* phase. Different morphologies may develop during the deposition and recoil stages depending on the impact conditions.

1.3.2.1 Deposition

There are two stages in the deposition phase: the kinematic deposition and the actual deposition (*Rioboo et al.* [2002]). In the kinematic stage the radius of the drop base $R \approx t^{1/2}$ independent of physical properties of liquid and surface. Dependence on these parameters begins to be felt only in the actual deposition stage. At the end the drop spreads over the surface with final lamella diameter D_{max}, and the ratio between D_{max} and the drop diameter is the maximum spread factor $\xi = D_{max}/D$. *Scheller and Bousfield* [1995] proposed the empirical correlation

$$\xi = 0.61(Re^2Oh)^{0.166} = 0.61(We/Oh)^{0.166} \tag{1.18}$$

The first and part of the second stage of deposition constitutes an initial phase of the other scenarios of drop impact on a dry surface illustrated in Fig 1.3. Additional factors become important to the evolution at some point, introducing different morphological features.

1.3.2.2 Splashing

With a increased impact velocity on a rough surface, tiny droplets are detached at the periphery of the liquid lamella generated by the spreading drop. At the end the impacting drop spreads and stays at the wall. This is the so-called *prompt splash* (second from top in Fig 1.3). With reduced surface tension, the liquid lamella can detach from the wall, resulting in a *corona splash* (third from top in Fig 1.3). The corona/crown is similar to that observed on a wet substrate impact on extremely thin liquid layers by *Wang and Chen* [2000], where surface properties of the wall cannot be ignored. The corona splash can be completely suppressed by decreasing the pressure of the surrounding gas *Xu et al.* [2005], which suggests ambient gas is equally important in introducing perturbations to the system as roughness of the surface.

Mundo et al. [1995] characterized the transition from spreading to splashing in drop impacts on dry surfaces at atmospheric pressure using the parameter $K_d = We^{1/2}Re^{1/2} = K^{5/8}$. According to the author, K_d=57.7 or K=657.48, which does not include surface roughness. *Cossali et al.* [1997] proposed to correlate the available data on the splashing threshold at a dry surface at atmospheric pressure as

$$K_s = 649 + 3.76/{R_{nd}}^{0.63} \tag{1.19}$$

where R_{nd} is the nondimensional roughness defined by $R_{nd} = R_a/D = 5 \cdot 10^{-5}$, R_a being the amplitude of roughness and D the drop diameter.

Rioboo et al. [2001] claimed that the thresholds between the various scenarios cannot be quantified by We, Re, Oh and K, because they do not reflect surface wettability and roughness.

As the drop spreads, the axisymmetrical lamella is subject to azimuthal disturbances, whose growth results in *fingering* at the rim of a spreading drop on a dry

wall. *Aziz and Chandra* [2000] reported molten tin droplets falling onto a stainless steel surface at different temperatures. The droplet solidified as it spread across the surface at various rates depending on the surface temperature. They found that the spreading of the drop was directly correlated with increasing substrate temperature. The authors also found finger-like structures around the periphery of the drop akin to a liquid drop impact. With higher temperature, the fingers were allowed to develop more fully and grew greater in number. The authors successfully predicted the number of fingers based on the Rayleigh-Taylor instability. Roughness of the surface was also shown to affect the number of fingers (*Thoroddsen and Sakakibara* [1998], *Range and Feuillebois* [1998]).

Mundo et al. [1995] experimentally studied drop impacts on inclined solid surfaces. They found that the tangential impact velocity is nearly completely transferred to secondary droplets in the case of a splash; the normal momentum is only partially conserved, because the energy is dissipated during the impact and in the formation of the corona/crown. For rough surfaces the splashing occurs under the influence of the local surface angle, leading to a transfer of tangential momentum into normal momentum. They also found that the splash/deposition threshold is determined by the normal component of impact velocity.

1.3.2.3 Receding stage

The kinetic energy of the impacting drop is partly dissipated by viscous forces and partly converted to surface energy during deposition stage. The following behavior of the drop depends greatly on surface wettability, which is characterized by the advancing and the receding angles, θ_{adv} and θ_{rec}. These two angles can be measured by the sessile drop method at a certain velocity of the contact-line motion. Due to contact angle hysteresis (if any), $\theta_{rec} < \theta_{adv}$ (without it θ_{rec}=θ_{adv}). For a given static drop volume a maximum (based on θ_{rec}) and a minimum (based on θ_{adv}) diameter,

d_r and d_a respectively, can be defined (*Rioboo et al.* [2002]).

Rioboo et al. [2002], and *Schiaffino and Sonin* [1997] argued that if viscous effects dissipate most of the kinetic energy of the impacting drop, the slowly advancing lamella reaches diameter d_a. With more kinetic energy, the lamella may pass d_r, after which the lamella recedes. For low-viscosity liquids the contact line will start its receding motion after a delay of order $(\rho D^3/\gamma)^{1/2}$. When the receding motion of the shrinking lamella is sufficiently low, it may be arrested at d_r; otherwise, it passes d_r and stabilizes between d_r and d_a, stopping at some contact angle due to contact angle hysteresis. *Receding breakup* happens during this stage for non-wettable surfaces (d_a=0): the shrinking lamella breaks up into a number of fingers, probably due to capillary instability.

1.3.2.4 Rebound

In the receding stage, surface energy is converted to kinematic energy which dissipates via viscous forces. However, if there is still some kinetic energy left at the end of the receding stage, the lamella passes d_a and collapses into the impact center. The energy of such a collapse is high enough to squeeze liquid upward from the surface into a rising column of liquid reminiscent of a Worthington jet (Fig 1.7). Depending on the amount of energy left, the liquid column either stays partly at the surface and launches one or more droplets at its top due to capillary instability (*partial rebound*), or it detaches from the surface as one drop (*complete rebound*).

Rebound is enhanced by the Leidenfrost effect, a phenomenon in which a liquid, in near contact with a mass significantly hotter than the liquid's boiling point, produces an insulating vapor layer which keeps that liquid from boiling rapidly. In this case, the vapor layer propels the drop upward (*Chandra and Avedisian* [1991], *Frohn and Roth* [2000], *Rein* [2002]). Bouncing behavior is also facilitated by superhydrophobic surfaces, where the contact-line hysteresis and the associated viscous losses are absent.

In such cases normal drop impacts at low We=0.07 lead to rebound of an almost spherical drop with a restitution coefficient of about 0.9 (*Richard and Quere* [2000]).

1.3.2.5 Final remarks

For normal impacts on a dry solid surface, we understand the nature of different behaviors and have a significant amount of data already available in the literature. Effects of surface properties on drop evolution still need to be fully characterized. The consequences of oblique impacts on a dry surface are still poorly understood, though we have some evidence showing that the normal velocity component is important in determining drop behavior. The formation of fingers at the free rim of the liquid lamella needs further investigation. *Xu et al.* [2005] showed that the partial vacuum has great influence on the corona splash. It would be interesting to test its effects on fingering.

Modeling of drop impact on a dry surface is reliable in the deposition phase based on energy balance (*Chandra and Avedisian* [1991], *Mao et al.* [1997], *Pasandideh-Fard et al.* [1996]), although there is still no complete agreement on the boundary conditions to be implemented at the moving contact line (*Reznik and Yain* [2002a],*Reznik and Yain* [2002b], *Reznik and Yain* [2002c], *Sikalo et al.* [2005], *S. et al.* [1997], *Gentner et al.* [2004]). The transition from deposition to the receding phase is incompletely understood and poses a challenge to modeling. Analytical modeling of drop rebound was attempted by *Xu et al.* [1998], *Kim and Chun* [2001], *Okumura et al.* [2003].

1.3.3 Wet substrate impact

1.3.3.1 Deposition, spreading and splashing

Empirical observations of wet drop impact reveal complex behaviors loosely divided into several regimes based on We and Re as shown in Fig 1.4. On the most basic level, the behavior belongs to the "*splash*" regime if the impact generates secondary

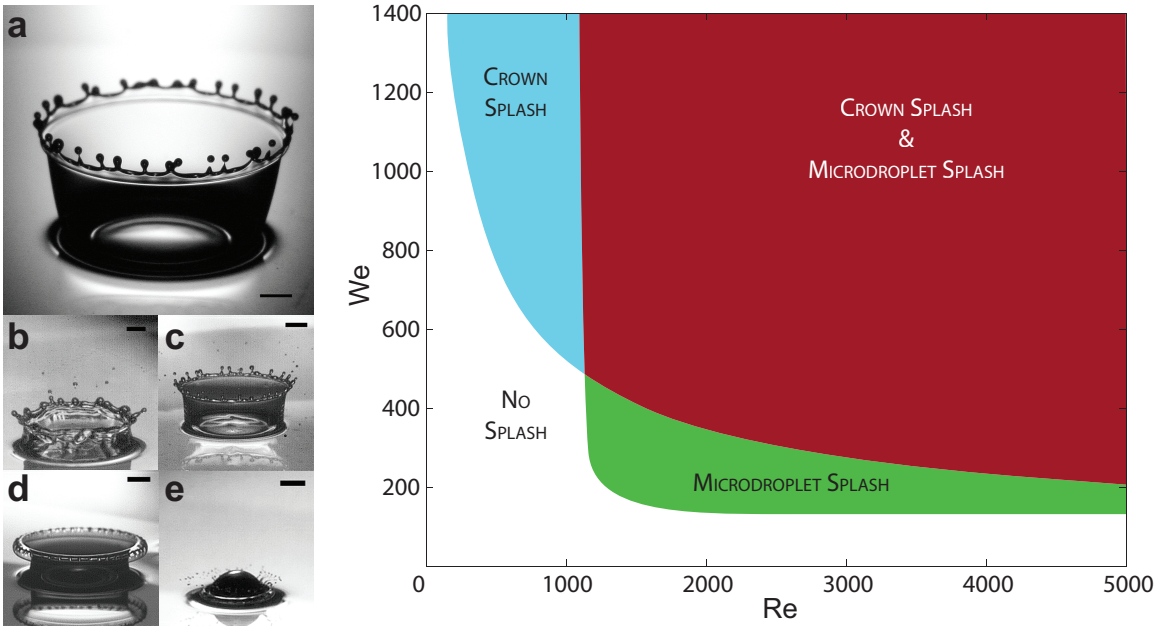

Figure 1.4: Left: Morphology of wet substrate impact, a: crown splash, b,c: crown splash & microdroplet splash, d: no splash, e: microdroplet splash, Right: Phase diagram indicating the qualitatively different regimes of drop impact with $h = 0.2$. Adapted from *Deegan et al.* [2008]

droplets; otherwise, it belongs to the "*no splash*" regime. The former is further divided into the *crown splash*, the *microdroplet splash* and the combination of two; the latter consists of the *deposition* and the *spreading*. Here I treat the splash regime as one entity and focus on the differences among deposition, spreading and splashing. Later I shall return to the various types in the splash regime.

At sufficiently low impact velocities, drops spread over the wall axisymmetrically, taking the shape of a crater. The wall of the crater is called a *lamella* or *crown* in the literature (Fig 1.5b), and the top of crater is stable with no visible corrugations. This process is called *spreading*.

At even lower impact velocities there is no lamella formation. Instead, the drop spreads over the surface of the liquid layer, a situation defined by *Rioboo et al.* [2003] as deposition (Fig 1.5a). *Rioboo et al.* [2003] used the dimensionless depth h and earlier defined $K = We \cdot Oh^{-2/5}$ to separate spreading and deposition. They found

that for $0.06 < h < 0.14$, deposition happens when K is less than 400, otherwise spreading takes place. They also found that deposition always happens for very thin liquid layers: in other words, the lamella does not form on ultra-thin liquid layers.

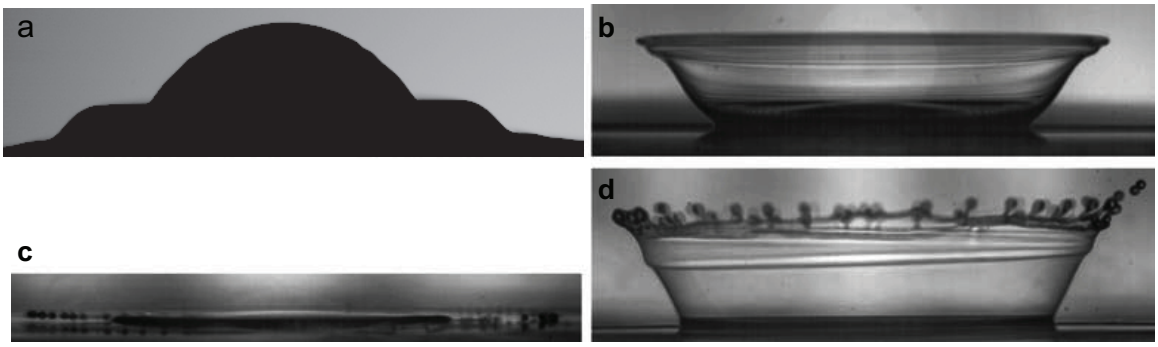

Figure 1.5: Outcomes of a drop impact on a wetted solid surface. a: deposition without formation of crown, b: formation of crown without break-up, c: splashing without crown, d: splashing with crown. Adapted from: *Rioboo et al.* [2003]

Splashing happens at higher impact velocities. The rim of the lamella becomes unstable and emits secondary droplets (Fig 1.5d). In particular, for ultra-thin layers the lamella almost coincides with the layer surface and results in horizontal emission of droplets (Fig 1.5c). *Cossali et al.* [1997] established an experimental condition for splashing using K, h and Oh defined earlier:

$$K > K_s = 2100 + 5880h^{1.44} \tag{1.20a}$$

$$0.1 < h < 1, Oh > 7 \cdot 10^{-3} \tag{1.20b}$$

Equation 1.20 was established for a specific value of the nondimensional roughness $R_{nd} = R_a/D = 5{\cdot}10^{-5}$, R_a being the amplitude of roughness and D the drop diameter. More experimental results can be found in *Stow and Hadfield* [1981], *Vander Wal et al.* [2006], *Zhao et al.* [2011].

From a theoretical viewpoint, *Yarin and Weiss* [1995] predicted the splashing

condition for a train of droplets with frequency f in terms of the velocity of drop U:

$$U >> (\frac{\gamma}{\rho})^{1/4}\nu^{1/8}f^{3/8} \tag{1.21}$$

with γ being surface tension, ρ density and ν kinematic viscosity. This result can be recast in terms of $K \approx 10000$, which is in reasonable agreement with Equation 1.20.

In summary, the previous studies have shown the nature of the transition between deposition, spreading and splashing along with abundant experimental data. There are, however, discrepancies among available data which can be attributed to factors such as the roughness of the surface, which needs to be investigated more thoroughly. The splashing behavior was predicted in various numerical simulations (*Rieber and Frohn* [1999], *Josserand and Zaleski* [2003], *Coppola et al.* [2011]) but needs verifications from experiments for accuracy of modeling. We know very little about oblique impacts (where a drop hits the surface with both horizontal and vertical velocity) on a wet substrate and have no data on transitions between deposition, spreading and splashing for oblique impacts.

In applications such as spray painting and cooling, the density of droplets is generally high. Conventional modeling approaches simply superimpose the results from single drop impacts. *Tropea and Roisman* [2000] showed that the splashing behavior at a given point near the solid surface can be influenced by the conditions far from that point. *Roisman et al.* [2002] experimentally investigated the interaction between two liquid drops separated both spatially and temporally. They found that the collision of two synchronized drops generates an uprising sheet along their intersection line. When there is a time lag between the impacts, the sheet is inclined from the vertical towards the earlier drop. The interaction of the drops produces several cylindrical jets formed almost at the substrate. These jets break up and create a number of secondary droplets. The conclusion is that the interaction of two drops can lead to jetting and splashes that are absent in the case of two separate single

drop impacts. The modeling of interactions between multiple drop impacts is still a relatively unexplored area.

1.3.3.2 Lamella

In both the splash and the no-splash regimes, the most common feature is rising liquid sheet called *lamella* as seen in Fig 1.6(a). It was first experimentally revealed by *Worthington* [1908]. One notable feature of the lamella is the existence of a visible outer rim. With relatively low velocity, the rim remains stable (spreading), while a higher impact velocity results in a more unstable rim from which numerous secondary droplets are ejected (splashing). One example is the crown splash in Fig 1.4a, where the rim dissociates into multiple secondary droplets resembling a real crown. Those secondary droplets are so-called *crown droplets*.

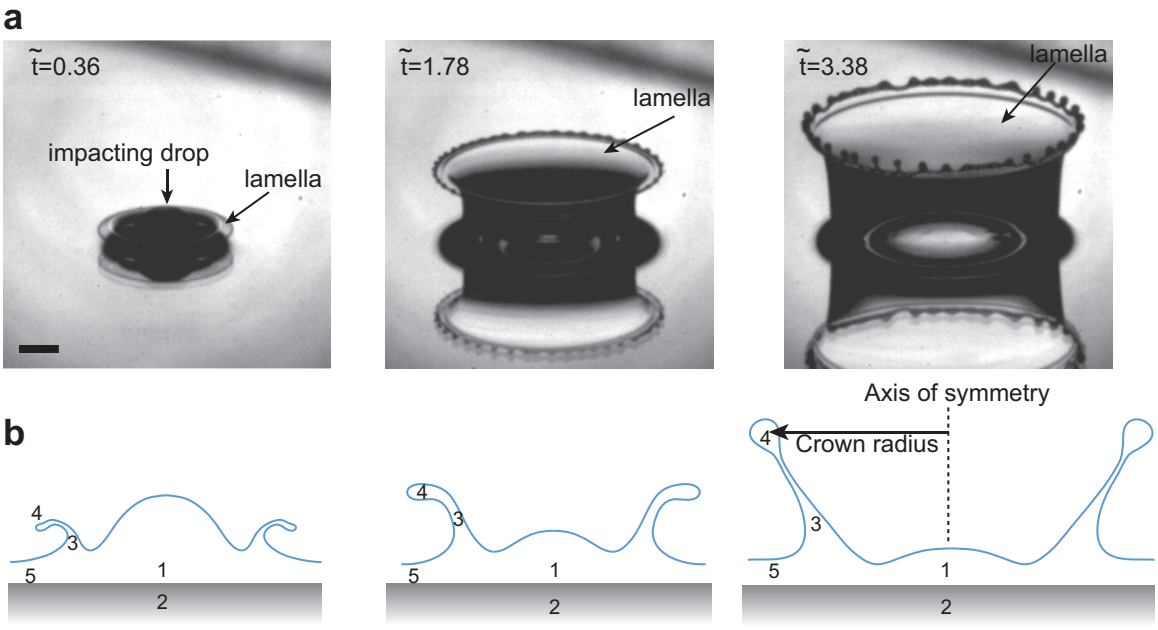

Figure 1.6: a: Time evolution of lamella viewed from an angle above substrate, scale bar: 1mm, b: A cartoon of cross section through impact center. 1, residual top of impacting drop; 2, wall; 3, section of lamella propagating outward; 4, cross-section of free rim; 5, liquid layer on wall.

Theoretically, *Peregrine* [1981] gave a simple one-dimensional mathematical model

of the lamella. Without using a spherical drop but a cylindrical jet, the model showed there is a discontinuous jump in the velocity of liquid where the lamella is propelled upward. A more accurate model provided by *Yarin and Weiss* [1995] considers the situation where, after the drop impact, a circular spot near the impact center has a distribution of the initial outward velocity of the order of the impact velocity. The liquid moving outward from this central spot impinges on the liquid from the undisturbed liquid in the layer. As a result, due to the presence of the free surface, a kinematic discontinuity in the velocity distribution emerges, which is reminiscent of a shock wave in an incompressible liquid. They showed that the emergence of the lamella is a result of this discontinuity in the velocity.

On the experimental side, *Yarin and Weiss* [1995] measured the radius of crown r_c (Fig 1.6) versus time and approximated data with a best-fit based on

$$\frac{r_c}{D} = C1(\tilde{t} - C2)^{1/2} \tag{1.22}$$

where $C1$ and $C2$ are determined by the fit. *Levin and Hobbs* [1971], *Cossali et al.* [1997] confirmed the square-root dependence of r_c on time for a single impact on thin layers. *Cossali et al.* [1999] obtained crown height and velocity, and they found that the vertical velocity of the crown scaled by impact velocity is independent of the drop *We*. *Cossali et al.* [2004] claimed that crown thickness grows with time, but found no correlation of crown thickness to layer thickness or impact velocity. *Roisman and Tropea* [2002] provided the shape of the lamella analytically and compared it to experimental results from *Cossali et al.* [1999]. *Coppola et al.* [2011] carried out a 2D simulation on evolution of lamella. Their results on the base position of lamella agreed with *Josserand and Zaleski* [2003], which stated that the distance from base position to impact center grows as the square root of time. Based on a 2D model, *Howison et al.* [2005] showed that at early times, the layer and drop contribute equally to the flux ejected into lamella, while the layer contribution is negligible at later times.

Wang and Chen [2000] reported that the lamella tends to be thinner and easily broken for impacts on very thin layers (h=0.05). They also found that impacts on thin layers produce lamella angled outward compared to thick layers (Fig 1.7). Conversely, when the liquid layer is very thick as reviewed in *Oguz and Prosperetti* [1993], *Rein* [1993], the liquid motion initiated by the drop is virtually unconstrained and capable of pushing apart a significant liquid mass in the layer. The crater is surrounded by a thick expanding lamella that is almost perpendicular to the undisturbed layer surface which is later pulled back by surface tension. The reversed motion causes the crater to collapse, which may produce a distinct jet called a *Worthington jet*. This is a significant difference from impacts on thin layers, which do not produce the Worthington jet (*Wang and Chen* [2000],*Rioboo et al.* [2003]).

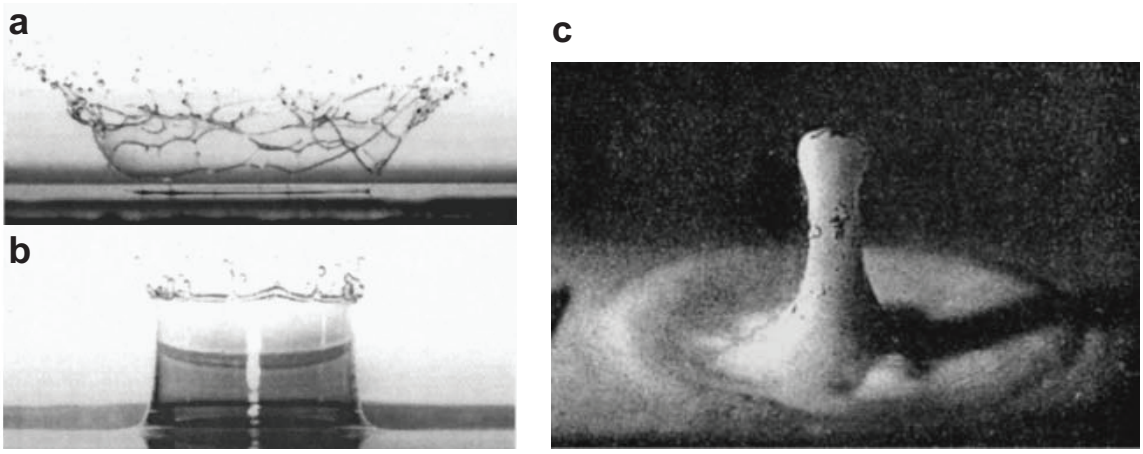

Figure 1.7: Left: comparison between thin layer (a, $h = 0.05$) and thick layer (b, $h = 0.5$) from *Wang and Chen* [2000]. Right: Worthington jet after impact on a deep liquid pool (c, $h \gg 1$), adapted from *Worthington* [1908]

Modeling of wet substrate impact by *Weiss and Yarin* [1999] showed a lamella is formed when $We \gtrapprox 40$. They ignored the viscosity of the liquid, and the potential flow problem was solved using the boundary element method with the corresponding boundary integral equation. *Davidson* [2002] published numerical results regarding the dynamics of the lamella and found it consistent with experimental data from

Cossali et al. [1997]. *Rieber and Frohn* [1999] took viscosity into account using a volume-of-fluid method and confirmed the crown radius-time relationship in Equation 1.22.

Previous work has shown an understanding of the formation of the lamella and numerical modeling of it. However, the experimental data regarding the lamella are incomplete. For example, there was no experimental data on the thickness of the lamella. Consequently we cannot verify certain aspects of the modeling. It has been shown that the angle between the lamella and the surface decreases as the layer becomes thinner, until it vanishes for extremely thin layers. More investigations are needed on impacts on extremely thin layers to understand the effects from surface roughness. Furthermore, the understanding on oblique impacts is limited: *Roisman and Tropea* [2002] simulated oblique impacts and found that when the ratio between the tangential velocity and the normal velocity is greater than some critical value, the shape of the crown base is no longer a closed curve; otherwise the base is a circle with a shifting center. A similar behavior of the crown after an oblique drop impact was observed by *Lavergne and Platet* [1999].

1.3.3.3 Ejecta sheet

The *ejecta sheet* is a liquid jet generated during the impact different from the lamella. First, it appears at a much earlier time than that of the lamella, which is a major reason that it was not discovered until recently from a boundary integral method simulation with a inviscid fluid by *Weiss and Yarin* [1999]. In the simulation, at $t \approx 10^{-6}$ to 10^{-5}s (which is three orders of magnitude less than the time of crown formation), a jetting sets in the middle of the neck between the oncoming drop and the liquid layer (Fig 1.8a). The numerical simulations of *Davidson* [2002] with an improved re-gridding procedure confirmed the same jetting phenomenon but also with a inviscid fluid. *Josserand and Zaleski* [2003] introduced viscosity to the simulation

and found the same jet. *Thoroddsen* [2002] first verified the existence of the jet experimentally (Fig 1.8b) and referred to it as the *ejecta sheet*. The jetting is caused by the rapidly moving liquid in the upper part of the neck from the drop impinging on slowly moving liquid below. The velocity jump is so great that the inertial forces dominate the surface tension and squeeze the liquid radially from the neck. The physical origin of the jetting is the same as that of crown formation: the onset of a kinematic discontinuity, irrespective of the specific shape of the free surface (*Yarin* [2006]).

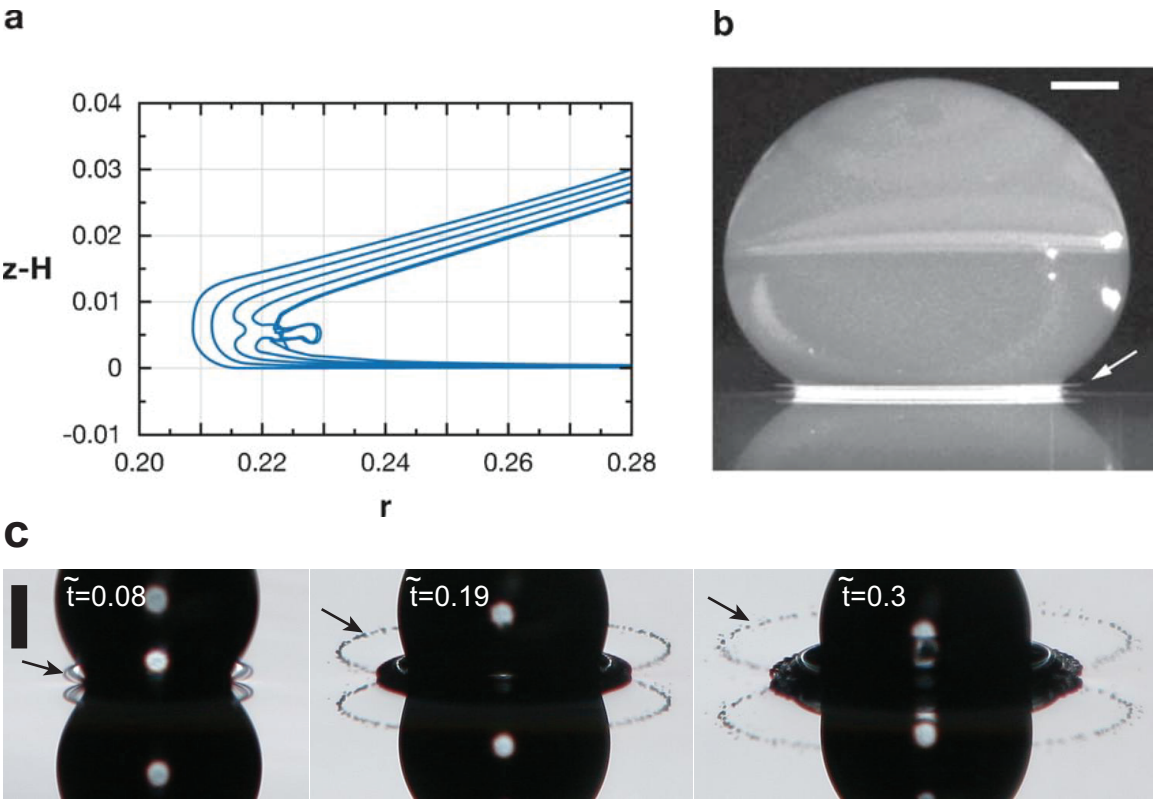

Figure 1.8: a: Ejecta sheet predicted by *Weiss and Yarin* [1999] at We=2000 and $h = 0.125$. The different curves correspond to various times after impact. b: Ejecta sheet observed by *Thoroddsen* [2002] at We=4170, Re=1080 long before lamella formation. Scale bar: 1 mm c: Ejecta sheet breaking into microdroplets. Scale bar: 0.5 mm.

Another major difference between the ejecta sheet and the lamella is that the former moves at a much higher speed. The dynamics of the ejecta sheet was exper-

imentally studied by *Thoroddsen* [2002]. An ejecta sheet resulting from pure water drop impact breaks up too quickly for detection, so they measured the initial speeds of droplets which were found to be ten times the impact velocity. The velocities of droplets from an ejecta sheet is significantly higher than have been observed in previous studies of secondary droplets (*Levin and Hobbs* [1971], *Mundo et al.* [1995], *Cossali et al.* [1997]). By mixing glycerin into water and increasing fluid viscosity, an ejecta sheet may stay intact for a longer period of time. The velocity of an intact sheet is found to decrease as viscosity η to the -1/2 power. They also found that an ejecta sheet emerges earlier for lower viscosities, converging to a fixed value for the smallest viscosities. Moreover, partial vacuum was found to change the morphology of an ejecta sheet significantly (*Thoroddsen et al.* [2011]) at intermediate time scale ($\tilde{t} \sim 1$), a fact that is consistent with its submicron thickness (300 nm).

Theoretically, *Josserand and Zaleski* [2003] argued that ejecta sheets form when the inertia effects overcome the surface tension that pulls it back. They claimed that the ejecta sheet forms when:

$$We^{1/2} Re^{1/2} \geqslant K_c \tag{1.23}$$

where K_c is a constant whose value depends on a precise description of the flow inside the jet. This expression can be recast in the same form as Equation 1.20, which describes the splashing threshold for the lamella. In fact, in a numerical simulation by the same author, the ejecta sheet evolves into a lamella. There are few theoretical results on instability associated with ejecta sheets. *Krechetnikov and Homsy* [2009] argued the ejecta sheet is subject to the Richtmyer-Meshkov instability when impulsively accelerated and Rayleigh-Taylor instability when decelerated. In addition, they claimed the wavelength of corrugation is set by the Richtmyer-Meshkov instability. This claim is yet to be confirmed, partly due to experimental difficulties resulting from the tiny length and time scale of ejecta sheets.

Usually the ejecta sheet disappears via various mechanisms reported in the literature. In one scenario, an ejecta sheet breaks up quickly after formation and produces secondary droplets, which *Deegan et al.* [2008] referred to as *microdroplets* (Fig 1.8c) because they are significantly smaller than those from lamella (crown splash). In a different scenario from a 2D boundary integral method calculation, *Davidson* [2002] found no breaking of the ejecta sheet but multiple reconnections between the ejecta sheet and the impacting drop. Additionally, *Josserand and Zaleski* [2003] found the ejecta sheet grew into a lamella in their volume-of-fluid method. Given the vast parameter space of the problem, there may be other behaviors of the ejecta sheet that deserve more investigation. *Thoroddsen et al.* [2011] showed partial vacuum changes the dynamics of the ejecta sheet at long times after the impact, yet it remains to be seen whether early time behavior of the ejecta sheet is related to the gaseous environment. There is very little understanding about the instability on the ejecta sheet.

1.3.3.4 Break-up of the free rim

The free rim of a liquid sheet with uniform thickness is pulled back by the Taylor-Culick mechanism (*Savva and Bush* [2009]) at the speed $V_{rim} = [2\gamma/\rho\delta]^{1/2}$, δ being the thickness of the sheet. As the lamella rises and expands outward, its top portion (rim) retracts relative to the bulk in a similar fashion. Splashing results from the breaking of symmetry on the rim due to this instability (Fig 1.9). There are, however, very different explanations for the instability on the rim and related secondary droplets.

Some authors believe corrugation on the rim originates from capillary instability, which is considered as a toroid either fully detached from the lamella or attached to it. In the former case where the free rim is considered an isolated cylinder, *Rieber and Frohn* [1999] performed a simulation to obtain the number of cusps formed on the rim of the lamella, which turned out to be fairly close to the number predicted by

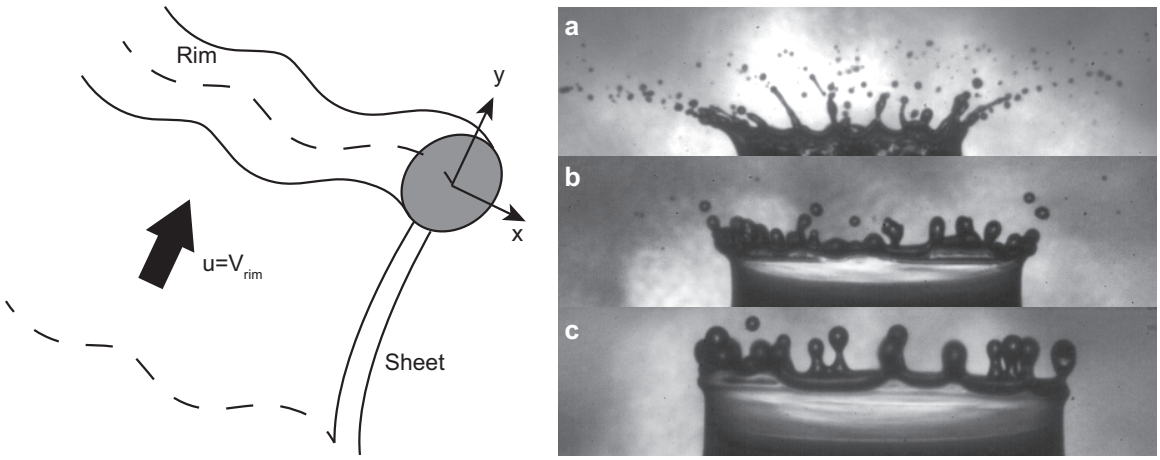

Figure 1.9: Left: Sketch of the rim bounding a sheet; Right: various scenarios of secondary droplets generated from rim of lamella

Rayleigh's theory (*Rayleigh* [1878]) for a liquid cylinder. However, their conclusion is purely computationally based without experimental confirmation. When considering a rim joined by a lamella, *Fullana and Zaleski* [1999] analyzed the stability of a thin sheet of fluid of uniform thickness ending with a retracting rim (Fig 1.9) based on Rayleigh's analysis of the effect of capillary forces on a round jet (*Rayleigh* [1878]). They showed that perturbations may be amplified only for very large wavelengths and large times. *Roisman and Tropea* [2005] claimed that the velocity gradient $\partial u/\partial y$ in the lamella (Fig 1.9) is critical to stability in the rim: when $\partial u/\partial y > 0$ the rim centerline is unstable; otherwise it is stable and no corrugation takes place. Moreover, their calculations showed the velocity gradient is always positive, so the rim centerline is unstable at all times. *Bremond and Villermaux* [2006] compared the gain from both the Rayleigh-Plateau instability (*Rayleigh* [1878]) and the Rayleigh-Taylor instability (*Taylor* [1950]) on the rim of a radially expanding sheet and found that the former always overcomes the latter. *Roisman et al.* [2007] applied a linear stability analysis to a straight rim and claimed that the main origin of the transverse instability is the inertia of the liquid entering the rim while capillary forces lead to stabilization of this type of instability.

Statistical studies on secondary droplets such as the distribution of size and velocity were widely used in *Stow and Stainer* [1977], *Mundo et al.* [1995], *Cossali et al.* [2004]. *Yarin and Weiss* [1995] argued that capillary instability cannot be the cause for secondary droplets generation based on the discrepancy in number of droplets between the experiments of *Stow and Stainer* [1977] and the theoretical predictions based on a corrugate cylinder. Instead, they proposed a nonlinear mechanism to describe the rim shape $y = Y(x,t)$ based on the following equation:

$$\frac{\partial Y}{\partial t} = V_{rim}\left[1 + (\frac{\partial Y}{\partial x})^2\right]^{1/2} \tag{1.24}$$

y being the coordinate directed along the lamella toward the solid wall and x the circumferential coordinate over the lamella (Fig 1.9). The solution leads to the formation of cusps that pinch off into secondary droplets. The perturbations could be triggered by wall roughness the moment the lamella was propelled upward. *Gueyffier and Zaleski* [1998] argued that drop impact produces a sudden and large acceleration of the interface which may become unstable due to the Richtmyer-Meshkov instability (*Richtmyer* [1960]).

So far most studies on the instability of the rim is related to the lamella. It is understood that the lamella is closely related to the instability of the rim as the former is constantly pumping mass into the latter. The velocity of the rim relative to the lamella is approximated by the Taylor-Culick relationship for a uniform liquid sheet. In the context of drop impact this velocity depends on many factors (geometry of lamella, velocity gradient on lamella, etc.) and therefore needs more investigation. So far, multiple mechanisms claim responsibility for the instability on the lamella rim, yet few can provide sufficient evidence to support the claim. A convincing explanation should provide consistent results from theory, simulation and experiments at various times after impact, not only at the time when droplets are generated (such as comparison of number of droplets). During a single impact event, various

mechanisms may exist and compete with each other. Given the vast parameter space of wet drop impact, different mechanisms may apply to different regimes.

1.4 Approaches to the problem

1.4.1 Analytical solutions

It is generally difficult to obtain analytical solutions that faithfully describe the flow inside the liquid after the impact. The difficulties include: first, a singularity of the curvature (with strong effects of surface tension) appears at the connection of the drop and surface upon impact, which makes the initial conditions hard to determine; second, there exist multiple stages of the evolution with various characteristic length and time scales; third, the mathematically convenient approach of a potential flow requires an inviscid liquid. In practice, the initial conditions are usually set arbitrarily; events that are associated with different stages of the problem are studied separately and described by asymptotic solutions; and the viscosity is usually ignored for a potential flow description of the problem. Because of a series of simplifications applied to the problem, analytical solutions cannot be directly compared to experimental/numerical results, but rather serve as insights into the physics behind the problem.

Peregrine [1981] considered a case where a horizontally shifting liquid jet (with a constant volume flux) impinges on a pre-existing liquid layer. This setup is similar to our model problem in the sense that the impacting drop pushes away liquid in the layer and creates a rising sheet. The author ignored the viscosity of the liquid and described the flow with streamlines, whose velocities were dictated by Bernoulli's theorem. Using the conservation of mass and momentum, the author gave analytical solutions for the speed and the angle of the rising sheet. The model also ignored surface tension. An important conclusion from this study is that the velocity has a

discontinuity where the liquid is propelled from the surface.

Yarin and Weiss [1995] studied a more realistic model of a spherical liquid drop hitting a thin liquid film. The liquid was considered incompressible and the viscosity was ignored. Adopting a simplified quasi-one-dimensional approach that averaged the flow velocity over the layer thickness, these authors were able to reveal the discontinuity in the velocity field that propagates and propels a part of the original liquid layer upward. Due to the axisymmetry of the problem, the rising liquid forms the shape of a crown, which is consistent with usual conception of a splash. The author gave an expression of a critical impact velocity beyond which the discontinuity (therefore the crown) forms. The viscosity was incorporated in a study by *Trujillo and Lee* [2001] but shown to have limited effects in the case of high impact velocities (Re=2000). This indicates that in high speed impacts, the dominant factor is the inertia of the liquid.

A conformal map is a function that preserves angles. Conformal mappings are powerful tools for solving problems that can be expressed in terms of a function of a complex variable but inconvenient geometries. By choosing an appropriate mapping, an inconvenient geometry can be transformed into a much more convenient one. *Howison et al.* [2005] applied this technique to the neck region between an infinitely long cylindrical drop (2D drop) and the liquid layer. The author showed that at short times after impact, the layer and drop contribute equally to the rising liquid sheet, while the layer contribution to the sheet is negligible at later times. For a typical drop impact event, the author claimed that viscosity effects can be safely ignored after about 1 μs and surface tension 1 ns, a very short time compared to the duration of the entire impact event. There is very little understanding on the time scale where the surface tension and viscosity cannot be ignored.

1.4.2 Numerical simulations

1.4.2.1 Boundary integral method

Due to the asymptotic nature of analytical methods, the real time solutions to the Navier-Stokes equations and many boundary conditions are often acquired via a numerical approach. For an idealized drop impact where the effect of viscosity is ignored (but still with surface tension), the boundary integral method (BIM) is a numerical scheme of high resolution of the deforming drop surface (see *Davidson* [2000]). Since viscous effects are ignored, the fluid motion will be irrotational throughout the drop and the liquid layer. The corresponding velocity potential ϕ satisfies:

$$\nabla^2\phi = 0 \tag{1.25}$$

A circular coordinate system is often used, where z represents the axis of symmetry and r the radial distance. At each time step, $\partial\phi/\partial n$ on the interface is determined by solving Equation 1.25 using a boundary integral approach based on a Green's function G which satisfies

$$\frac{\partial\phi}{\partial z} = 0 \;\; on \;\; z = 0 \tag{1.26}$$

and

$$\frac{\partial\phi}{\partial r} = 0 \;\; on \;\; r = R_f \tag{1.27}$$

where velocity $\mathbf{u} = \nabla\phi$, and R_f is chosen to be sufficiently large for the liquid film to be undisturbed at $r = R_f$ during the time period under consideration. The consequent values of $\partial\phi/\partial n$ are used in a simple Euler time-stepping of the velocity potential and surface shape.

Oguz and Prosperetti [1990] applied the boundary integral method to study the

bubble trapped underneath the drop after it hits the liquid surface. One interesting finding suggests that bubbles entrained by rain have a narrow spread in radii and therefore generate a single peaked noise spectrum under water. *Weiss and Yarin* [1999] used the same technique to study the jet formation following a strong impact and predicted a disk-like jet forms at the neck between the drop and the pre-existing liquid film, if the impact Weber number is high enough. *Davidson* [2002] found the predicted jet has multiple reconnections to the liquid layer after its formations; furthermore, the author verified a $t^{1/2}$ dependence for the radial position of the crown.

1.4.2.2 Volume of fluid method

The volume of fluid method (VOF) is another numerical technique for tracking and locating the free surface. It is characterized by a mesh that is either stationary or moving in a certain prescribed manner to accommodate the evolving shape of the interface. However, VOF is not a stand-alone flow-solving algorithm. The Navier-Stokes equations have to be solved separately to understand the motion of flow. The method is based on the idea of the so-called fraction function C. It is defined as the integral of a fluid's characteristic function in the control volume (a computational grid cell). Basically, when the cell is empty, with no traced fluid inside, the value of C is zero; when the cell is full, C=1; and when the interphasal interface cuts the cell, then $0 < C < 1$. The fraction function C is a scalar function, and while the fluid moves with velocity $\mathbf{v}$ every fluid particle retains its identity. Therefore, the substantial derivative of C needs to be zero:

$$\frac{\partial C}{\partial t} + \mathbf{v} \cdot \nabla C = 0 \tag{1.28}$$

The equation cannot be easily solved directly, since C is discontinuous. The most popular approach to the equation is the so-called geometrical reconstruction from *Hirt and Nichols* [1981].

Unlike the boundary integral method, the VOF method can incorporate viscous forces. *Josserand and Zaleski* [2003] performed simulations based on VOF and found that the radial position of the base where liquid is propelled upward is proportional to $t^{1/2}$, up to intermediate times after the impact ($\tilde{t} \approx 3$). Using an *ad hoc* modified version of the public-domain SURFER code (VOF in nature), *Coppola et al.* [2011] found that the first emergence of the jet after the impact depends on the fluid viscosity, while its subsequent evolution is *Re* independent. In addition, the authors obtained the velocity and pressure fields of the liquid, and captured the bubble entrapment of the gas in the liquid layer.

1.4.2.3 Lattice Boltzmann method

The Lattice Boltzmann method is a discrete computational method based upon the Boltzmann equation. The general equation can be written as:

$$\frac{\partial f}{\partial t} = \left(\frac{\partial f}{\partial t}\right)_{force} + \left(\frac{\partial f}{\partial t}\right)_{diff} + \left(\frac{\partial f}{\partial t}\right)_{coll} \tag{1.29}$$

where f stands for the probability of finding a particle at a specific location and time, the "force" term corresponds to the forces exerted on the particles by an external influence (not by themselves), the "diff" term represents the diffusion of particles, and "coll" is the collision term—accounting for the forces acting between particles in collisions. The method considers a typical volume element of fluid to be composed of a collection of particles that are represented by a particle velocity distribution function for each fluid component at each grid point. The time is counted in discrete time steps and the fluid particles can collide with each other as they move, possibly under applied forces. This method naturally accommodates a variety of boundary conditions such as the pressure drop across the interface between two fluids and wetting effects at a fluid-solid interface. It is an approach that bridges microscopic phenomena with the continuum macroscopic equations. This technique is relatively new to drop impact

simulations, and there have not been any published results yet.

1.4.3 Experimental methods

Flash photography (*Worthington and Cole* [1897], *Edgerton and Killian* [1954]) is frequently applied to observe drop impact events. The basic idea is to use a strong pulse of light combined with a very short exposure time. A series of pulses can be triggered consecutively to show a time sequence (see Fig 1.10). We used digital still cameras (Canon 20D and Nikon D80) to achieve an image resolution of 3000 by 2000 pixels in our experiments.

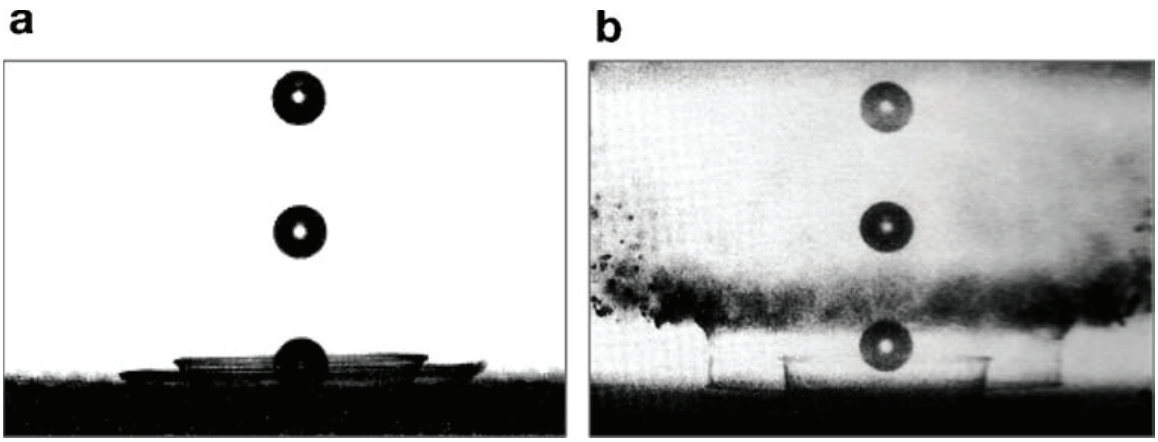

Figure 1.10: a: Spreading ethanol drops stroboscopically illuminated for a single drop. b: Splashing ethanol drops illuminated by a single flash for a train of impacting drops. From *Yarin and Weiss* [1995]

High-speed cameras are also widely used in drop impact experiments. Today they are entirely electronic, using either a charge-coupled device (CCD) or a CMOS active pixel sensor, recording typically over 1,000 frames per second into DRAM and playing images back slowly to study the motion of the transient phenomena. During the recording, most high-speed cameras write images to a temporary memory card, from which the data can be later downloaded onto a hard drive. The downloading is significantly slower than the recording. One challenge to high-speed video technique is the requirement of a strong and continuous light source due to its extremely short

exposure time (on the order of one microsecond). There is also a trade-off between speed of recording and image resolution: to achieve higher frames-per-second (FPS), one has to reduce the image resolution. The high speed camera used in our studies (Phantom v711, Vision Research) is capable of a resolution of 256 by 128 pixels at 100,000 FPS.

A dye-based optical visualization was applied by *Thoroddsen* [2002], who mixed fluorescent dye with the impacting drop (glycerol and water mixture) and the underlying layer to study the liquid boundary between them. However, this technique is limited by the type of fluid used in the experiment since some liquids cannot mix well with fluorescent dye. Furthermore, it is impossible to trace a particular parcel of fluid with this method and measure the speed of flow. One variation, particle image velocimetry (PIV), is capable of such tasks. It is used to obtain instantaneous velocity measurements and related properties in fluids. The fluid is seeded with tracer particles which, for sufficiently small particles, faithfully follow the flow dynamics. The degree to which the particles faithfully follow the flow is represented by the Stokes number, the ratio of the particle response time to the characteristic fluid time scale. For acceptable tracing accuracy, the particle response time should be faster than the smallest time scale of the flow. Moreover, tracer particles should not alter the flow or the fluid properties or interact with each other. We applied PIV to measure the velocity in the lamella. We, however, could not observe particles at certain parts of the lamella due to light issues caused by the refraction of light. As a solution, an X-ray based imaging technique was employed and is briefly introduced below. A more detailed introduction will be made in Chapter II.

Optically based observation methods are usually subject to some artifacts and cause certain hard-to-interpret parts in the recorded image (Fig 1.11:left). An alternative to optical imaging is X-ray phase contrast imaging (Fig 1.11:right) which mainly enhances the sharp boundaries and the interfaces between materials with dif-

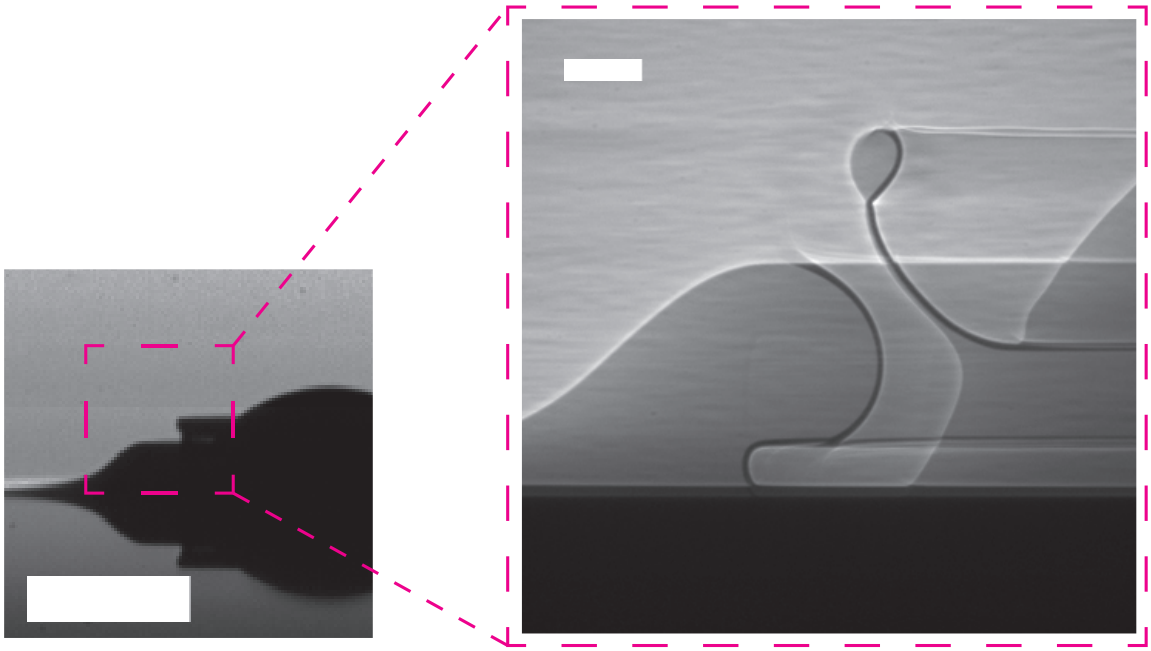

Figure 1.11: Images from optical (left) and X-ray (right) technique on same impact.

ferent refraction indices or abrupt thickness variations (*Wilkins et al.* [1996]). The phase contrast technique is naturally immune to the strong reflection or scattering effects that are usually associated with the optical imaging. The image contrast is most significant at the air-fluid interface, which leads to straightforward image interpretation.

1.5 Outline of the thesis

In this thesis, I will report experimental studies on several topics of the drop impact on a wet layer. Most studies were joint work with my advisor Robert Deegan. The motivation of Chapter II comes from the limitations of the conventional observation methods. Previous research has not been able to experimentally obtain certain features of lamella because of the optical artifacts. We applied an X-ray phase contrast imaging technique to the crown splash that revealed a complete liquid-air interface, from which we obtained reliable data of the lamella. By systematically changing the impact velocity U and the dimensionless depth h, I measured various

quantities related to the lamella for multiple impact conditions and obtained results for the first time. I compiled a database based on our measurements that can be used to check numerical simulations in the future.

In Chapter III, I focus on the instability developed on the rim of the lamella from a crown splash, which is the simplest type of splash and therefore providing the best hope for understanding its mechanism. By performing many experiments for the same parameter values, we measured the spectrum of small-amplitude perturbations growing on the lamella rim, which turns out to be in a great agreement with the prediction from Rayleigh-Plateau instability theory. We also dismissed other mechanisms proposed in the literature, at least for our experimental range.

In Chapter IV, I present the results of the ejecta sheet generated by liquid drop impacts onto a deep pool (therefore the dimensionless depth h does not enter the problem). By changing the type of liquid in the drop and the impact velocity, our study scanned the parameter space of Re and We and observed various outcomes of the impact. We clarified the relationship between the ejecta sheet and the lamella, characterized the behavior of ejecta sheet for various impact conditions, and determined the different fates of the ejecta sheet. We studied the dynamics of the ejecta sheet that include the emergence time, the emergence position, the velocity and their dependence on the viscosity of the liquid.

Partial vacuum has been shown to alter the dynamics of ejecta sheet at long times after the impact; however, there may be other effects at a different timescale and parameter range. In the studies reported in Chapter V, for a wide experimental range I controlled the level of ambient air pressure and tested its influence on the liquid drop impacts. I found the ambient gas pressure has influence on various regimes of the problem. In particular, ambient gas pressure has significant effects on the shape of the ejecta sheet, and is also related to the noise level in the system. No observable difference was found for the emergence of the ejecta sheet.

Chapter VI focuses on a particular feature of ejecta sheet: the onset of instability, with better image resolution provided by X-ray phase contrast imaging technique. We aimed to test whether the threshold of instability is influenced by the density and the dynamic viscosity of gas by changing the gaseous environment of the system. Our results showed that the density ratio of gas and liquid is not so important in determining the threshold of instability, while the dynamics viscosity ratio plays a more important role. This result provided evidence of the deficiency of conventional parametrization that ignores the properties of surrounding gas. We gave an explanation on the correlation between the dynamic viscosity and the threshold of instability on the ejecta sheet.

The studies in Chapter III, IV and VI were published in *Zhang et al.* [2010], *Zhang et al.* [2012a] and *Zhang et al.* [2012b].

CHAPTER II

X-ray studies on liquid drop impacts

2.1 Introduction

Most experimental studies on drop impacts rely on the information carried by the visible light, such as flash photography. Due to geometry of the problem, the refraction of light on the liquid-air interface usually renders some region unexposed (Fig 2.1 left). One solution is the X-ray phase contrast imaging (Fig 2.1 right) that allows us to observe the internal structure during the evolution.

Generally speaking, the contrast in the X-ray images comes from two independent effects: the absorption contrast and the phase contrast. X-rays which pass through an object along different paths are differentially absorbed, and the intensity pattern of the emerging beam records the distribution of absorbing materials, in our problem, the liquid lamella and the remnant of drop. This is the mechanism behind the absorption contrast, which is weak when the material is not highly absorptive or there is very little material in the path of X-ray.

An alternative approach proposed by *Wilkins et al.* [1996] records variations of the phase of the emerging radiation. They have shown that an X-ray beam, monochromatic or polychromatic, with high spatial coherence generates intensity contrast from the distortion of the wavefront, which is especially significant at sharp boundaries and interfaces between materials with different indices of refraction or abrupt thickness

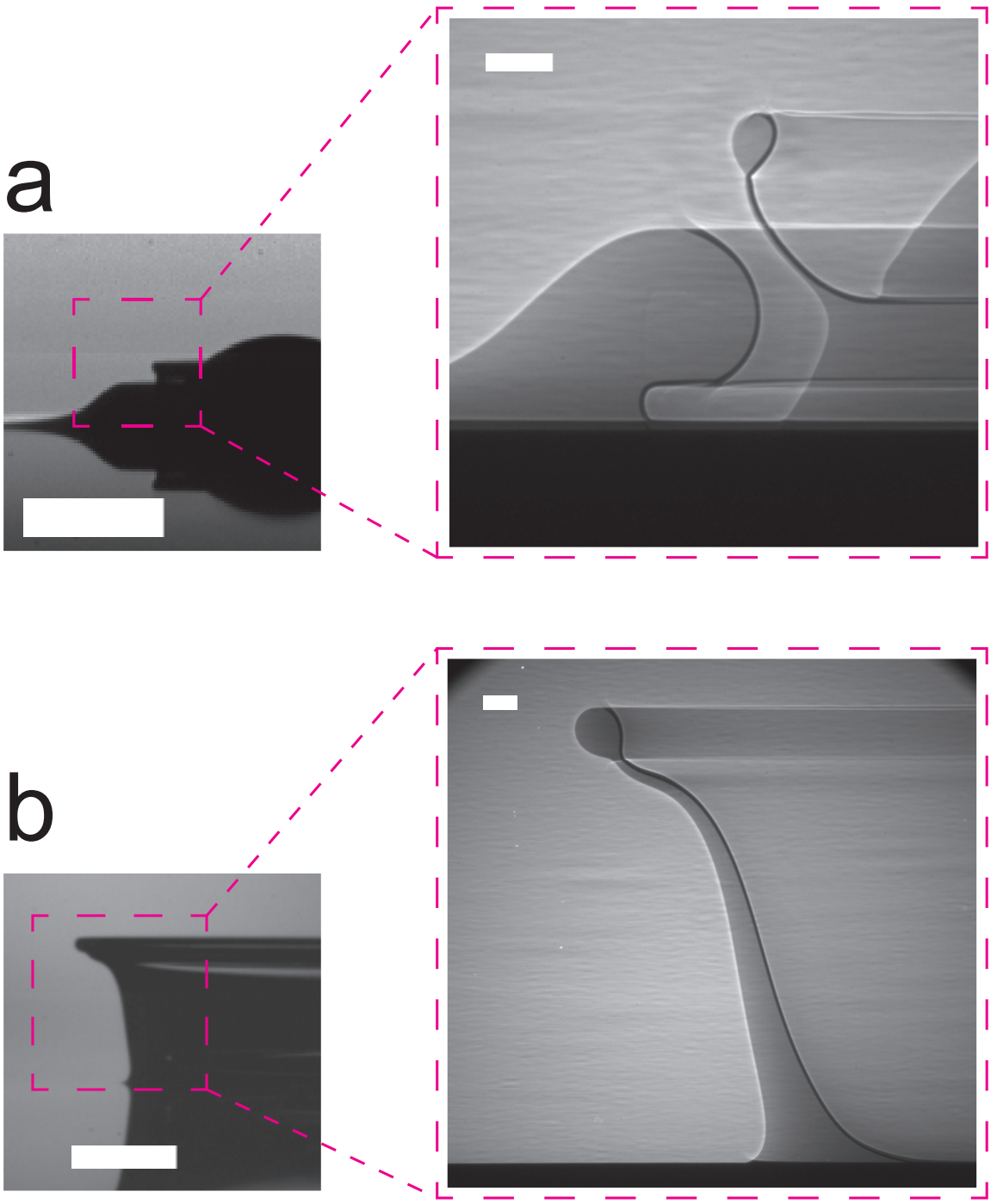

Figure 2.1: Comparison between optical images (left) and X-ray images (right). Scale bar: 1 mm for optical images, 100 μm for X-ray images.

variations. The relatively high X-ray energy (∼13 keV) utilized in our experiment ensured that the image contrast at the liquid-air interface was mostly dominated by phase contrast instead of absorption contrast (*Fezzaa and Wang* [2008a]). The in-

tensity changes gradually in the bulk of liquid (due to the absorption contrast) and abruptly at the boundary (mainly due to the phase contrast), which is signified as a pair of black and white fringes that correspond to the loss and the gain of intensity, respectively.

2.2 Experimental setup

We utilized the X-ray phase contrast imaging to study drop impact events at beamline 32-ID-B, Advanced Photon Source (APS), Argonne National Laboratory. The APS is a national synchrotron-radiation light source; electrons circulate inside the storage ring at nearly the speed of light, the period of the circulation is 3.68 μs, and the current inside the ring is 100 mA. The X-ray is generated when the electrons pass through an array of magnets, usually called "undulators", and emit radiation. With a precisely timed shutter, we released a horizontal beam of X-ray with uniform intensity (whose cross section is about 1.5 mm in width and 2 mm in height) into the impact site at a predesignated time. The X-ray beam penetrates the impact drop and the lamella with its phase modulated by the liquid-air interface, and then hits a scintillator far away from the impact site. At the same time, a high speed camera captures the image on the scintillator showing the cross section of the modulated X-ray beam. Each X-ray image was integrated over a period of time that is on the order of 500 ns, a very short time compared to the typical timescale of the impact (1 ms); the image is therefore free of motion-blur.

With enhanced contrast at interfaces between liquid and air, the X-ray imaging technique is capable of obtaining more accurate and interpretable data than optical imaging methods. The crown splash was studied as a simplest type of drop impact with only one jet formation: the lamella. We obtained a time-evolution of the boundary between the lamella and the surrounding air (Fig 2.1b), which can be compared to numerical simulations. We acquired reliable data of the lamella thanks to a great

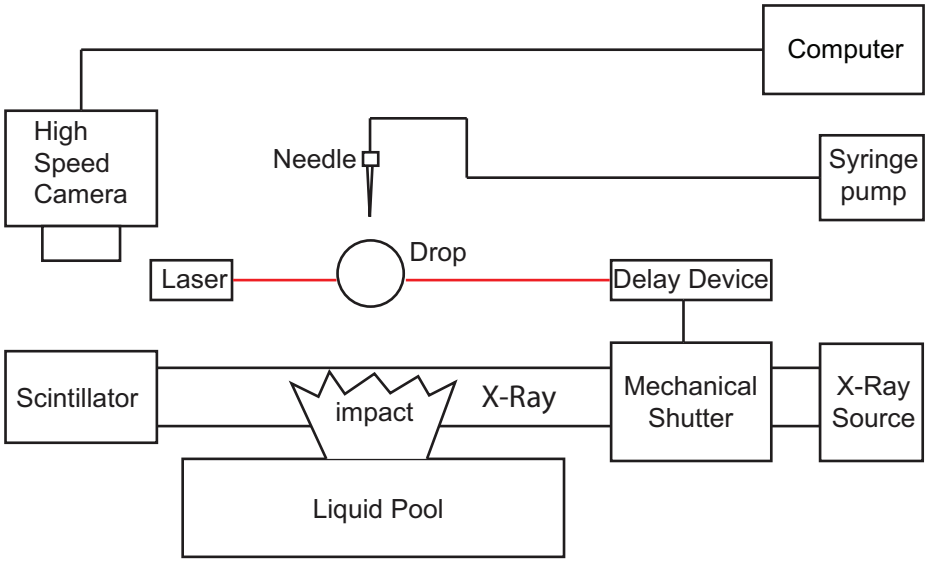

Figure 2.2: Experimental setup for X-ray phase contrast imaging on drop impact

improvement in image quality over previous studies. We also studied a variety of features related to the problem using the same technique.

2.3 Procedure for data processing

The X-ray images provide the cross sections of lamella at various times for an individual impact event (Fig 2.3). Due to the axisymmetrical nature of the lamella, the cross section is sufficient to reconstruct the time-evolution of lamella in a 3D space. We refer to this cross section as the *profile* in the following discussions.

The first step in data processing is the extraction of profile from original images using an edge detection algorithm. Next, since the extracted profiles are represented in a coordinate system defined by the picture frame, a proper translation is required so that all profiles fit into one coordinate system originated from where the bottom of the drop first touches the layer surface. The result is shown in Fig 2.3.

A simplification scheme was introduced to describe the complex motion of the lamella. The basic idea is to represent the motion with a centerline what we call the *backbone*. The backbone as a one-dimensional curve is a fairly accurate way to

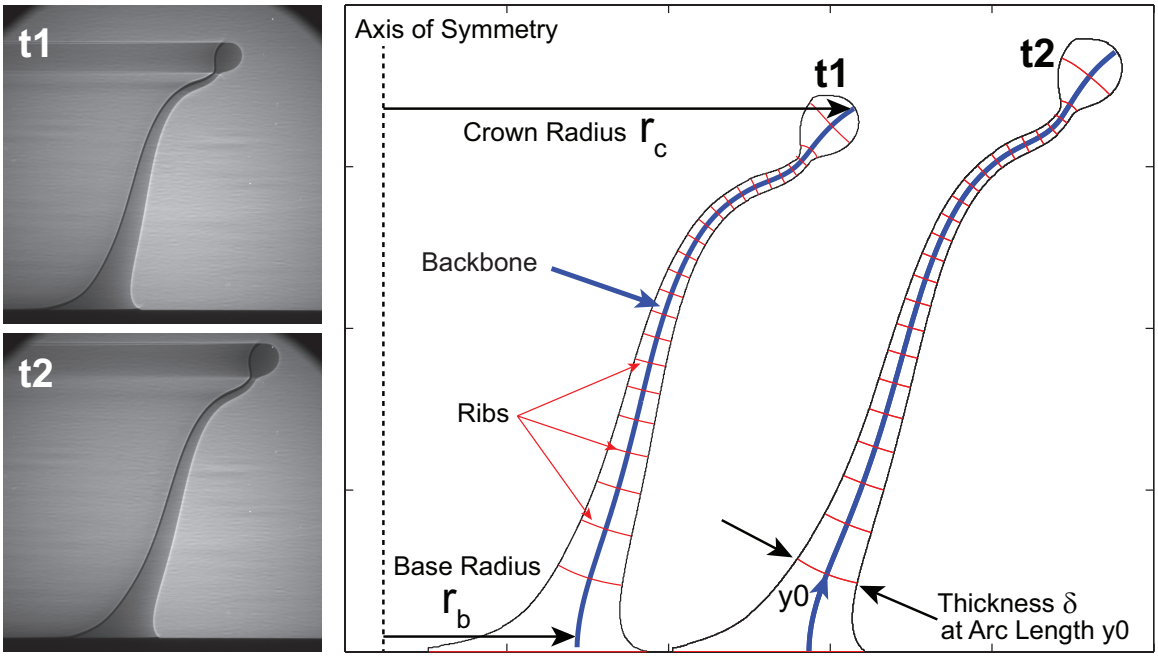

Figure 2.3: Original images (left) and grids on extracted profiles (right) for same impact at different times showing backbone (blue) and ribs (red), impact axis shifted to better illustrate definition of crown radius and base radius.

represent the lamella because of its long and thin shape. However, the backbone does not carry any thickness information of the lamella. To complement the backbone, we created a series of lines, or the *ribs* that are perpendicular to it. Backbone and ribs slice lamella into small segments, which we refer to as the *gridding scheme*. The technical details of the gridding scheme are discussed below.

The gridding scheme is based on Schwarz-Christoffel (SC) mapping; I give a brief introduction on this technique. For a polygon P with complex vertices $w_1, ..., w_n$ given in counter-clockwise order, each vertex w_k corresponds an exterior turning angle $-\beta_k\pi$, or interior angle $(1-\beta_k)\pi$. We have

$$\sum_{k=1}^{n} \beta_k = -2 \tag{2.1}$$

Let $\mathbb{C}^+$ denote the open complex upper half-plane, and define f on $\mathbb{C}^+$ by

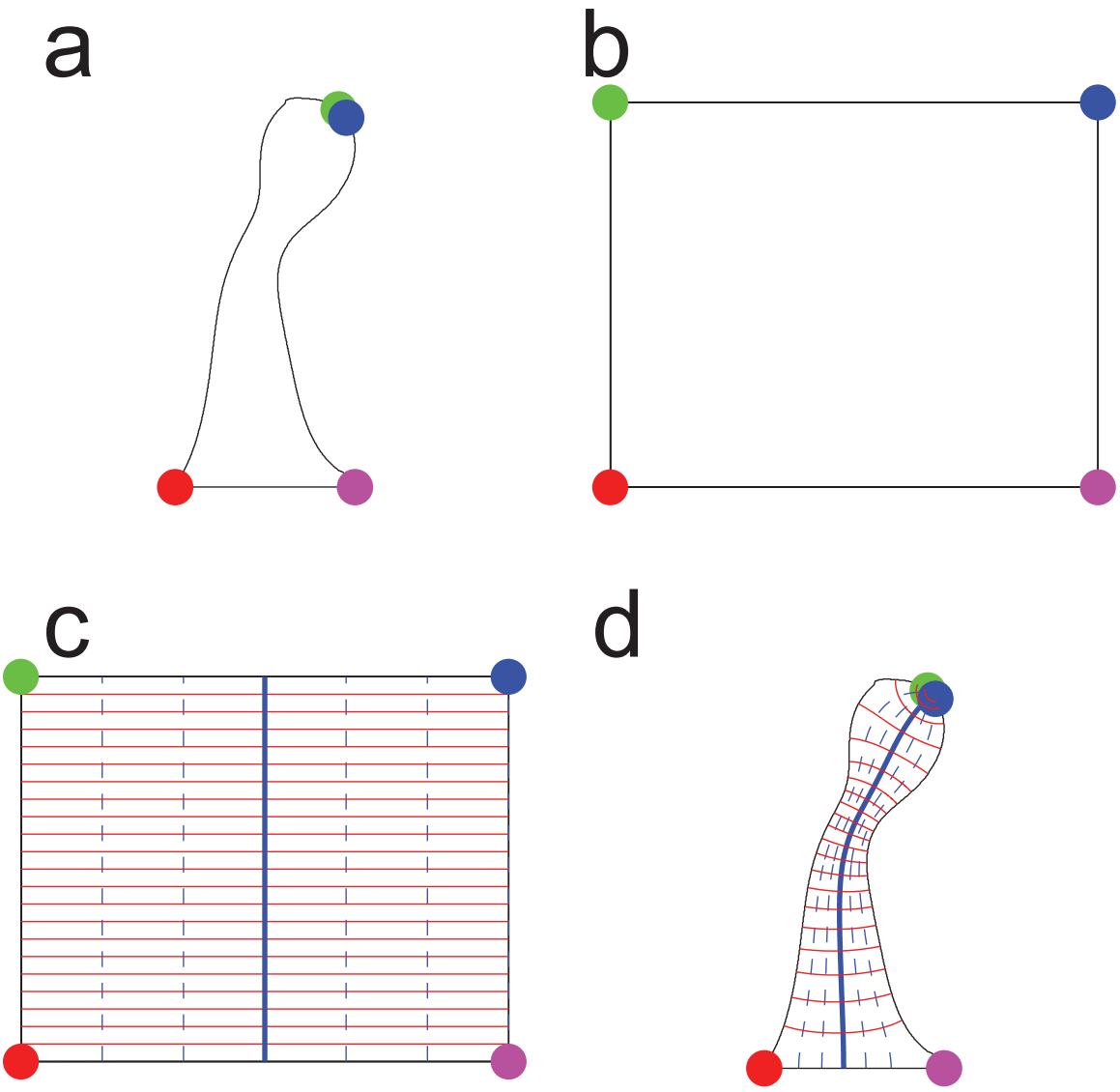

Figure 2.4: Obtaining the backbone and the ribs. a: Extracted profile with four selected points, b: SC mapping turns every point inside original profile into a rectangle and four points into vertices, c: A uniform grid put onto the rectangle, d: Grid mapped back to original space via reverse SC mapping. Solid blue: backbone; Solid red: ribs

$$f(z) = a + c \int_0^z \prod_{k=1}^{n-1} (s - x_k)^{\beta_k} ds \tag{2.2}$$

for some real $x_1, ..., x_{n-1}$ satisfying

$$x_1 < x_2 < ... < x_{n-1} < x_n = \infty \tag{2.3}$$

and complex constants a and c. Equation 2.2 is known as the *Schwarz-Christoffel formula*. The *fundamental theorem of Schwarz-Christoffel mapping* states that every function which maps $\mathbb{C}^+$ conformally onto interior of polygon P can be expressed in the form of Equation 2.2 (*Henrici* [1974], Thm 5.12 e).

Composing Equation 2.2 with standard conformal maps leads to variations of the Schwarz-Christoffel formula for mapping from other domains, such as a unit disk or a square. In our program, we mapped a polygon that represents the shape of the lamella into a rectangle using a MATLAB tool box developed by *Driscoll* [1996].

We start off with the original profile in Fig 2.4a and approximate it with a polygon by placing N points along the profile with equal distance. We chose $N = 80$ as a reasonable compromise between the fidelity to original geometry and the computational complexity. Next, we specify four points colored in Fig 2.4b to be mapped into four vertices of the rectangle. Two points are ends of the base of profile, the other two are neighboring points where the backbone ends.

Schwarz-Christoffel mapping turns the polygon into a rectangle, with four selected points mapped to its corners. We then divide the rectangle with a uniform grid that represents the backbone and the ribs in the mapped space. The horizontal lines (red) of the grid correspond to the ribs, the vertical lines (blue) the backbones. We are interested in all ribs but only the middle backbone (solid blue) that dissects the profile longitudinally into two equal halves. Finally, we find the counterparts of the ribs and the backbone in the original space with a reverse Schwarz-Christoffel mapping.

2.4 Limitations of the method

Like any other experimental technique, the X-ray phase contrast imaging technique comes with several limitations. The first and foremost limitation is the field of view determined by the size of cross section of the beam, which is limited to 2 x 1.5 mm in our experiments. For high impact velocities (on the order of 1 m/s), the spatial extent of the evolution exceeds this dimension, to as far as 10 mm. Therefore it is impossible to image a complete evolution in one video sequence. We mitigated the problem by shifing the impact site between video capturing sessions. As a result, various stages of the evolution were captured in different video sequences, which can then be combined to show the entire evolution. The combination of the sequences is, however, not straightforward. The major difficulty is to determine the impact center without seeing it directly in the image. We overcome the difficulty by comparing X-ray images with pre-recorded optical images, from which we deduce the information such as the impact center and the time after impact.

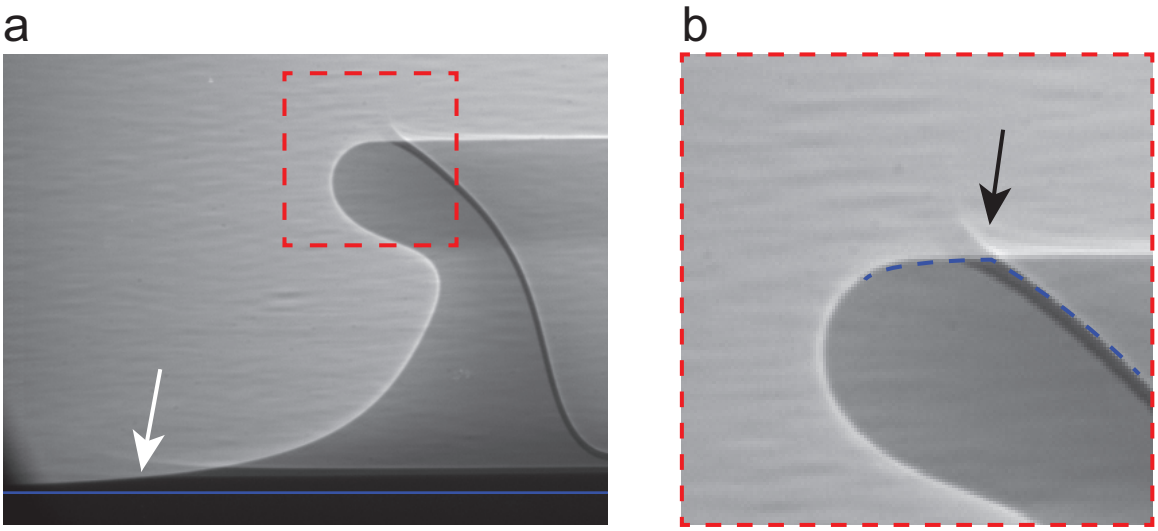

Figure 2.5: Left: meniscus effect extends outside frame, blue solid line represents original layer surface, curve due to meniscus is ignored beyond the location indicated by white arrow. Right: amplified top portion of the lamella with overshooting fringes (black arrow), blue dashed line indicates our choice of liquid-air boundary.

The second limitation is related to black and white fringes that come with the phase contrast effect. As seen in Fig 2.5, the black fringe dominates the inside of the lamella (relative to the impact center), while the white fringe is more significant on the outside. This is an effect due to differences in the curvature of the lamella, which causes loss and gain of the intensity of X-ray. The real liquid-air boundary can be anywhere inside the fringe. Although the thickness of both fringes is insignificant compared to the thickness of lamella, an uninformed choice of the exact location of boundary can bring certain errors. In a typical X-ray image, the thickness of two fringes combined is about 4 pixels, while the thickness of lamella is usually ten times of that. We choose the boundary to be the inner side of the white fringe and the outer side of the black fringe (Fig 2.5). The upper limit of the error due to our choice is about 10%. In many cases, it is the volume of liquid in the lamella that we care about, which brings down the estimated error to $10\%^3 = 0.1\%$.

We encounter a related issue at the top of the lamella, where the dominating white and black fringes meet without a smooth connection. Therefore we do not have direct visual information of the boundary at that specific location; we choose a reasonable, but uninformed, boundary as shown in Fig 2.5 b. This practice potentially brings some errors to the shape of the top portion of lamella, however, the errors are insignificant when we consider the entire lamella of a much larger size.

The meniscus effects (Fig 2.5 a) at the bottom of the lamella sometimes extends faraway beyond the picture frame, and therefore has to be cut off. For all images used in our data extraction, we ignored the lowest portion of the lamella up to a pre-defined height from the original layer surface. This ensures the consistency of our data and circumvents the problem from the meniscus effects. The practice also brings error in liquid volume that is insignificant compared to the bulk of lamella.

Safety issues prevented us from applying certain liquids at the Advanced Photon Source. One example is pyridine, which evaporates fairly fast and was denied usage at

APS due to lack of ventilation. We also observed the ionization of air due to passage of the X-ray, a fact that indicates possible safety issues when a flammable liquid is used.

2.5 Dynamics of lamella

We aimed to study the dynamics of the lamella in a crown splash using the gridding scheme introduced above. We created crown splashes using silicone oil (Clearco Products, μ=5.70 cP, ρ=0.918 g cm^{-3} and γ=19.4 dyne cm^{-1}) droplets of diameter D=0.169 cm. They were released above a uniform liquid layer of the same liquid. We changed the releasing distance from the layer to create four impact velocities ranging from 175 cm/s to 304 cm/s. For each velocity, we controlled the depth of liquid layer by letting h take different values: 0.1, 0.2, 0.4 and infinity (deep pool impact).

2.5.1 Crown radius

In the literature, the crown radius r_c was defined as the radial distance from the axis of symmetry to the rim at top of the crown, represented by the top position of backbone with our gridding scheme (Fig 2.3). The theory by *Yarin and Weiss* [1995] predicted the crown radius r_c to be

$$\frac{r_c}{D} = C(\tilde{t} - \tilde{t_0})^n \tag{2.4}$$

where D is the diameter of the drop, C and $\tilde{t_0}$ are variables dependent on impact conditions, and $n = 1/2$. They also fitted experimental data to the formula with n fixed and obtained a fairly good agreement with the theory. A slightly different n was reported as 0.43 in *Cossali et al.* [2004].

The expression suggests that when $\tilde{t}$=$\tilde{t_0}$, the radius of the crown is zero. Namely, the lamella emerges from the axis of symmetry, a scenario assumed by the authors

who did not have enough temporal resolution in their experiments. Our experimental technique was able to trace the lamella back to its emergence time at some distance r_{0c} from the axis of symmetry. Therefore we propose a modified version of the crown radius r_c:

$$\frac{r_c - r_{0c}}{D} = C(\tilde{t} - \tilde{t_0})^n \tag{2.5}$$

where the pre-factor C is determined by a best fit, r_{oc} and $\tilde{t_0}$ are obtained experimentally, and $n = 1/2$. We plotted the experimental data of r_c together with a best fit in Fig 2.6. The new formula describes the data fairly well. Therefore we are able to confirm the square-root dependence of r_c on time. This result is amazingly simple given the complex geometry at the top of the crown and the multiple surface tension related mechanisms such as the Taylor-Culick mechanism and the hoop stress in the rim.

For the same impact velocity, a greater layer depth corresponds to a generally slower expansion rate of the crown. This is consistent with the fact that there is more resistance from the pre-existing layer to slow down the propagation of the crown.

2.5.2 Base radius

The base radius r_b is defined by the distance from the axis of symmetry to the base of lamella and represented by the bottom position of the backbone in our gridding scheme (Fig 2.3). Based on a numerical simulation, *Josserand and Zaleski* [2003] claimed that r_b can be described as

$$\frac{r_b}{D} = 1.1\sqrt{\tilde{t}} \tag{2.6}$$

which is valid until intermediate times after impact ($\tilde{t} \approx 3$). We fit the dimensionless radius $\frac{r_b}{D}$ with the following formula:

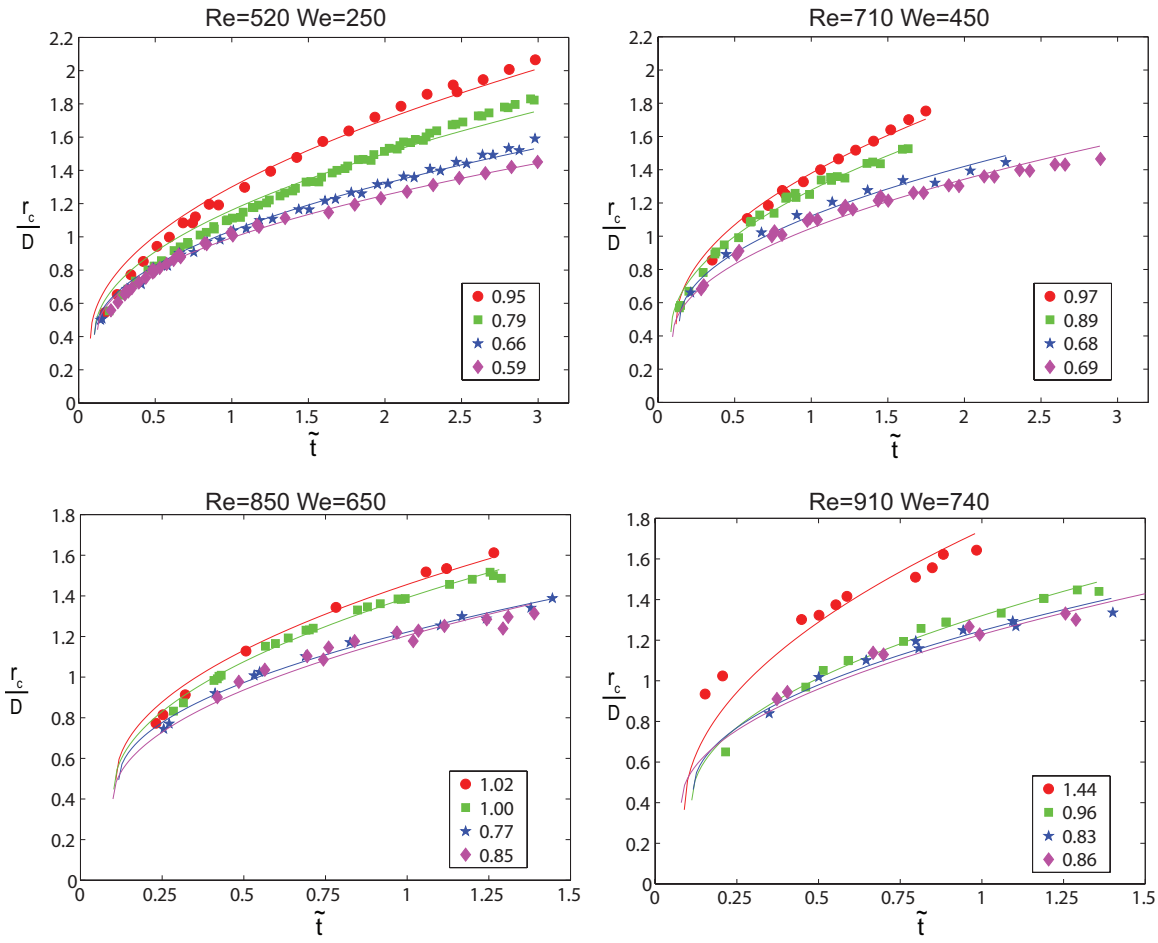

Figure 2.6: Dimensionless crown radius r_c/D fit to Equation 2.5 at four different dimensionless depths for each velocity: 0.1 (circles), 0.2 (squares), 0.4 (stars) and infinity (diamonds) with pre-factor C in the box. Solid line is the best fit

.

$$\frac{r_b}{D} = B\tilde{t}^n \tag{2.7}$$

Our data suggests an exponent n of 0.4 instead of 1/2 and a pre-factor B that is weakly dependent on impact conditions. The relationship is valid until intermediate times after impact.

2.5.3 Thickness of lamella

Cossali et al. [2004] attempted to measure the thickness of lamella, but they could

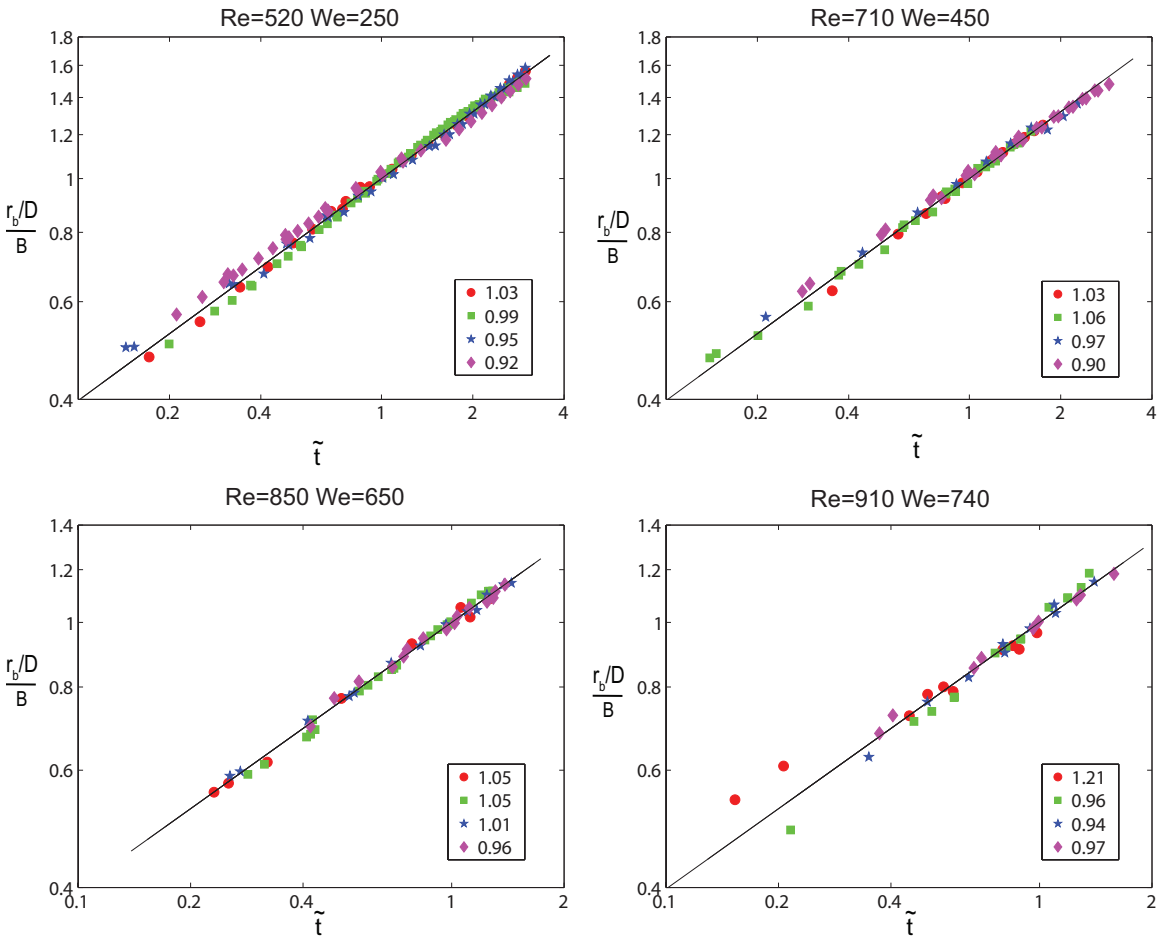

Figure 2.7: Dimensionless base radius r_b/D fit to Equation 2.7 and scaled by prefactor B (value shown in the box) at four different velocities. Four dimensionless depths h for each velocity: 0.1 (circles), 0.2 (squares), 0.4 (stars) and infinity (diamonds). Solid line represents $\tilde{t}^{0.4}$

.

only do so by viewing the crown from above, which rendered some ambiguous results. Their pictures taken from the side suffered from the optical artifacts that made them impossible to extract the thickness information from.

The X-ray technique deployed in our studies improved the side-view pictures significantly so that we obtained reliable data on the thickness of the lamella. Our first finding is that the thickness of the lamella varies significantly with the location: the lamella is generally thinner at top and thicker at bottom (Fig 2.3). The dependence on the location complicates the comparison between impacts of different parameters. To simplify the problem, we define the lamella thickness to be the value at a fixed arc

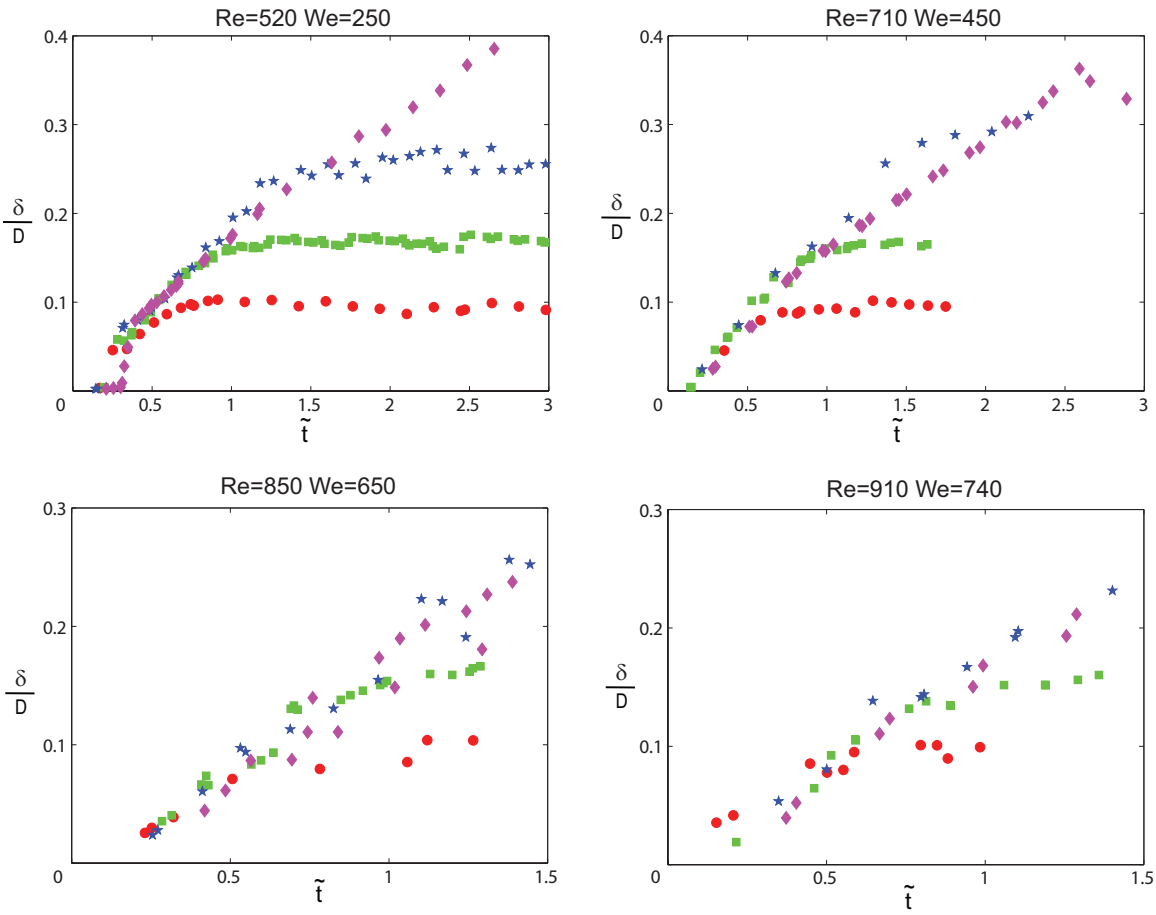

Figure 2.8: Dimensionless thickness of lamella δ/D at $y0 = 0.02$ cm at four different velocities . Four dimensionless depths h for each velocity: 0.1 (circles), 0.2 (squares), 0.4 (stars) and infinity (diamonds).

.

length $y0$ from the layer surface for all experiments. For the same impact velocity, we controlled the layer depth and plotted the thickness versus time (Fig 2.8).

For the same impact velocity, the thickness of lamella grows linearly at the same rate regardless of the layer depth. After a certain period of time, it remains constant for as long as our observations lasted. The terminal thickness of lamella is a increasing function of the depth of the pre-existing layer. This is consistent with the fact that there is more liquid to be pumped into the lamella with thicker layers. However, the curves converge at very early times, which shows that the influence from the depth of the layer takes a certain amount of time to affect the evolution. The dimensionless depth h is not important before that time.

2.5.4 Velocity of lamella

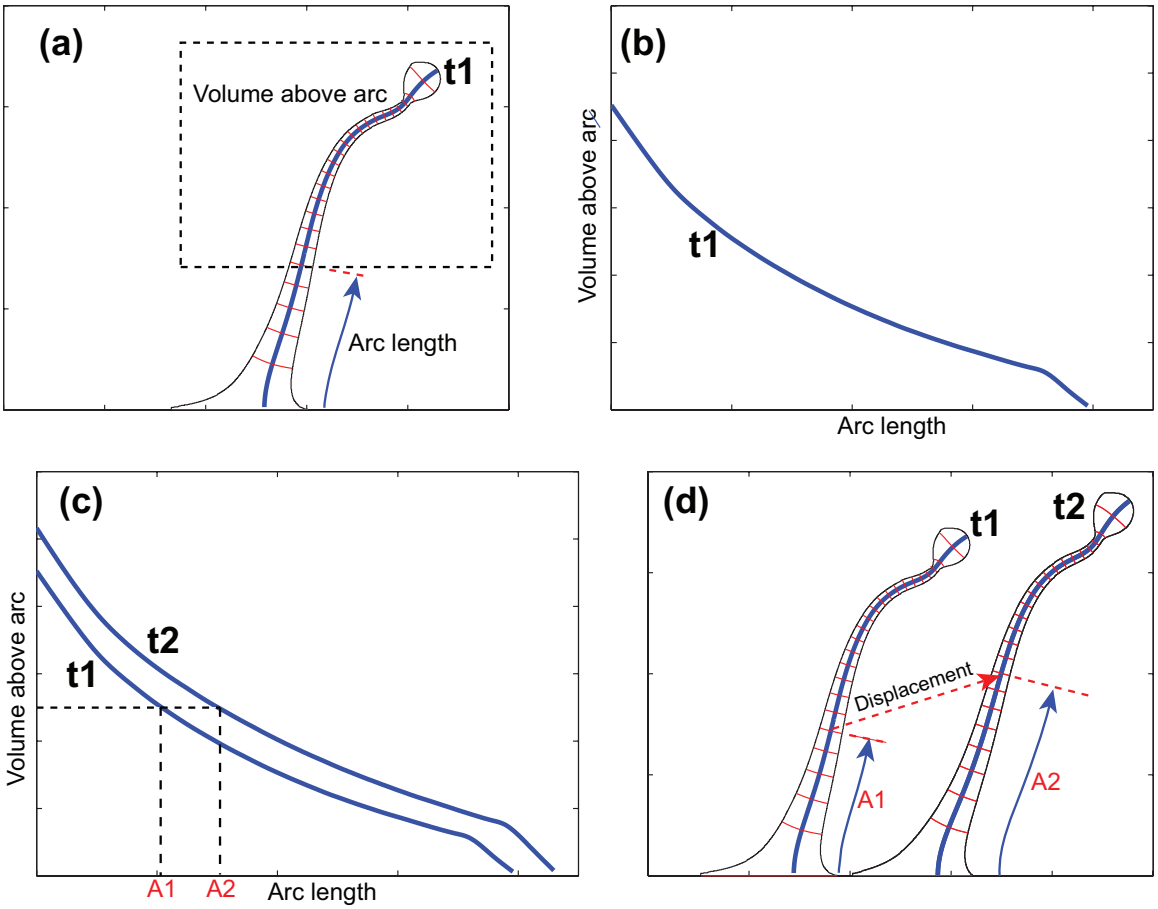

Figure 2.9: Procedure for finding velocity at an arbitrary location on lamella

The calculation of the velocity field inside the lamella was confined to numerical simulations (*Josserand and Zaleski* [2003],*Coppola et al.* [2011]). Some theories were proposed to calculate the velocity where the lamella is propelled upward (*Yarin and Weiss* [1995],*Roisman and Tropea* [2002]). There was no experimental result regarding the flow inside the lamella.

In our gridding scheme, we use a centerline (backbone) to represent the motion of lamella. We assume that the backbone is a good representation of the whole lamella and calculate the velocity field along the backbone in a fashion illustrated in Fig 2.9. For an arbitrary point on the backbone at time $t1$, we denote its location by the coordinate *arc length* $A1$ from bottom of the backbone and calculate the total volume

above it (*volume above arc*). The volume was calculated in a 3D space considering the axisymmetry of the lamella. As the lamella evolves, the volume of liquid above this point must be conserved since there is no source or sink. For the next frame at time $t2$, we find the arc length $A2$ at a point that has the same volume of liquid above it. Therefore, the point must has moved from $A1$ to $A2$ during time $t2 - t1$. The velocity of this particular point can thus be calculated accordingly. We performed calculations for many points along the backbone and obtained the velocity field inside lamella.

There are two important notes about our calculations above. First, we ignore the thickness of the backbone and assume all points on a rib perpendicular to the backbone have the same velocity. This assumption is justified by the long and thin shape of lamella, therefore the velocity variation on a rib is small compared to that of the backbone. Second, the velocity calculated for time period $t1$ to $t2$ is averaged. Since the inter-frame time $t2 - t1$ is very small compared to the timescale of the evolution, the averaged velocity is a good approximation to the instant velocity.

Fig 2.10 shows the velocities along the backbone for various times after the impact. Both the horizontal and vertical velocities increase spatially from the bottom of lamella until the thinnest portion of it, which we define as the *neck* of lamella. Since the top portion emerges earlier than the bottom portion, the spatial distribution of the velocity can be translated into a temporal distribution. In other words, the emergence speed of lamella decreases with time. The velocity monotonically decreases from the neck of lamella to the rim. This is consistent with the fact that this portion of the lamella is pulled back by the surface tension similar to the Taylor-Culick mechanism. The rim is traveling backwards relative to the lamella, which lowers the velocity measured in the lab frame.

In particular, the horizontal velocity at bottom of the backbone (where the arc length is zero) is defined as the base velocity v_b. It determines the rate of lamella

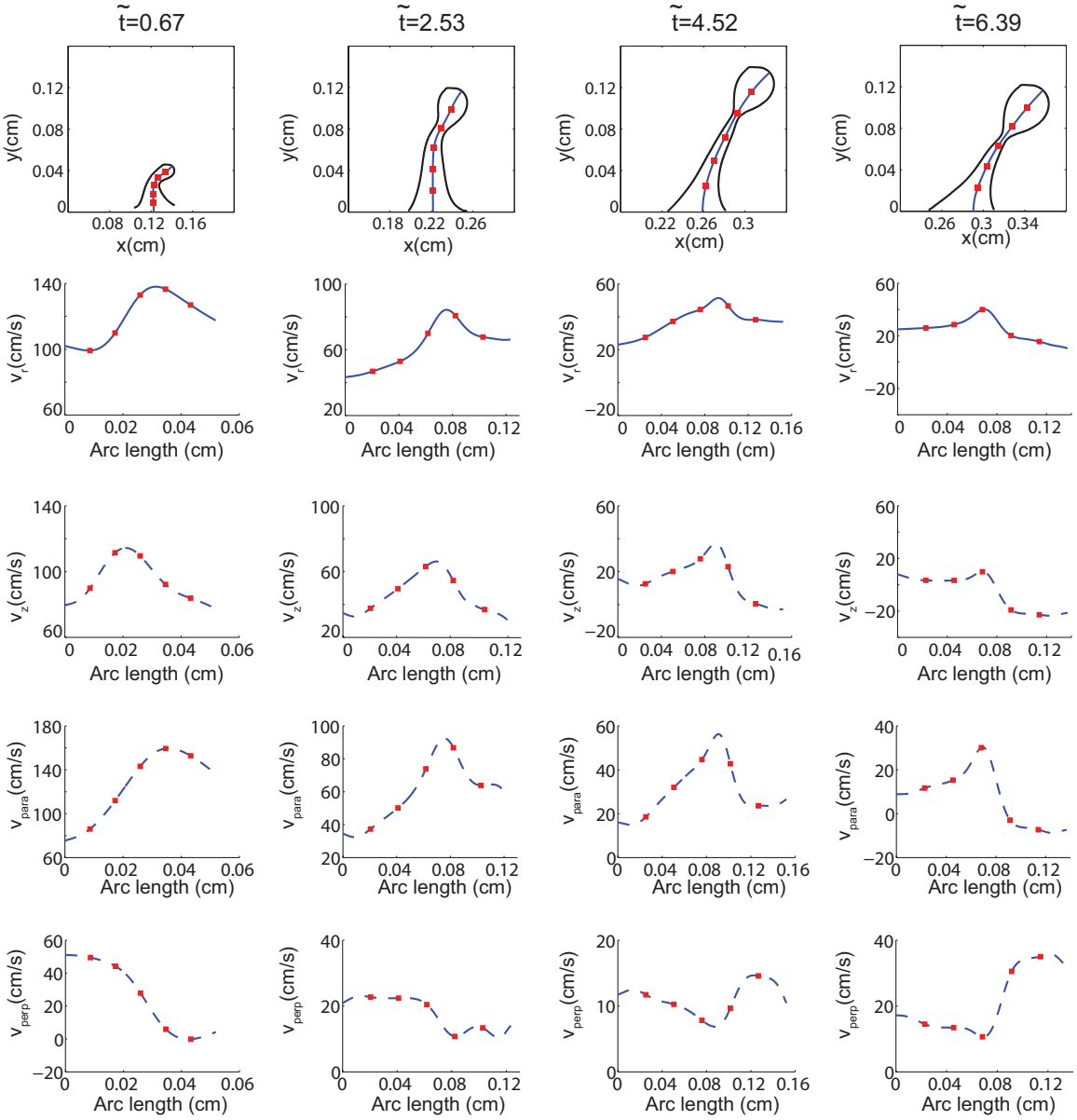

Figure 2.10: First row: profiles of lamella at different times after impact for $U = 175$ cm/s, $Re = 520$, $We = 250$ and $h = 0.2$ with backbone. Second to fifth row: horizontal (v_r)velocity, vertical (v_z) velocity, velocity component parallel to the backbone (v_{para}) and velocity component perpendicular to the backbone (v_{perp}) at various arc lengths. Red dots represent the same set in a column.

.

expansion and is therefore important to understanding the dynamics of lamella. We fit measurements of base velocity v_b to the following equation:

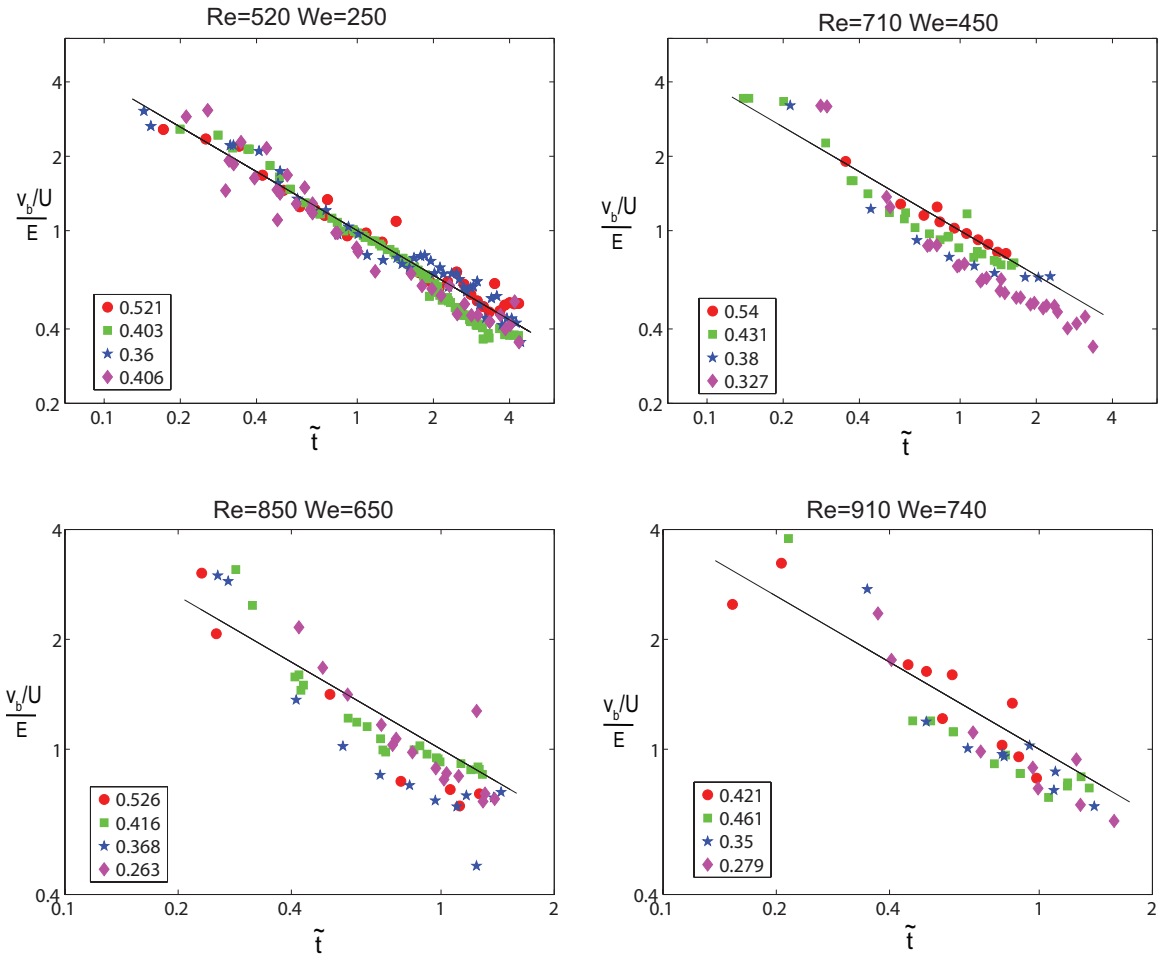

Figure 2.11: Dimensionless velocity of the base v_b/U fit to Equation 2.7 and scaled by pre-factor E (value shown in the box) at four different velocities . Four dimensionless depths h for each velocity: 0.1 (circles), 0.2 (squares), 0.4 (stars) and infinity (diamonds). Solid line represents $\tilde{t}^{-0.6}$

.

$$\frac{v_b}{U} = E\tilde{t}^n \tag{2.8}$$

where U is impact velocity and $n = -0.6$ is a best fit.

In a different approach, we obtain v_b independently by differentiating the base location r_b with respect to time. Indeed, since $r_b \sim \tilde{t}^{0.4}$, $v_b \sim \tilde{t}^{-0.6}$. Two methods produce consistent results with each other, which adds credibility to our calculations.

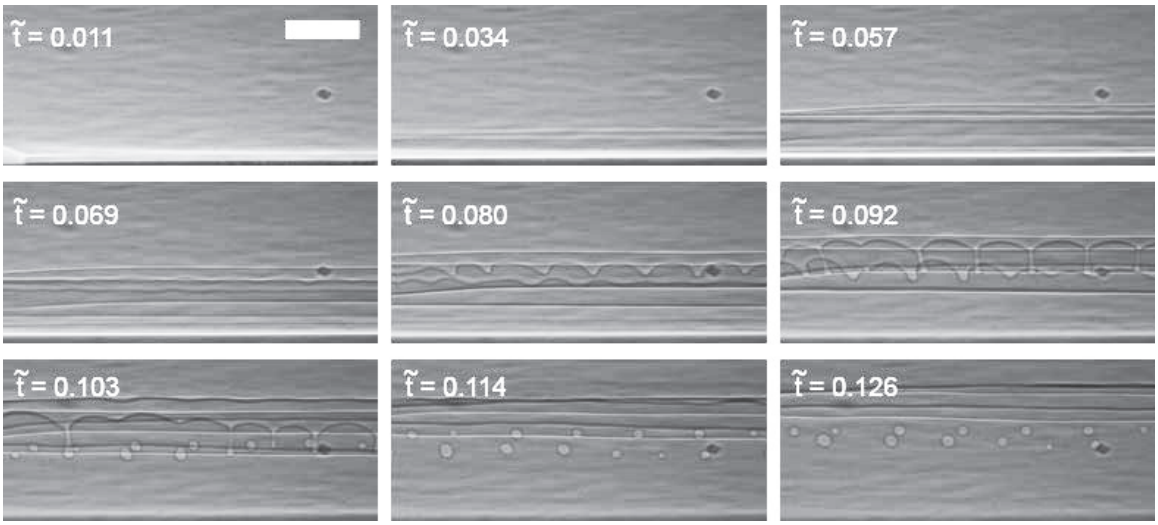

Figure 2.12: Development of instability on ejecta sheet from impact between liquid drop of water-glycerol mixture and a deep pool of same liquid at velocity $U = 190$ cm/s, $D = 0.2463$ cm, $Re = 3764$ and $We = 142$. Scale bar:100 microns

2.6 Miscellaneous studies

We imaged several other features related to the problem. Compared to the systematic study on lamella, results displayed here are less comprehensive. Nonetheless we obtained some interesting data and advanced our understanding on the capability of the experimental technique.

2.6.1 Instability on ejecta sheet

We have shown that the ejecta sheet can either break up into droplets or retract back to the drop depending on the impact parameters. With the high-amplification of the X-ray technique, we were able to capture the corrugation of ejecta sheet viewing from the side at a high image resolution. We found a dominant wavelength of the corrugation and many tiny bubbles trapped by the interaction between the ejecta sheet and the drop.

2.6.2 Bubble trapped under drop

As mentioned in Chapter I, a liquid drop deforms just before the impact due to a pressure gradient from the drainage of air and traps a bubble between the drop and the layer. *Thoroddsen et al.* [2003] observed an undulation resembling a pearl necklace during the contraction of the bubble in water drop impacts. In our experiments with a water-glycerol mixture, we noticed a similar behavior of the air bubbles.

Compared to the optical images in *Thoroddsen et al.* [2003], X-ray images are sharper thanks to the virtually infinite depth of field. They also provide more contrast inside the bubble that leads to easier interpretation as opposed to a completely black interior in the optical images.

2.6.3 Interface between liquid drop and layer

The X-ray phase contrast imaging technique is based on the refraction of X-ray on the interface between two materials of different indices of refraction n, such as the liquid and the air in our experiment. We do not observe the interface between the drop and the layer when they are made of the same liquid, and therefore have same n.

When we replaced the liquid in the layer with another liquid of a different n, the interface between liquids appeared (Fig 2.14). The shape of the interface is similar to the vortices predicted numerically by *Nikolopoulos et al.* [2004], *Coppola et al.* [2011] and *Thoraval et al.* [2012].

2.6.4 Particle image velocimetry

We attempted a PIV measurement based on the X-ray technique instead of optical imaging technique. Surprisingly, X-ray based PIV measurement increases the difficulty of tracking particles for the following reasons. Optical imaging technique has a pre-determined depth of field and only images a layer of particles on the axis

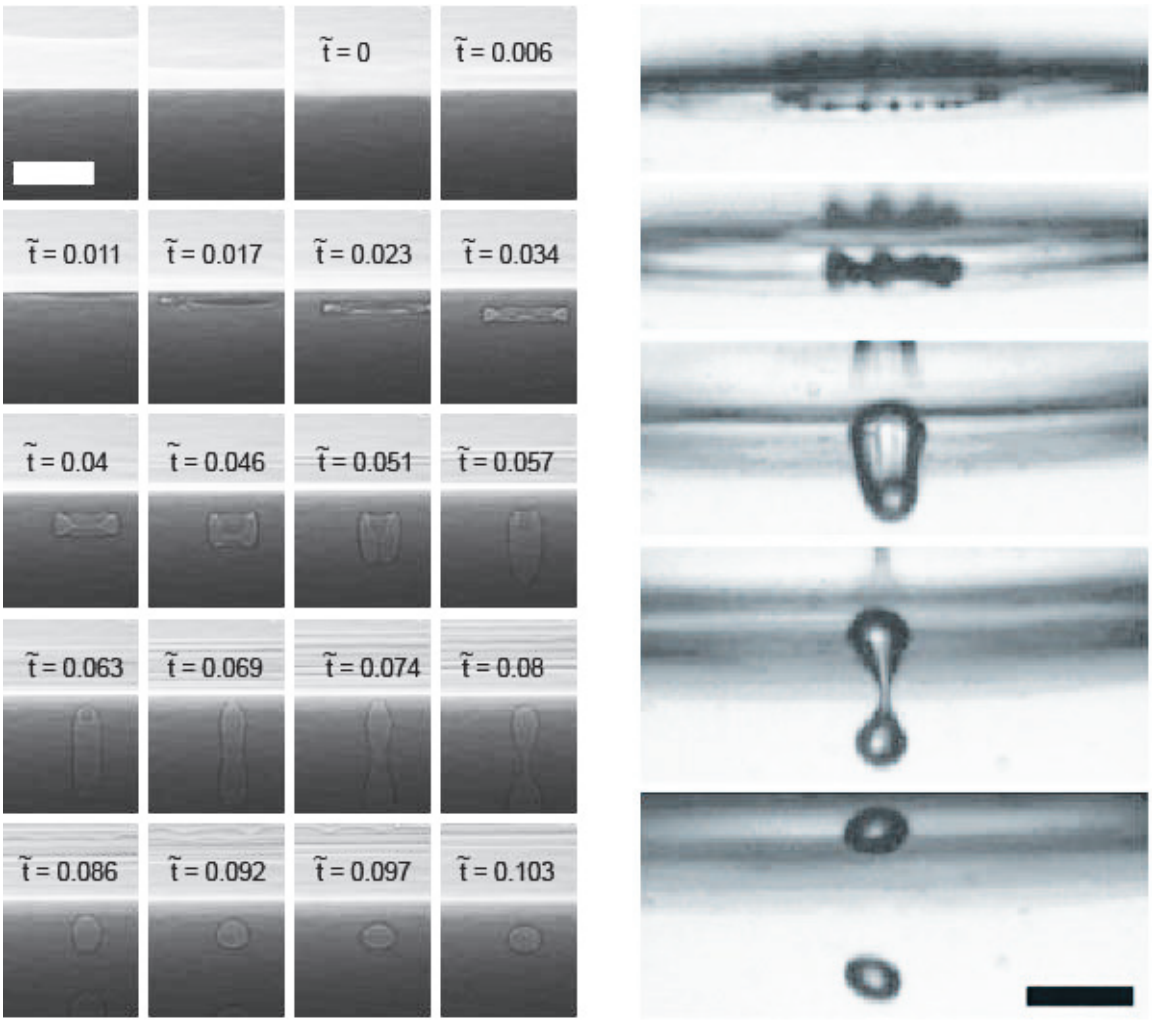

Figure 2.13: Left: X-ray images of bubble trapped underneath drop of water-glycerol mixture impacting a deep pool of same liquid. $U = 190$ cm/s, $D = 0.2463$ cm, $Re = 3764$ and $We = 142$. Scale bar:100 microns; Right: optical images of bubble from *Thoroddsen et al.* [2003], $U = 49$ cm/s, $D = 0.424$ cm, $Re = 138$ and $We = 14$. Scale bar: 500 microns

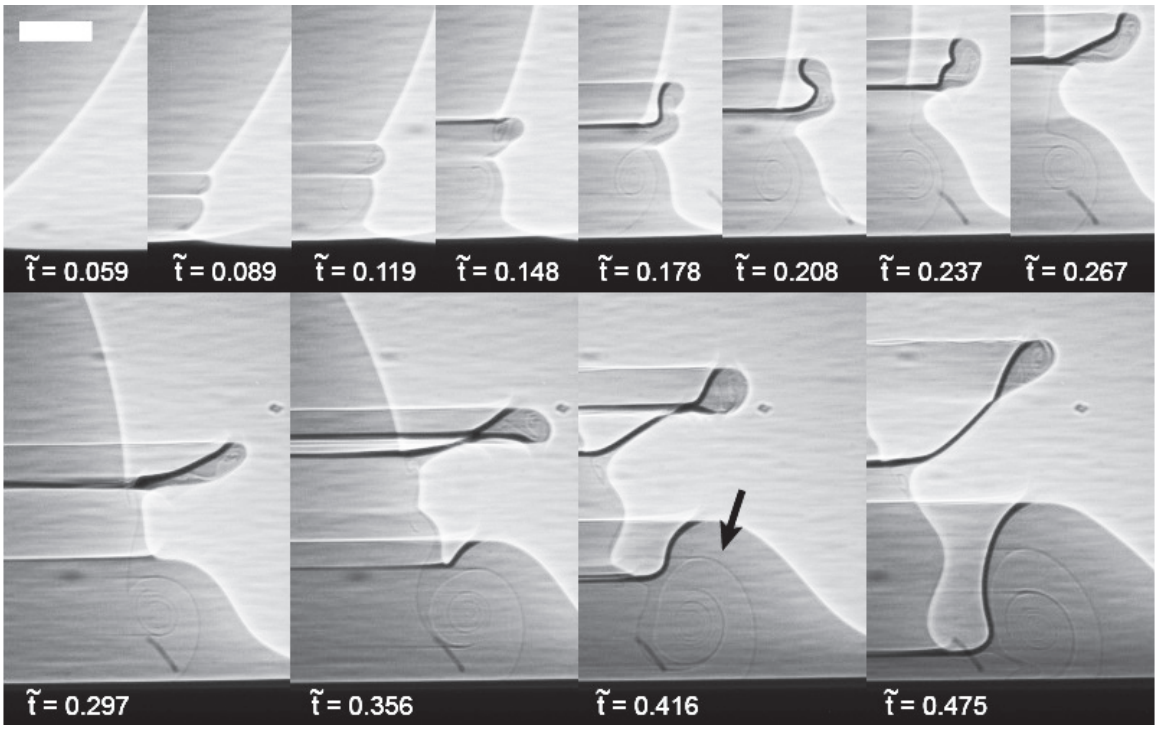

Figure 2.14: Interface (black arrow) between two fluids after a drop of SO1 of diameter $D = 0.1645$ cm hitting a deep liquid pool of SO2 at velocity $U = 220$ cm/s . Scale bar:100 microns

perpendicular to the focus plane. The tracks of particles provide the flow information in $x - y$ plane (image plane), while the location of the imaged layer has a coordinate on z axis. One can therefore obtain a 3D visualization of the flow. With X-ray however, the depth of field is virtually infinite: every particle in its path is sharply imaged (see Fig 2.15). This has two consequences: first, there are a lot more particles which could potentially increase the difficulty in tracking one specific particle; second, we lost information on z axis since there is no way to differentiate particles at various z locations.

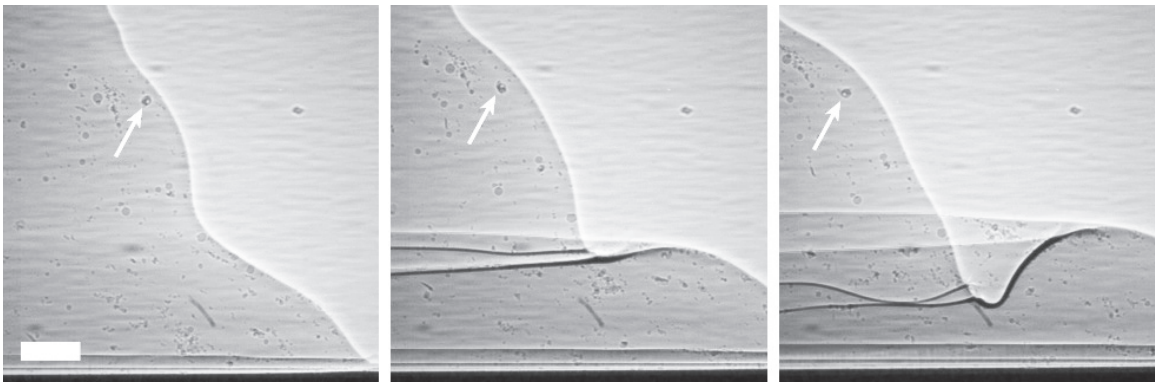

Figure 2.15: Drop impacts with particles for PIV measurement. White arrow indicates a trackable particle. Scale bar:100 microns

CHAPTER III

Wavelength selection in crown splash

3.1 Introduction

Figure 3.1 shows the end stage of a crown splash in which the rim of a sheet-like jet breaks into secondary droplets distributed almost uniformly along its perimeter. The name of the splash derives from the resemblance of this final stage to a crown with equally spaced tines, as exemplified in Edgerton's iconic photograph *Milk Coronet* (*Edgerton* [1977]). The events culminating in a crown splash begin with a smooth cylindrical sheet-like jet extending outward and upward. The leading edge of this jet (i.e. the rim) is pulled by surface tension towards the sheet (*Culick* [1960], *Taylor* [1959]), and grows in diameter as it entrains fluid from the sheet. Next, the rim develops a symmetry-breaking corrugation, and in a much later nonlinear phase of the original instability, the rim's crests sharpen into jets which pinch off to form secondary droplets.

Due to the high speed and small scale structure of a splash there are few quantitative time-resolved observations of crown formation (*Allen* [1988], *Chandra and Avedisian* [1991], *Yarin and Weiss* [1995], *Mundo et al.* [1995], *Cossali et al.* [1997], *Fujimoto et al.* [2002], *Leng* [2001], *Thoroddsen* [2002], **?**], *Roisman et al.* [2007], *Krechetnikov and Homsy* [2009]). This is true in particular for the earliest stages of the growth of the rim, during which perturbations of the rim are extremely small.

Basic questions regarding the origin and evolution of splashes remain unanswered (*Yarin* [2006]). Foremost among these is: what mechanism leads to the generation of secondary droplets?

From the earliest investigations, the leading suspect for the mechanism responsible for secondary droplets was the Rayleigh-Plateau instability (*Rayleigh* [1878]), which causes cylindrical jets to break into droplets. *Worthington* [1879] experimented with tori of mercury on a solid surface to address this question, but was unable to directly compare the number of ejected droplets with Plateau's theory. *Yarin and Weiss* [1995] cast doubt on the relevance of this mechanism based on timescale arguments, and noted that there is a discrepancy between the expected and measured number of ejected droplets. *Fullana and Zaleski* [1999] argued that the Rayleigh-Plateau instability is slowed prohibitively by the increase of the rim's radius with time. *Rieber and Frohn* [1999] found support for the Rayleigh-Plateau mechanism in computer simulations but only for large initial perturbations. *Bremond and Villermaux* [2006] analyzed rim instabilities for the lamella produced by impacting jets, and found the Rayleigh-Plateau instability to be the dominant mechanism.

Mechanisms other than Rayleigh-Plateau have been suggested for the generation of secondary droplets. *Yarin and Weiss* [1995] proposed a nonlinear amplification mechanism. *Gueyffier and Zaleski* [1998] argued for the Richtmyer-Meshkov instability. *Krechetnikov and Homsy* [2009] argued for a combination of the Richtmyer-Meshkov and Rayleigh-Taylor instability.

We think there are two reasons why the symmetry breaking instability of a splash has been interpreted in so many, seemingly contradictory ways. First, depending on parameters, there exist many different splash morphologies (*Deegan et al.* [2008]), which may result from different instabilities. Second, there is a lack of quantitative experimental data that characterizes both the symmetry breaking as well as the base state on which the instability grows.

Here we focus on a parameter regime in which the crown splash grows from an initially smooth sheet formed on impact into a thin layer of the same fluid at moderate speed. We image the instability that appears on the leading edge of the ejected sheet at multiple times onward from ≈ 100 μs after impact for multiple impact speeds and layer depths. From our images we extract the spectrum of the instability, and compare this to the various mechanisms that are cited in the literature. Our results for peak position and width of the spectrum are in excellent agreement with Rayleigh-Plateau mechanism.

The chapter is formatted as follows. Section 3.2 describes our experimental setup and procedures. Section 3.3.1 describes our observations of the morphology of splashes. We show that highly regular crown splashes in thin layers occur only for low Reynolds number. Section 3.3.2 describes our experimental measurements of the instability spectra from still images of the rim's corrugation. For the majority of experiments the spectra at any given time after impact were produced from a single image; for our most precise experiments we averaged over ten spectra obtained at equal times. Section 3.4 describes a comparison of our data with a calculation based on the Rayleigh-Plateau instability. For our most precise measurements with averaged spectra the measured and calculated peak wavelengths agree within 5%. Section 3.5 describes a comparison of our experiments with other proposed mechanism such as Rayleigh-Taylor and Ritchmyer-Meshkov. Our measurements exclude these mechanisms. Section 3.6 discusses and summarizes our results in the context of other splashing studies.

3.2 Experimental Methods

Our experiments identified the parametric regime for crown splashes and measured the evolution of these splashes. A 10 cm diameter $\lambda/10$ glass optical flat, coated with an indium-tin oxide film to prevent the destabilization of the thin liquid films due

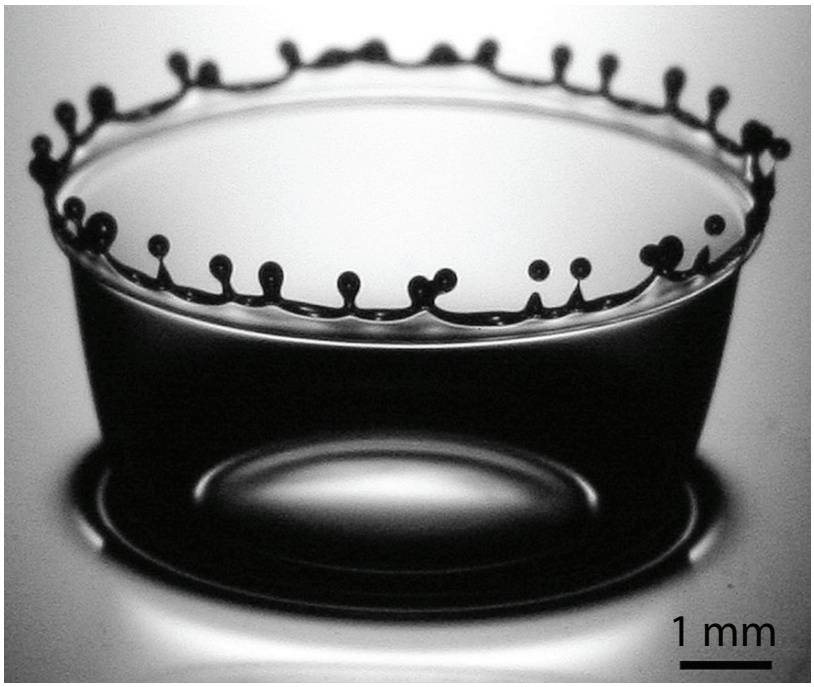

Figure 3.1: Crown splash (silicon oil: $Re = 966$, $We = 874$, $h = 0.2$).

static charge build up, was placed in a 15 x 15 cm container with a glass bottom. Fluid was added to the container until the optical flat was submersed, forming a film of height h above the optical flat, as shown in Fig 3.2. The orientation of the container was then adjusted so that the flat lay parallel to the fluid's surface to within 3×10^{-4} radians. The depth of the layer was varied between 100 and 400 μm depending on the experiment. A single drop of diameter D was released from a gravity fed 30 gauge hypodermic needle at fixed height above the liquid layer. The interval between drops was longer than 10 s, which ensured that the liquid layer fully relaxed between impact events. The drop struck the liquid layer with a velocity U normal to the surface.

The dimensionless parameters for describing droplet impact in the absence of a surrounding gas are the Weber number $We = \frac{\rho D U^2}{\gamma}$, the Reynolds number $Re = \frac{DU}{\nu}$, the Froude number $Fr = \frac{U^2}{gD}$, and the dimensionless fluid depth $h = H/D$, where g is the acceleration due to gravity, and ρ, γ, ν are the density, surface tension, and kinematic viscosity of the fluid, respectively. Past studies ignored the ambient gas and gravity on the basis that densities and viscosities of liquids are much higher than the

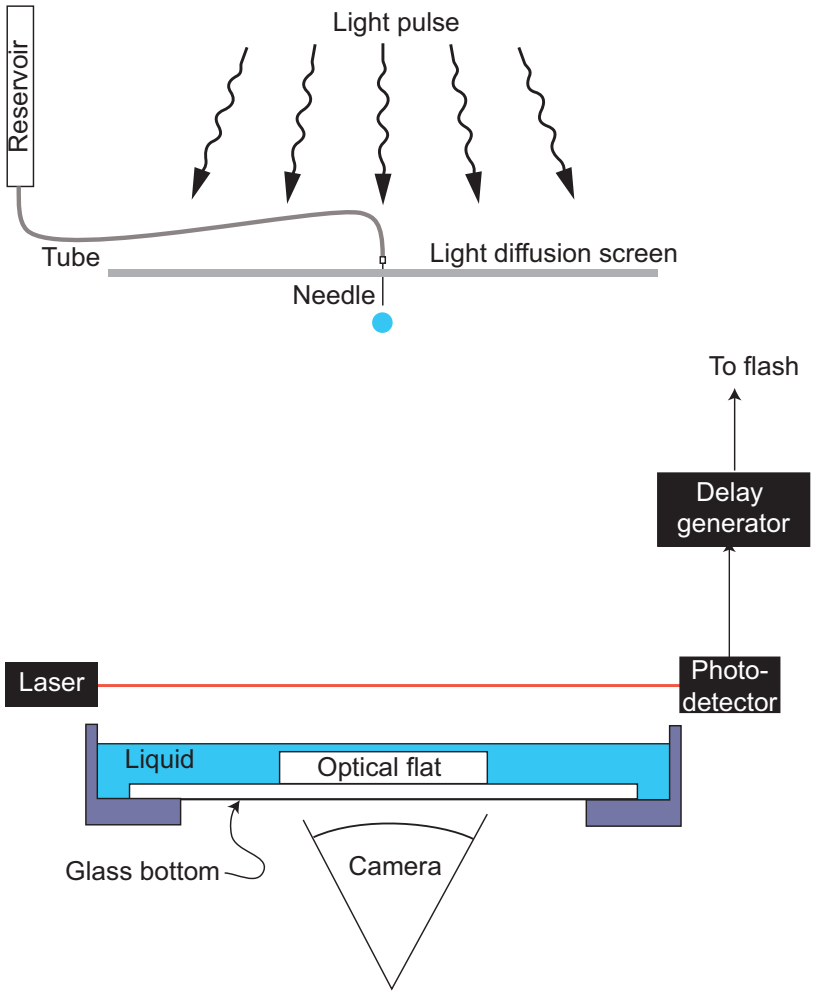

Figure 3.2: Apparatus for observing the evolution of crown splashes. A drop forms and detaches from a hypodermic needle held a fixed height above a thin layer of the same liquid. The needle is gravity fed from a reservoir. As the drop falls towards the liquid layer, it interrupts a laser sheet focused onto a photodetector which initiates a countdown on a delay generator. After a preprogrammed time, the delay generator fires a flash onto a diffusion screen, and a back-lit image of the impact event is recorded from below through the transparent substrate or from the side.

gas, and that the timescale for gravitational effects is long compared to the duration of a splash. We follow this practice here, and concentrate on the We, Re, and h. Nonetheless, we note that the recent work of *Xu et al.* [2005] found a significant influence of the ambient air on drop impact on a *dry* solid. We believe the effect of air to be much weaker in our experiment, since there is no moving contact line.

Our data on the morphology of splashes was obtained with a high speed camera (Phantom 5.0 or 7.3) viewing the impact from the side. Our data on the evolution of the rim was obtained from images simultaneously recorded through the glass substrates and from the side using digital cameras (Nikon D80 with a 90mm f/2.8 macro and Canon 20D with a 100mm f/2.8 macro lens) and a single 600 ns, 6 J pulse from a spark flash (Palflash 501, Pulse Photonics Ltd.). The flash was triggered after a preprogrammed delay interval initiated by the drop cutting a laser sheet focused onto a photodiode. The triggering event was reproducible to within ± 5 μs. By varying the delay time, the evolution of the impact was recreated from a composite of still images. Examples of typical bottom and side images are shown in Fig 3.3 & 3.4. The virtue of this technique is that it produces much higher spatial and temporal resolution than can be achieved with existing high speed video cameras. The speed of the drop at impact was measured with the high speed video camera.

Our measurements of the crown splash were performed with a 5 centistokes ($\rho = 0.918$ g/cm^3, $\gamma = 19.7$ dynes/cm) or 10 centistokes ($\rho = 0.935$ g/cm^3, $\gamma = 20.6$ dynes/cm) silicone oil purchased from Clearco. Our experiments were performed for the parameters listed in Table 3.1.

For each parameter set we took data at least every 100 μs after the rim emerges from beneath the drop, prior to which the rim is not visible. For parameter set number 1 ($Re = 1060$, $We = 760$, $h = 0.2$) we collected much more data than in other parameter sets in order to reduce fluctuations.

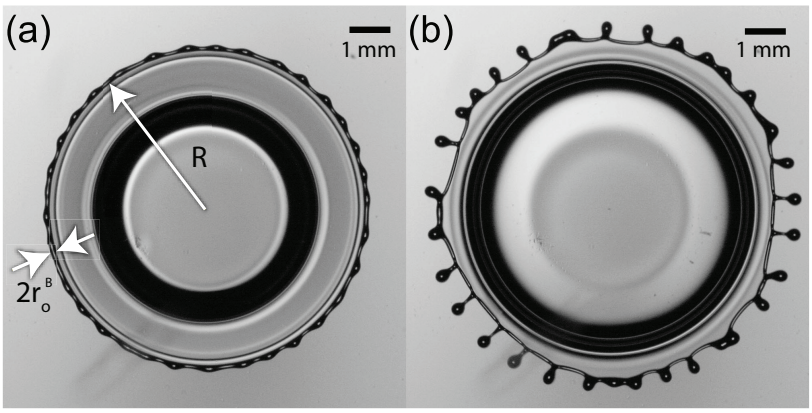

Figure 3.3: Crown splash ($Re = 894, We = 722,$ & $h = 0.1$) from below at $t = 1.85$ ms and $t = 3.15$ ms after impact showing the one-to-one correspondence between instability wavelength and the number of droplets. The arrows define rim radius as seen from below r_o^B and rim's radial distance from the impact center R.

Figure 3.4: *Left:* Images illustrating the crown sheet at 250 and 2100 μs after impact. *Right:* Cartoon of sheet cross-section. At early times, the leading edge of the sheet is almost horizontal. The shape changes as the rim retracts relative to the fluid (though still moving away from the center in the laboratory frame) and entrains the fluid in the sheet. Eventually the entire flat portion of the sheet is entrained in the rim. The kink in the late time sheet is a wave generated when the rim reaches the vertical section of the sheet. Scale bar equals 2 mm.

Set	We	Re	h	Liquid	Speed (cm/s)	Radius (cm)	Layer depth (μm)
1	760	1060	0.20	5 cSt	308	0.172	350
2	1015	1266	0.20	5 cSt	344	0.184	360
3	813	1133	0.10	5 cSt	308	0.184	184
4	1043	642	0.20	10 cSt	349	0.184	368
5	607	979	0.19	5 cSt	266	0.184	350
6	824	1141	0.15	5 cSt	310	0.184	275

Table 3.1: Parameters for experiments.

3.3 Experimental Results

3.3.1 Splash morphologies

By observing splashes for a range of Weber and Reynolds numbers and fixed $h = 0.2$, we classified the morphologies. The parametric dependence of these morphologies are shown in Fig. 4.3. Crown splashes appear only in the regime labeled *Crown Droplets*. A regular crown is also observed in the parameter range below this regime, but these crowns do not form secondary droplets because the growth of the corrugation pattern is slower and thus the sheet retraction occurs before droplets can pinch-off. Outside of this domain, splashes are more irregular and complicated (*Deegan et al.* [2008]) as shown by the examples in Fig 3.6.

3.3.2 Crown splashes

From our bottom-view images we extract the corrugation of the outer edge of the splash to within ± 6 μm. A selection of these data are shown in Fig 3.7. For each parameter set, we capture this corrugation every 100 μs and compute the power spectrum of these data. From the spectra, we extracted the peak wavelength (i.e. the most energetic mode) by a fitting the peak to a Gaussian. For parameter set number 1, we capture the edge profile with much greater time resolution (up to every 10 μs during the first 700 μs) and in addition repeated the measurement at 500 μs intervals ten times. From the latter data, we computed the spectrum for each image,

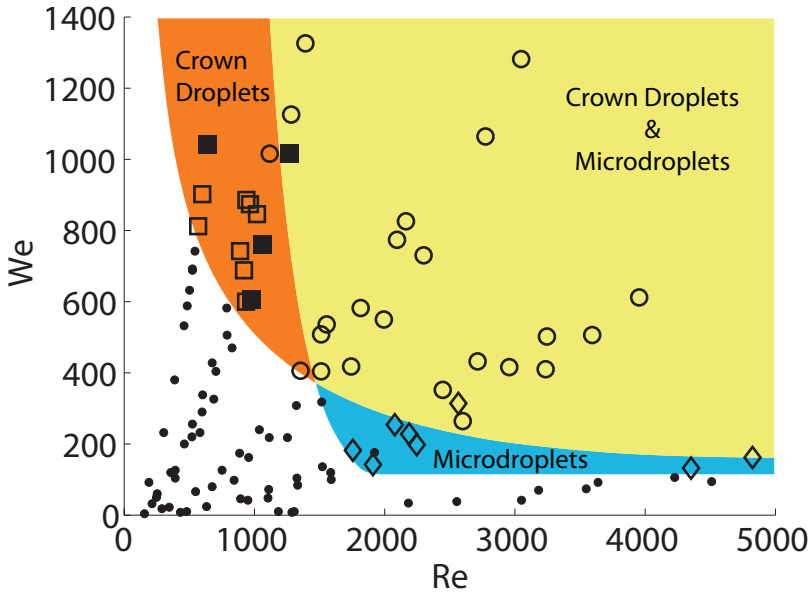

Figure 3.5: Qualitative character of impact for $h = 0.2$. No splash (black small circles), crown droplets with (open circles) and without (squares) microdroplets, and microdroplets without crown droplets (diamonds). The filled squares indicates the parameter set for all experiments at $h = 0.2$ reported here. Spatially periodic crown splashes form exclusively in the Crown droplets regime.

and averaged these results to arrive at the spectra shown in Fig 3.8. The peaks of these spectra, obtained by fitting the upper parts of the peaks to a Gaussian, are plotted in Fig 3.12. The data from the inner edge yields the same spectra but with a reduced amplitude due to the fact that the rim is angled away from the vertical and we only observe its projection on to the horizontal plane.

As shown in Fig 3.8, the peak wavelength shifts to larger values for later times, corresponding to a coarsening of the corrugation. Furthermore, the corrugation does not grow evenly at all points on the rim, but rather nucleates at several locations. These domains grow and merge, consistent with the growth of the unstable modes from random noise. At later times each corrugation sharpens and begins to form a droplet, as demonstrated by the example in Fig 3.3. The number of corrugations – and hence the number of proto-droplets – is set by the ratio of the rim circumference to the peak wavelength. The actual number of emitted droplets is smaller because

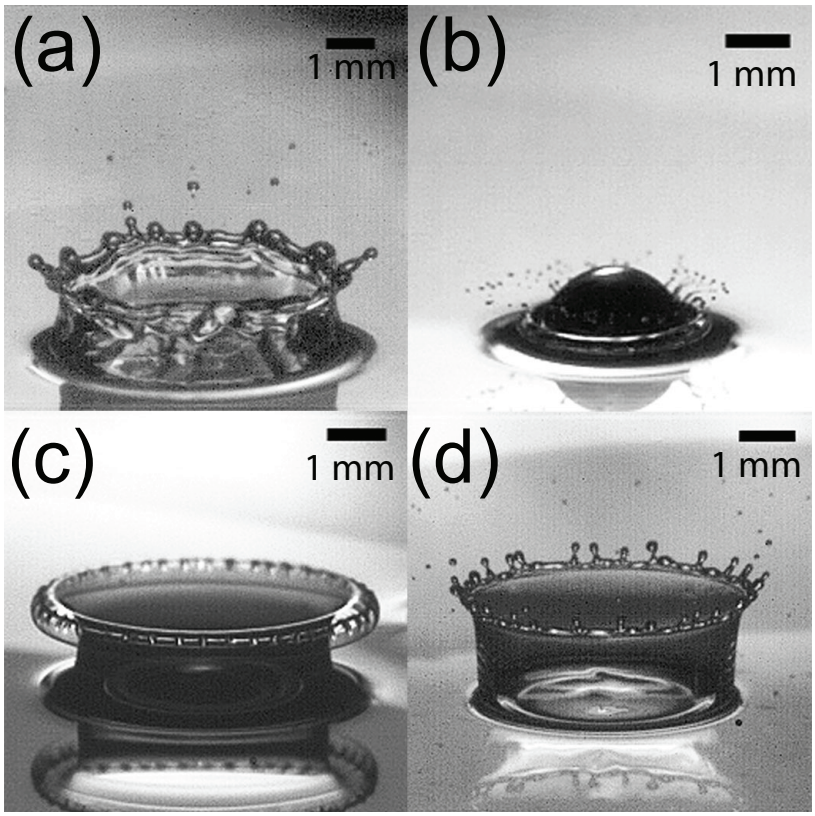

Figure 3.6: Morphologies of splashes outside of the crown splash regime: (a) water ($Re = 6044$, $We = 254$, $h = 0.2$) produces a highly irregular crown sheet and splash (b) glycerol/water mixture ($Re = 2566$, $We = 314$, $h = 0.2$) produces droplets immediately upon impact, long before the crown sheet forms, (c) silicon oil ($Re = 1392$, $We = 1266$, $h = 0.2$) produces a trapped torus of air (d) isopropanol for $Re = 1354$, $We = 406$, $h = 0.2$ produces a wavy crown sheet and continuously ejects droplets as the crown grows upward.

of mergers between adjacent incipient droplets. Therefore, the number of secondary droplets is bounded from above by the most unstable wavelength of the instability.

From our bottom-view images, we also extracted the average radius of the rim as seen from below r_o^B, and the horizontal distance of the centerline of the rim from the impact center R. We processed the images to extract the position of the inner and outer edges of the rim. The radii of the inner r_{inner} and outer r_{outer} edge were determined by fitting to a circle, and from these we obtained the rim radius $r_o^B = \frac{1}{2}(r_{outer} - r_{inner})$ and the radial position of the rim $R(t) = \frac{1}{2}(r_{outer} + r_{inner})$. Figure 3.3

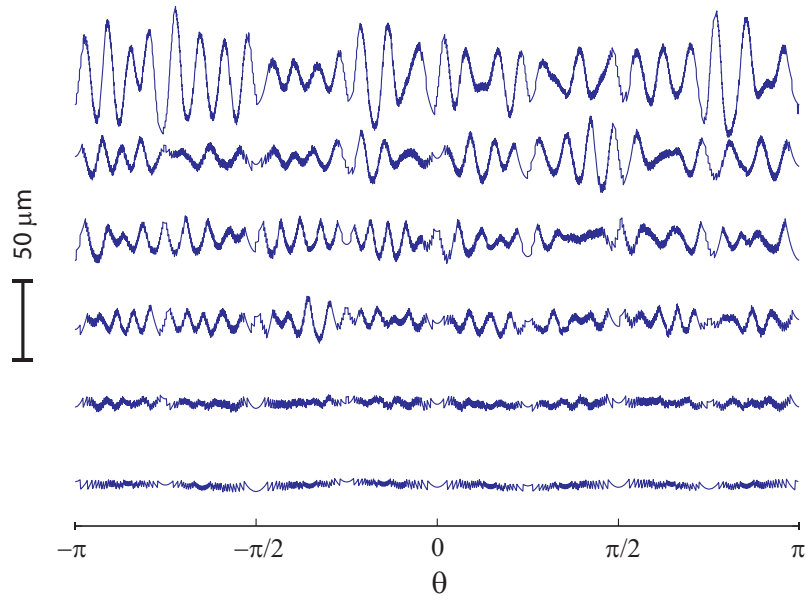

Figure 3.7: Profiles of the outer rim corrugation at successive times (from bottom to top: 115, 365, 605, 1105, 1605, 2085 μs after impact), starting from a smooth profile and growing to a highly corrugated state. Note that the corrugation nucleates at different places and these domains merge at later times. The noise on the early time profiles are digitization artifacts: the camera pixel size is 6.0 μm.

illustrates the physical features corresponding to these parameters, and Fig 3.11 shows their time-dependence for parameter set number 1.

From our side view images, we measured the average radius of the rim as seen from the side r_o^S. Measurements were only possible over a short segment of the rim because of the shallow depth of field of our optical system, and were difficult to obtain due to the small changes in the impact position which would move the rim out of the depth of field. These data are shown by the squares in Fig 3.11. Our side view is to good approximation orthogonal to the bottom view, and hence the effective radius of the rim r_o was taken as the geometric mean of r_o^S and r_o^B. The geometric mean is indicated by the dashed line in Fig 3.11 .

The corrugation of the rim following impact has been attributed by various investigators to the Rayleigh-Plateau instability, the Rayleigh-Taylor instability, the Kelvin-Helmholtz instability, the Ritchmyer-Meshkov instability, and nonlinear am-

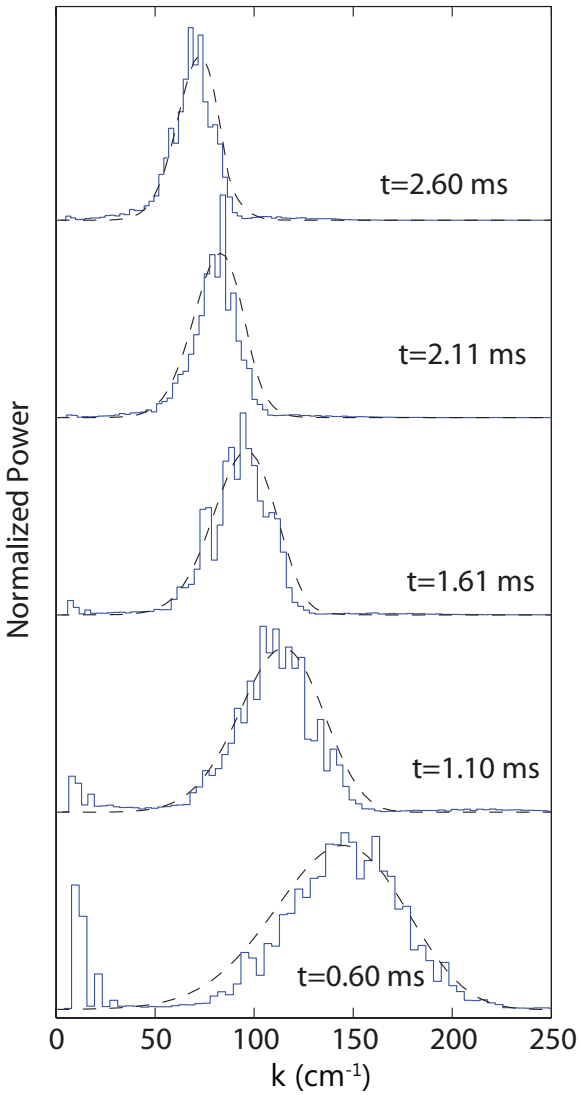

Figure 3.8: Normalized power spectra versus wavenumber for various times after impact for parameter set number 1. The solid curve is the average of multiple experiments and the dashed curve is the prediction from the Rayleigh-Plateau model. The peaks at low wavenumber arise from digitization effects and small non-parallelism of the camera sensor and the impact plane; for example, the largest of these peaks corresponds to the $m = 2$ mode.

plification. Given the vast range of splash morphologies, it may be that each of these effects are dominant in some particular parameter regime. In the following two sections, we compare our measurements in the limited parameter regime labeled *Crown Droplets* – and to some extent the parameter regime at lower Re number – to each of

these mechanisms.

3.4 Rayleigh-Plateau Instability

We compared our measurements to a theoretical calculation based on the physical idea that the rim behaves like a cylinder of fluid subject to surface tension forces. Such a cylinder is unstable to perturbations whose wavelengths are greater than 2π times the radius of the cylinder. This so-called Rayleigh-Plateau instability accounts for the decay of cylindrical jets into droplets (*Rayleigh* [1878]). We first give a physical explanation of this instability before a more rigorous linear stability analysis.

We start with an undisturbed straight liquid cylinder with uniform radius r (Fig 3.9 I), the liquid here is considered inviscid in this qualitative analysis, followed by a formal linear stability analysis with viscosity. The local curvature κ of the surface is defined by the two principle radii r and S, where the stream radius $S = \infty$ (straight cylinder). The curvature is therefore $\kappa = (\frac{1}{r} + \frac{1}{S}) = \frac{1}{r}$. The pressure is balanced on the surface of cylinder:

$$P = \gamma\kappa + P_0 = \gamma\frac{1}{r} + P_0 \tag{3.1}$$

where γ is the surface tension, P is the pressure inside the cylinder, and P_0 is the pressure outside the cylinder. The cylinder is stable since the pressure inside is the same everywhere. When the cylinder is perturbed into a shape as shown in Fig 3.9 II, the pressure inside becomes a function of local geometry. Suppose a is the trough of the perturbation and b the peak, the pressures at a and b are

$$P_a = \gamma\kappa_a + P_0 = \gamma\left(\frac{1}{r_a} - \frac{1}{S_a}\right) + P_0 \tag{3.2a}$$

$$P_b = \gamma\kappa_b + P_0 = \gamma\left(\frac{1}{r_b} + \frac{1}{S_b}\right) + P_0 \tag{3.2b}$$

note the negative sign in P_a because two radii at a point to opposite directions. If $P_a > P_b$, the liquid inside the perturbed cylinder continues to flow from a to b and therefore reinforces the perturbation, otherwise it dies down due to back flow of the liquid. Since $r_a < r_b$, the amplitudes of S_a and S_b become important in deciding the growth or decay of the perturbation. For perturbations with short wavelengths, S_a and S_b are small. As a result, $P_a < P_b$ and the perturbation decays. When the wavelength is long, r_a and r_b dominate and cause the perturbation to grow. Therefore the cylinder is unstable to perturbations with long wavelengths.

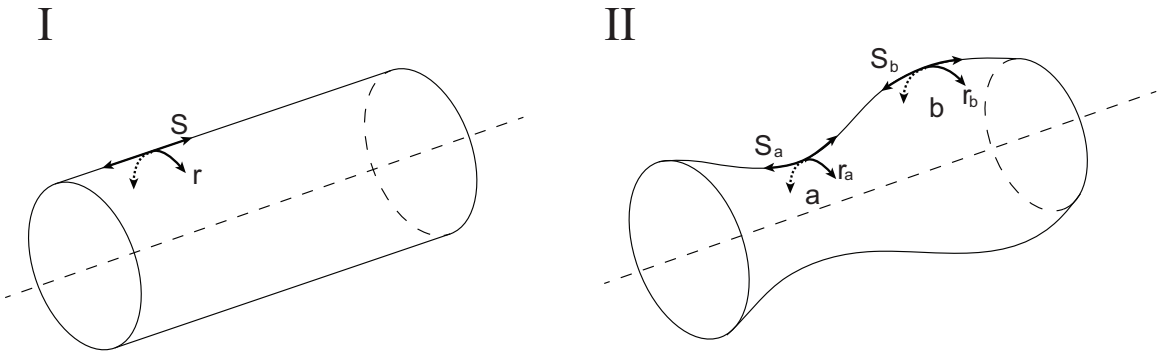

Figure 3.9: I: An undisturbed straight liquid cylinder with uniform radius r and stream radius $S = \infty$, II: A slightly perturbed (exaggerated drawing) liquid cylinder with r and S dependent on local geometry.

If the jet is subject to a broad spectrum of initial perturbations, the typical drop size is set by the wavelength of the perturbation that has the highest growth rate. A characteristic feature of the instability is that this "Rayleigh" mode is a multiple of the radius of the cylinder. In our calculation, we assume that the attachment of the sheet to the rim is negligible. We also treat the cylinder as straight, which is a good approximation if, as in our experiments, the unperturbed rim radius $r_o(t)$ is much smaller than the rim's radial distance from the impact center $R(t)$.

To perform a linear stability analysis, the local rim radius $r(\theta, t)$ is written as

$$r(\theta, t) = r_o(t) + \epsilon(\theta, t) \tag{3.3}$$

where θ is the angle as seen from the center, and ϵ is a small perturbation to the mean radius. The overwhelming majority of past studies focused on the growth of a single mode. Instead, we consider a spectrum of modes in order to characterize the randomness of the perturbations growing on the rim. Thus as an initial perturbation we take the spectral decomposition

$$\epsilon(\theta, 0) = \sum_{m=-N}^{N} a_m e^{im\theta} \tag{3.4}$$

In our model, the initial amplitude of each mode a_m is set equal to the same constant a_0 for all values of m. This is equivalent to assuming that the initial spectrum is flat. We start from the classical result for the growth rate of perturbations on a cylinder of constant radius with no flow inside the cylinder; the boundary conditions include stresses due to the viscosity (*Chandrasekhar* [1981] p.540).

The growth rate σ_m of the mth mode is determined implicitly by

$$2x^2(x^2+y^2)\frac{I_1'(x)}{I_o(x)}\left[1-\frac{2xy}{x^2+y^2}\frac{I_1(x)}{I_1(y)}\frac{I_1'(y)}{I_1'(x)}\right]-x^4+y^4=\frac{\gamma r_o}{\rho\nu^2}\frac{xI_1(x)}{I_o(x)}(1-x^2) \tag{3.5}$$

Here $x = k_m r_o$, $k_m = m/R$ is the wave number of the mth mode, $y^2 = x^2 + \sigma_m r_o^2/\nu$, and I_n are modified Bessel functions of the first kind (*Chandrasekhar* [1981] p. 541).

The topology of the rim is different from that in the classic case of a straight cylinder. The rim in our problem resembles the shape of a torus with a main curvature $1/R(t)$, which is essentially zero in a straight cylinder. Moreover, the rim is attached to a liquid sheet. The difference in topology necessitates several modifications to the analysis of a straight cylinder. First, the amplitude must satisfy $\epsilon(\theta, t) = \epsilon(\theta + 2\pi, t)$, which means there can only be an integer number m of wavelengths on the rim. Moreover, the minimum number of $m = 1$ determines that the longest wavelength that can exist on the rim is $2\pi R(t)$, whereas in the straight cylinder case there is no

such constraint. Second, the torus expands radially and the rim radius must satisfy the conservation of volume. Third, as the rim retracts relative to the attached liquid sheet, its radius increases due to the influx of liquid.

As explained in *Eggers and Villermaux* [2008], we expand on the classic result to include (a) the growth of the rim as it entrains the sheet and (b) the stretching of the rim as the sheet expands. According to equation (106) of *Eggers and Villermaux* [2008], the time evolution of the perturbation in the presence of (a) and (b) is given by

$$\frac{d\ln\epsilon(\theta,t)}{dt} = -\frac{s}{2} + \sigma_m \tag{3.6}$$

where s is the stretch rate due to the expansion of the rim. In other words, longitudinal stretching due to the main curvature of rim $1/R(t)$ always *decreases* the amplitude of the perturbation (*Eggers and Villermaux* [2008]), since it causes fluid elements to contract in the radial direction. The growth rate σ_m is calculated from the classical theory with no stretching or flow into the cylinder (i.e. Eq. 3.5). This approximation is justified by the fact that the base state changes according to a linear law (see Fig 3.11), while the growth of perturbations is exponential, and thus faster. Indeed, while the rim radius changes by a factor of four between 0.5 ms and 2.5 ms (see Fig 3.11), the amplitude of the perturbation changes by more than a decade in the same time span (see Fig 3.10).

Since the stretch rate is $s = \dot{R}/R$, (3.6) can be integrated in time to give

$$\ln\frac{\epsilon(\theta,t)}{\epsilon(\theta,0)} = -\frac{1}{2}\ln\frac{R(t)}{R(0)} + \int_0^t dt'\sigma_m \tag{3.7}$$

Using the initial perturbation (3.4), we then obtain

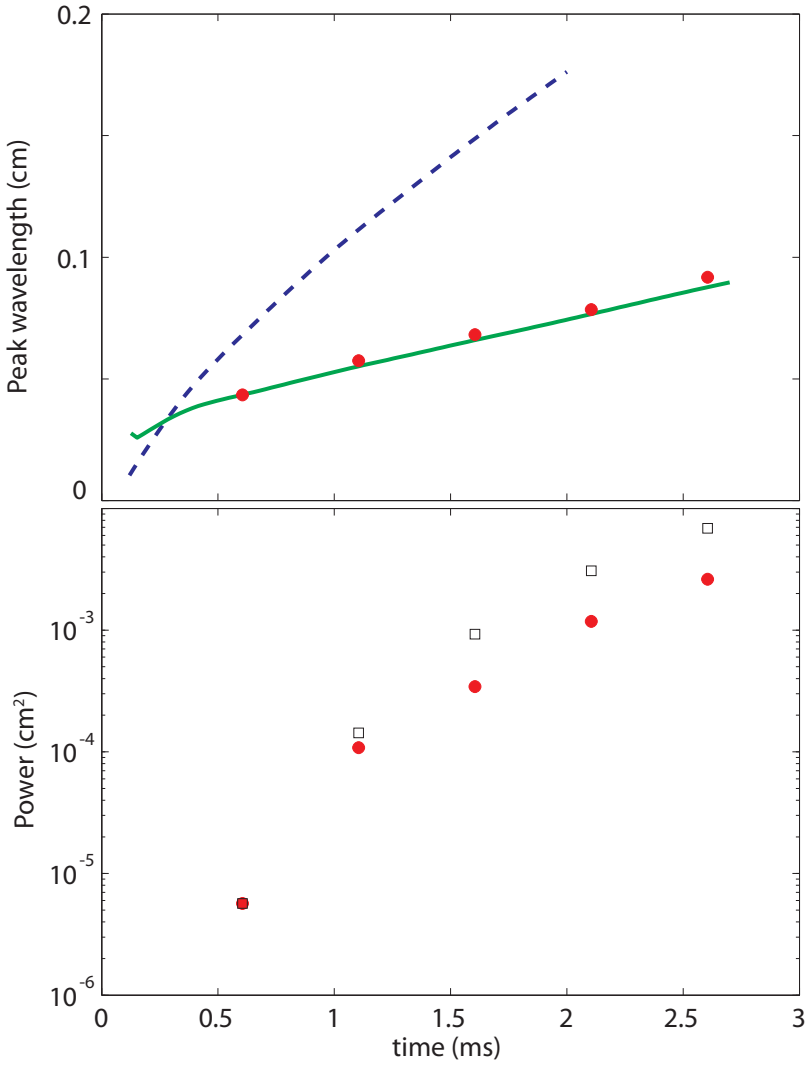

Figure 3.10: Peak wavelength (*top*) and power (*bottom*) versus time: measured (circles) and the predicted values from the Rayleigh-Plateau (solid line,squares) and the Rayleigh-Taylor (dashed line) models for parameter set number 1.

$$r(\theta,t) = r_o + \sqrt{\frac{R(0)}{R(t)}} \sum_{m=-N}^{N} a_m \exp\left[im\theta + \int_0^t dt' \; \sigma_m(k_m = m/R(t), r_o(t)) \right] \qquad (3.8)$$

The spectra obtained from our calculation are compared in Fig 3.8 to those obtained from our most precise experiments. We find excellent agreement in both the position and width of the central peak. Note that the peak position moves to lower

wave numbers as time goes on, since the original perturbation is stretched out as $R(t)$ increases and $r_o(t)$ swells. The peak width decreases in time as the most unstable wave number "Rayleigh mode" is amplified more strongly than the wave numbers surrounding it, and thus dominates the spectrum more and more. The theoretical peak wavenumber is obtained by fitting the calculated spectra with a Gaussian. The peak wavenumber at any given instant t, defined as the mode with the most power, is determined by not only the instantaneously most rapidly growing mode but also by the history of the other modes. Thus the peak wavelength is given by the maximum of $\exp\left\{\int_0^t dt'\ \sigma_m(t')\right\}$. A comparison of these data with experiments is shown in Fig 3.12. The calculation reproduces the measured wavelength to within $\pm 10\%$ for all our experiments and to with $\pm 5\%$ for our most precise experiments at $Re = 1060$, $We = 760$, and $h = 0.2$. It bears emphasizing that the calculation of the peak position and width depends only on the experimental determined variables $r_o(t)$ and $R(t)$, i.e. there are no adjustable parameters.

Our results also account for irregularities in the pattern. Under the action of the Rayleigh-Plateau instability, perturbations away from the most unstable wavelength are amplified as well, albeit at a smaller rate. As shown in Fig 3.8, the width of the spectrum evolved by our equations from initial white noise spectrum is equivalent to that of our data. Thus the irregularity is governed by the width of the central peak of the spectrum, a phenomenon which to our knowledge has never been considered quantitatively for the Rayleigh-Plateau instability (*Eggers and Villermaux* [2008]). Instead, typical measurements of linear instability impose a wavelength from the outside so as to produce a regular pattern, and irregularity is often attributed to nonlinear effects (*Kadanoff* [2000]).

The theoretical peak power was obtained by fitting the calculated power spectra to a Gaussian. The overall scale of these data is determined by the initial amplitude a_0. This parameter was chosen such that theory and experiment agree at $t = 0.6$ ms.

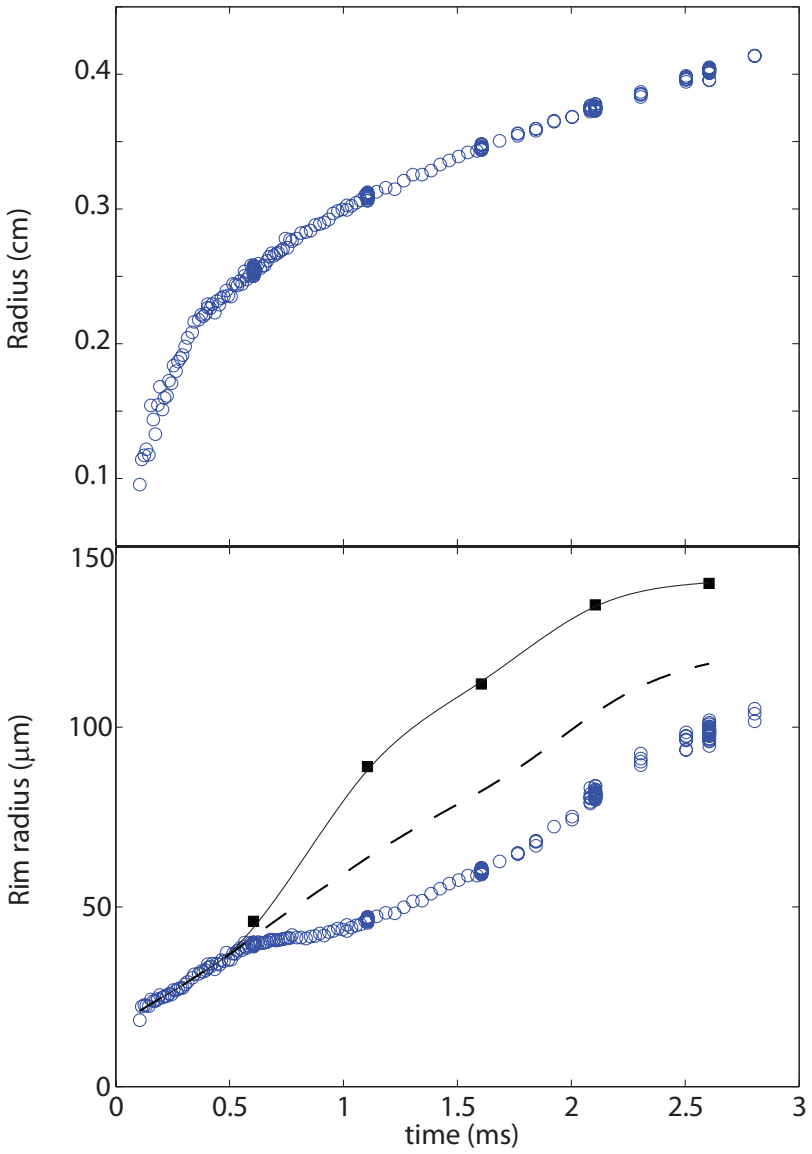

Figure 3.11: Horizontal distance of the rim from the impact center (top) and radius of the rim (bottom) measured from below (circles) and from side (squares) versus time for parameter set number 1. The solid line is a cubic spline of the side data and the dashed line is the geometric mean of the rim radius r_o.

These data are compared to experiments in Fig 3.10. The agreement between the theoretical and measured maximum power is fair, showing a systematic overestimate of the actual growth rate. We believe the deviations arise from both experimental and modeling issues. On the experimental side, our measurements of the amplitude from below undervalue the actual amplitude because we measure its projection on the

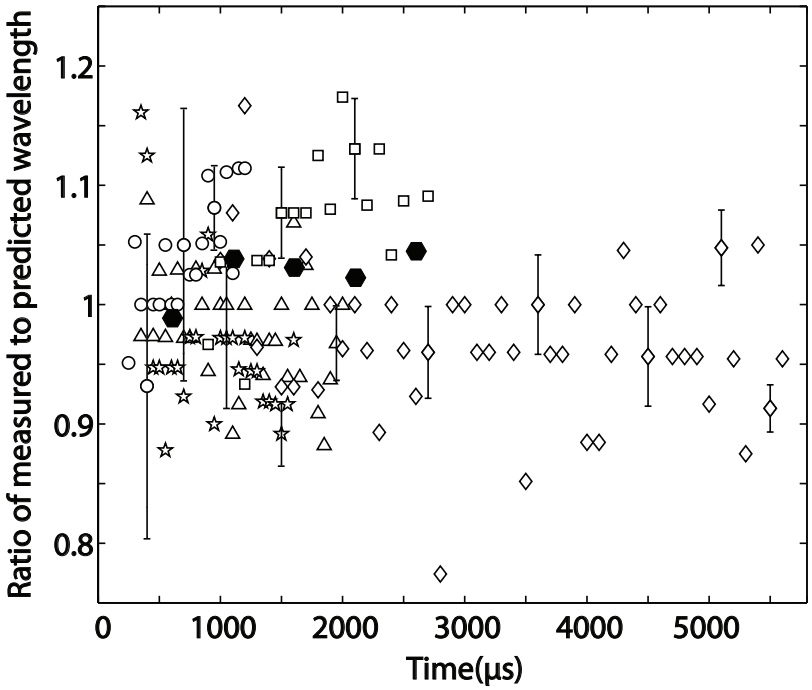

Figure 3.12: Ratio of measured to theoretically expected peak wavelength versus time for the Rayleigh-Plateau model for all experiments: number 1 (hexagons), number 2 (circles), number 3 (stars), number 4 (diamonds), number 5 (squares), number 6 (triangles). Note that the most accurate data is for parameter set number 1.

horizontal plane. On the theoretical side, the assumption in our model that the rim is cylindrical and the unstable mode is varicose may contribute to the disagreement. First, even if the sheet is thin compared to the rim radius, the attachment constrains the evolution of the rim and the reduction of surface energy due to corrugation is not as great as it would be for an unconstrained cylinder. A model calculation in which the curve along which the sheet attaches to the rim is kept uncorrugated (i.e. straight), as observed experimentally, shows that the growth rate decreases. Second, the gradual transition from rim to sheet will slow the growth of the instability. For example, in the extreme case in which the rim is simply a semicircular end of the sheet, there no surface energy to be gained from a local reduction of the rim radius, and thus no instability at all.

3.5 Other Mechanisms

3.5.1 Rayleigh-Taylor Instability

Mechanisms based on the Rayleigh-Taylor instability posit that the generation of secondary droplets arises from the deceleration of the sheet. *Krechetnikov and Homsy* [2009] have argued for this mechanism based on their experiments conducted with milk. Here we show that the Rayleigh-Taylor mechanism predicts wavelengths significantly greater than those observed experimentally. This prediction is based on direct measurements of the acceleration of the rim.

The driving force for the Rayleigh-Taylor instability comes from the deceleration of a fluid surface relative to a less dense external medium, in our case air (whose density can be neglected). It is opposed by surface tension, which favors a flat interface. As a result, the characteristic length scale governing this instability is the effective "capillary length"

$$\ell_a = \sqrt{\frac{\gamma}{\rho a}} \tag{3.9}$$

based on the acceleration a. If ℓ_a is greater than the rim radius r_0, inertial effects are small at the length scales relevant to our study.

We compute the Bond number $\mathrm{Bo}^{-1} = \ell_a^2/r_o^2$ using the acceleration derived by fitting the vertical and horizontal components of position and differentiating the result twice with respect to time. The acceleration and the Bond number are plotted in Fig 3.13. These data show that over the time interval for which we observe growth of perturbations along the rim, ℓ_a is indeed far greater than r_0, confirming that the effect of acceleration is unimportant.

The same conclusion can also be drawn directly from the dispersion relation for the Rayleigh-Taylor instability of a flat interface, for which the growth rate σ_m is defined implicitly by *Chandrasekhar* [1981]:

$$\sigma_m^2 = ak\left[1 - \frac{k^2\gamma}{a\rho}\right] - 4k^2\nu\left(\sigma_m + k\nu\left[\sqrt{k^2 + \sigma_m/\nu} - k\right]\right) \tag{3.10}$$

The cutoff wavenumber, above which no amplification takes place, is $1/\ell_a$. The most amplified wavenumber is slightly smaller (corresponding to a longer wavelength), but its precise value depends on the viscosity. Using the acceleration shown in Fig 3.13, the peak wavelength as predicted by (3.10) is plotted in Fig 3.10. At $t \approx 250$ μs the peak wavelengths coincide, but thereafter the Rayleigh-Taylor prediction is in increasing disagreement with the experimental results, consistent with our expectations based on the Bond number.

The rim of the sheet is curved, not flat, as assumed in the derivation of (3.10). However, as argued by *Krechetnikov* [2009], this only weakens the Rayleigh-Taylor instability, and shifts the range of unstable wavenumbers to even smaller values, or equivalently to higher wavelengths. In other words, the dashed line shown in Fig 3.10 is only a *lower bound* for the true peak wavelength of the Rayleigh-Taylor instability. The physical reason is that if the heavy fluid is bounded by a *convex* interface, the mass of fluid being accelerated is less than that for a flat interface. Since the Rayleigh-Taylor instability is inertia-driven, it becomes less effective. To make up for the loss of mass, the wavelength in the direction along the rim has to be even greater than expected on the basis of (3.10).

Even more recently, the same point has been expanded upon in *Krechetnikov* [2010], by performing a linear stability calculation about a fluid cylinder of circular cross section, which is accelerated in a direction normal to its axis. It is claimed that the interplay between the Rayleigh-Plateau and Rayleigh-Taylor instabilities leads to a change in the dispersion relation. The problem with the calculation of *Krechetnikov* [2010] is that a hydrostatic pressure gradient will build up inside the cylinder, which deforms its equilibrium state from a circular cross section to a new deformed base state. The linear stability calculation thus is not performed about the

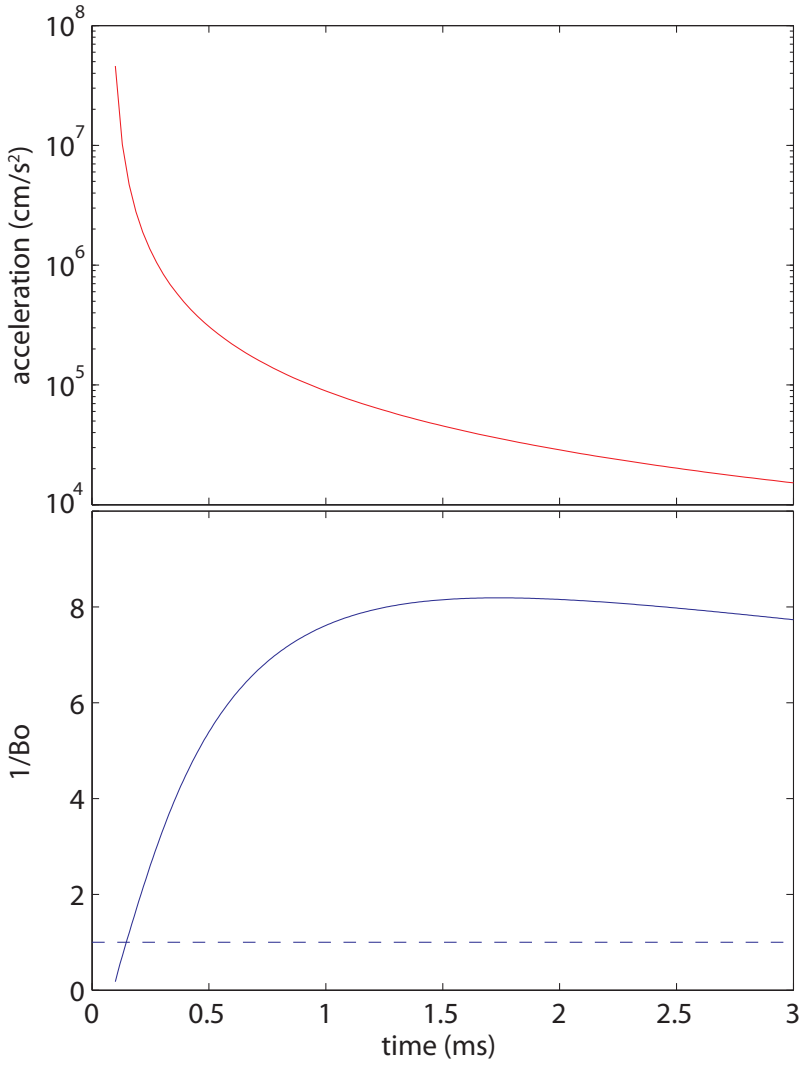

Figure 3.13: Acceleration (top) measured from the trajectory of the rim and inverse Bond number (bottom) versus time. For most of the splash inverse Bond number is large compared to one, indicating the dominant role of capillarity over inertial forces.

true equilibrium state of the system, which leads to inconsistencies. For example, the dispersion relation reported in *Krechetnikov* [2010] shows instability at zero wave number, corresponding to an exponential time dependence of the base state. But as argued above, the fluid cylinder will merely relax to a new equilibrium state when accelerated. We hasten to add, though, that none of these effects are of importance for the present experiments, since the Bond number is small.

3.5.2 Richtmyer-Meshkov Instability

Gueyffier and Zaleski [1998] present simulations in which the length of fingers on the rim grow linear in time. They interpret this result as evidence for a Richtmyer-Meshkov instability triggered by the impulsive impact of the drop on the substrate. Our experiment addresses a much earlier regime, during which the amplitude of perturbations is much smaller than the width of the rim. We find exponential growth for this initial regime, whereas a Richtmyer-Meshkov instability is expected to grow linearly in time. *Krechetnikov and Homsy* [2009] also argue for the Richtmyer-Meshkov instability, based on the experimental observation that the instability occurs in the very early stages of impact, but their experiments were conducted with a non-Newtonian fluid and for $Re \simeq 3000$, $We \simeq 1000$ which, if the fluid was Newtonian, would correspond to the highly irregular splashes we observe in the crown droplet/microdroplet regime.

3.5.3 Nonlinear Instabilities

Yarin and Weiss [1995] proposed a nonlinear amplification mechanism governed by the eikonal equation. This mechanism does not select a particular wavelength but rather sharpens pre-existing perturbations of finite amplitude. Our measurements of the power spectrum show a clear wavelength and thus are inconsistent with this prediction.

3.6 Discussion & Conclusion

Other investigators reached the same conclusions as ours. *Bremond and Villermaux* [2006] found that the Rayleigh-Plateau instability accounts for the fragmentation of the lamella produced by colliding jets. Our results are also consistent with numerical simulations of *Rieber and Frohn* [1999].

Our results do not agree with those of *Yarin and Weiss* [1995] who found a discrepancy between the expected and measured number of ejected droplets. We suspect that differences in the experimental conditions account for the disagreement as their experiments were conducted at a high repetition rate (up to 15000 Hz) in which the liquid layer was highly perturbed by the previous impact. Our results are also at odds with the work of *Fullana and Zaleski* [1999], who used numerical simulations as well as theoretical arguments very similar to ours to conclude that the Rayleigh Plateau instability does not produce sufficient growth to lead to the breakup of the rim. However, no justification was given for their choice of parameter values. In addition, the total length of the sheet simulated by *Fullana and Zaleski* [1999] was only 40 times the thickness of the sheet, and thus permitted to follow the rim evolution only over a limited period of time. Our calculation, by contrast, is based on parameter values obtained directly from experiment, and leads to order one perturbations of the rim over the time the sheet retracts. Thus Fullana and Zaleski's conclusions are invalidated for the experimental parameter regime studied by us.

In conclusion, we study the crown splash regime of the impact of a drop onto a thin film. This permits us to follow the growth of the symmetry-breaking instabilities from very small values through significant perturbations of the rim, leading to the formation of droplets. For a wide range of parameters in this regime, we show (i) that there is a well-defined wavelength selection process, (ii) that the amplification of the selected modes is consistent with a linear instability, and (iii) that the maximum number of secondary droplets is determined by the most unstable wavelength. Our measurements of the most unstable wavelength are in excellent agreement with a model based on the Rayleigh-Plateau instability. Hence, the number of incipient secondary droplets is proportional to the circumference of the splash sheet divided by the most unstable wavelength (and therefore proportional to the radius of the rim), and the irregularity of the crown is set by amplification of random noise by the

spectrum of growth rates of the Rayleigh-Plateau instability.

CHAPTER IV

Parametric studies on liquid drop impacts onto a deep pool

4.1 Introduction

One of our goals is to dispel the ambiguity that exists in the literature concerning the identity of the ejecta sheet versus the lamella. The ejecta sheet predicted by *Weiss and Yarin* [1999] reattached to the surrounding fluid or pinched-off into a torus soon after forming. The fate of the ejecta sheet in *Thoroddsen* [2002] is not explicitly stated, except in those cases where it was shown to disintegrate. The boundary integral method calculations of *Davidson* [2002] show no pinch-off but multiple possible reconnection events; again, its ultimate fate is not stated. Whereas in the latter works the ejecta sheet is transitory, the ejecta sheet of *Howison et al.* [2005] persists for all time.

Here we report our experimental observations of the ejecta sheet's dynamics following normal impact of a spherical drop with a layer of the same liquid. Our visualizations were obtained using high speed photography with visible light and X-rays. The X-ray technique allows us to see features that in visible light would be obscured by refraction and reflections from free surfaces. We find that the ejecta sheet is always present for Weber numbers above a certain threshold. At low Reynolds numbers the

	Fluid	Viscosity (centipoise)	Density (g/cm^3)	Surface tension (dyne/cm)
SO1	silicone oil	0.49	0.759	15.7
SO2	silicone oil	0.82	0.816	17.2
SO3	silicone oil	1.3	0.851	17.6
SO4	silicone oil	1.8	0.871	18.6
SO5	silicone oil	2.7	0.899	18.4

Table 4.1: Physical properties of experimental fluids.

lamella and ejecta sheet form a single contiguous jet, and thus the ejecta sheet persists indefinitely even though at later times it is subsumed into the growing blob on the leading edge of the jet (*Keller et al.* [1995]). At high Reynolds and Weber number the ejecta sheet disintegrates. We measured the emergence time, position, and speed of the ejecta sheet, and find that these depend strongly on the impact speed and weakly on the viscosity. We show that scaling these quantities with viscosity collapses the data onto master curves that depends only on the impact speed. Lastly, we show that the size of secondary droplets is not necessarily a good indicator of whether the droplets are from the ejecta sheet or the lamella.

4.2 Experimental System

We conducted experiments to observe the impact of a drop (diameter $D \approx 2$ mm) onto a deep pool of the same fluid (depth > 10 cm) at speeds U=1 - 5 m/s. Each drop was formed on the tip of an electrically grounded sewing needle fed by a 30 gauge hypodermic needle connected to a reservoir. The sharp conical tip of the sewing needle minimized surface oscillations and lateral deflections, which greatly reduced variations of the impact location and yielded reproducible drop sizes. The oscillations of the drop after detaching from the needle decayed long before impact, and the small size of the drops ensured that the flattening caused by air drag resulted in a less than 3% difference between the major and minor axis of the drop. The experimental fluids

were a series of silicone oils (Clearco Products) with different viscosities; their physical properties are listed in Table 6.1. Drops were produced at a rate sufficiently slow to allow the waves on the substrate fluid from the preceding drop impact to fully decay.

Our visible light measurements were obtained from a high speed video camera (Phantom 7.3, Vision Research) or a single lens reflex camera (20D, Canon) in combination with a single 600 ns, 6 Joule pulse from a spark flash (Palflash 501, Pulse Photonics) triggered by the interruption of a photogate by the drop (*Zhang et al.* [2010]). Our X-ray measurements were conducted at high-speed imaging facility at the Advanced Photon Source at Argonne National Laboratory using a phase contrast technique (*Fezzaa and Wang* [2008b]). The latter technique produces images, such as those shown in Fig 4.1, in which the gray scale is indicative of absorption by the fluid and the fluid-gas interface parallel to the beam are highlighted by a light or dark halo. The substrate fluid appears black in these images because the X-ray beam traverses the full diameter of the container ($\sim$ 10 cm) and therefore is highly attenuated. The phase contrast technique produces some halo-like artifacts, such as the one indicated in Fig 4.1(b), that are easily distinguished by eye or, if necessary, by simulation (*Fezzaa and Wang* [2008b]).

The impact of a drop with a deep layer of the same fluid is conventionally described by six parameters: the impact velocity U, the drop's diameter D or radius R, the fluid's surface tension σ, density ρ, and dynamic viscosity η, and the acceleration due to gravity g. These parameter reduce to three dimensionless groupings which are commonly chosen to be the Weber number $We = \rho DU^2/\sigma$, the Reynolds number $Re = \rho DU/\eta$, and the Froude number $Fr = U^2/gD$. The acceleration due to gravity is assumed to be negligible on the timescale of a splash and henceforth the dependence on the Froude number is ignored.

We measured the kinematic viscosity of our fluid with a Cannon-Fenske routine viscometer, the density with a Gay-Lussac bottle, and the surface tension with the

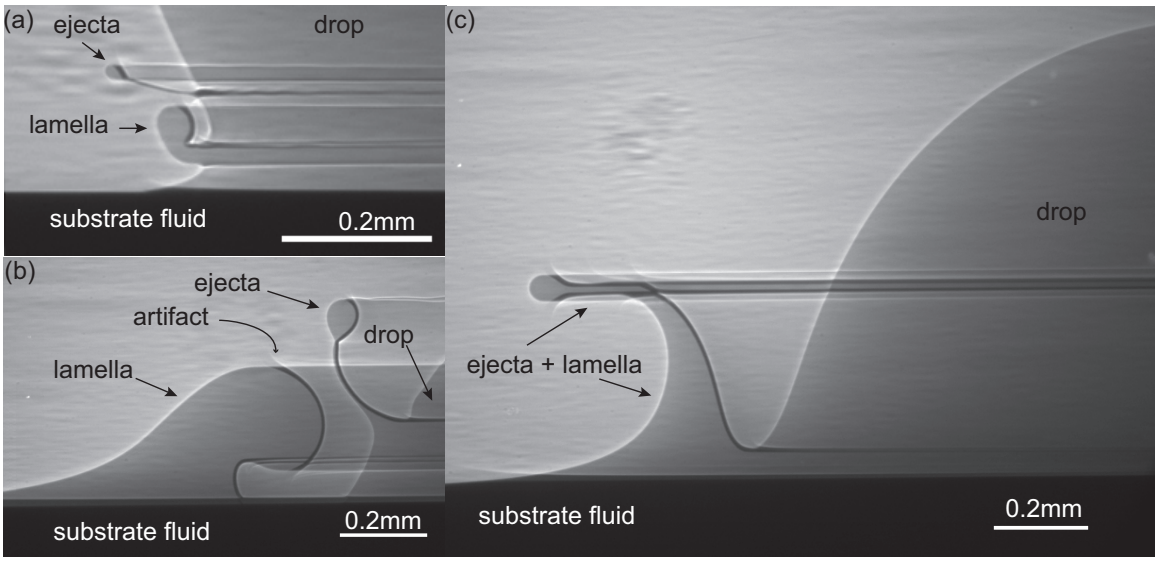

Figure 4.1: X-ray phase contrast images of splash at (a) $We = 396$ & $Re = 5703$ with 0.65 cSt silicone oil, (b) $We = 324$ & $Re = 2191$ with 1.5 cSt silicone oil, and (c) $We = 451$ & $Re = 710$ with 5 cSt silicone oil. (a) & (b) show a thin jet (the ejecta sheet) and a thicker jet (the lamella sheet). (c) shows the ejecta sheet and lamella sheet combined into a single contiguous sheet. Note that the leading edge of all jets are engorged due to Taylor-Culick contraction. The wayward halo departing from the lamella in (b) is an example of an artifact produced by the phase contrast technique.

Wilhelmy plate method.

4.3 Experimental results

4.3.1 Phenomenology of the ejecta sheet

Deegan et al. [2008] proposed a classification of splashes in shallow layers in which they differentiated between *crown droplets* which unambiguously detach from the lamella and *microdroplets* whose origin was not determined but which they speculated were produced by the break-up of the ejecta sheet. *Thoroddsen et al.* [2011] recently showed that the ejecta sheet unambiguously produces microdroplets. We examined the initial moments of impact to further characterize the production of the microdroplets. We found that the behavior at early times, as demonstrated by the examples shown in Fig 4.1, is far more complex than previously thought.

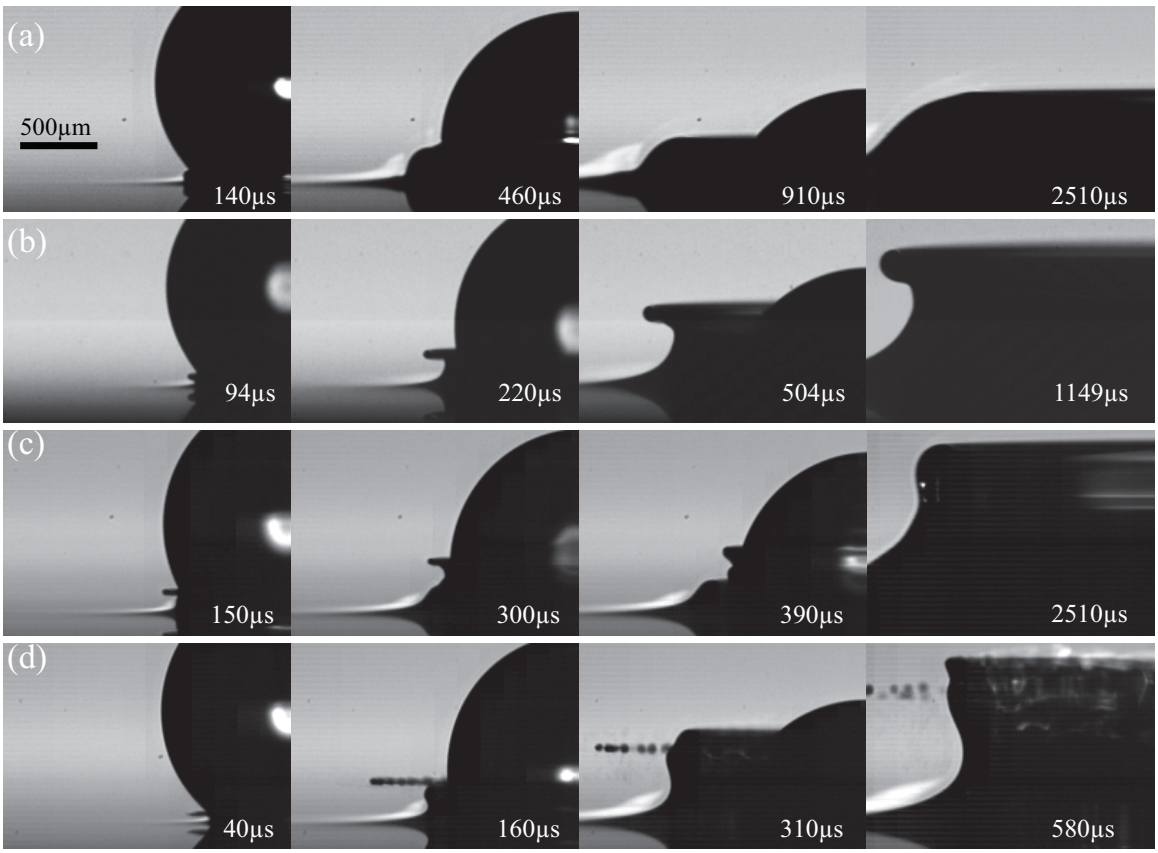

Figure 4.2: Time evolution of jets for (a) $Re = 1330$, $We = 117$; (b) $Re = 1511$, $We = 282$; (c) $Re = 2931$, $We = 256$; (d)$Re = 4975$, $We = 735$. These parameters are plotted in Fig 4.3 with an unfilled circle, square, star and diamond, respectively. The time after impact is given in the lower righthand corner of each image and the scale bar the is given in the first panel of (a). The black corresponds to the fluid. The various white patches are lighting artifacts.

The lamella and ejecta sheets are labeled in Fig 4.1. While Fig 4.1 (a) & (b) show two distinct jets, the panel (c) shows a single jet. Furthermore, this single jet is what we would normally classify as a lamella (*Zhang et al.* [2010]). We examined the evolution of this jet at all accessible times and find no other jet. This raises the question of whether there is a bifurcation in the dynamics at which the ejecta sheet loses or gains integrity.

We observed splashes over a wide range of We and Re and found that these follow one of the four behaviors depicted in Fig 4.2: (a) the drop merges with the substrate

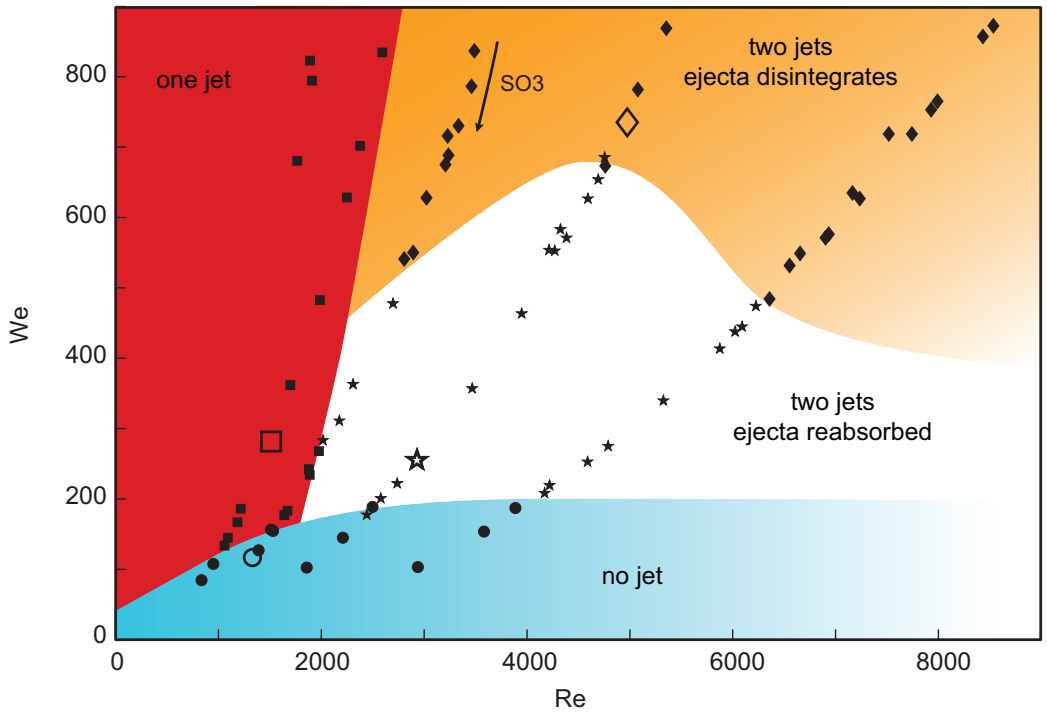

Figure 4.3: Phase diagram as a function of *We* and *Re* indicating number of jets resulting from drop impact. The behavior of each experiment is indicated with a symbol: circles for a non-cresting capillary, squares for a single jet comprised of both the ejecta sheet and lamella sheet, stars for separate ejecta sheet and lamella, and diamonds for separate ejecta sheet and lamella when the ejecta sheet dissociates into secondary droplets. Unfilled symbols correspond to the particular experiments depicted in Fig 4.2.

fluid generating capillary waves as shown by *Yarin and Weiss* [1995]; (b) a single jet forms; (c) a thin jet (the ejecta sheet) emerges within 100 μs after impact followed by a thicker one (the lamella); the ejecta sheet folds into and ultimately merges with the upper part of the drop; (d) like (c) two jets are produced but instead the ejecta sheet disintegrates into microdroplets.

Our experiments are summarized in Fig 4.3. For different impact speeds the experiments for a particular fluid trace out a curves $We = \alpha \mathrm{Re}^2$. The most revealing experiments are those for SO3 (indicated by an arrow in Fig 4.3) which cross from the *two jet* to the *one jet* regime. Experiments with this fluid at moderate and high *We* show two clearly distinct jets. The separation of these jets decreases with *We*.

Just above the transition to *one jet*, the jets remain robust and clearly separate, but are very close to each other; just below the transition, there is only a single jet and furthermore it is shaped as though the ejecta sheet was affixed to the leading edge of the lamella. From these observations we conclude that the ejecta sheet and the lamella merge to form single jet. Thus, the horizontal segment on the leading edge of the jet visible in Fig 4.1(c) is the ejecta sheet riding on the leading edge of the lamella. For all values of *Re* below the transition point the jets remain conjoined.

Thoroddsen et al. [2011] provided a different classification of splashes in a parameters range similar to ours. While our data focuses exclusively on the ejecta sheet dynamics, their categorization focuses on microdroplet production. The two classifications are complementary. For example, their *sling shot* regime falls within our *one jet* regime, and their *irregular broken sheets and spray* regime corresponds closely to our *two jets* regime in which the ejecta sheet disintegrates. In the former case, our experiments reveals that the ejecta sheet forms the leading edge of the lamella whereas their experiments shown how this ejecta sheet breaks up. In the latter case, their experiments reveal the presence of microdroplets whereas our experiments pinpoint their source.

4.3.2 Dynamics of the ejecta sheet

In addition to the morphology, we measured the emergence time, position, and speed of the ejecta sheet using high speed video recording, typically at 50,000 frames per second. Figure 4.4 (a) & (b) show typical data for the jet position versus time after impact. In order to determine the time when the drop first touches the layer (i.e. $t = 0$), we measured the vertical distance between bottom pole of the drop and its refection for several frames prior to impact and extrapolated this value to zero. In all cases we examined, the radial distance of the tip from the center of the impact r grew rapidly and showed strong signs of deceleration, whereas the vertical position

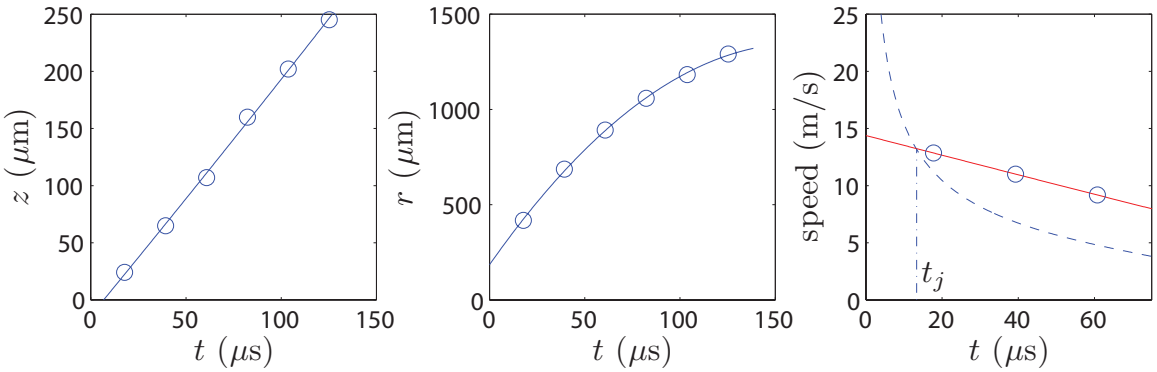

Figure 4.4: Example of the radial r and vertical z position of the ejecta sheet versus time, and the procedure for determining the emergence time t_j. The data for the position of the leading edge plotted versus time after impact (circles) were fit to a parabola (solid line). The speed of the jet was determined by from the derivative of the fit, and plotted in the (c) with a (red) solid line. The speed of the front for the particular impact speed (see Appendix A) is plotted with a (blue) dashed line. The intersection of the front and jet speed was taken as the emergence time.

relative to the layer surface z grew slowly and showed weak signs of acceleration.

We determined the speed of the ejecta sheet from the derivative of a fit to the position versus time data, and compared it to the speed of the front u_m that is required to move the mass of fluid from beneath the drop (see Appendix A). We define the emergence time t_j as the time when these curves intersect, as shown in Fig 4.4(c). In all cases, t_j lies in the time interval between the image pair bracketing the visible emergence of the jet. We took the emergence speed u_j and the radial position r_j of the jet as the value of these at t_j.

Our measurements for t_j, r_j, and u_j are plotted in Fig 4.5 versus impact speed. The data for each liquid is plotted with a different symbol and color as described in the caption. The most prominent trends are t_j strongly decreases with impact speed and weakly increases with viscosity, r_j weakly decreases with impact speed and weakly increases with viscosity and u_j strongly increases with impact speed and weakly decreases with viscosity. The dependence on the impact speed of these quantities is what one would expect qualitatively on the basis of energy conservation. With

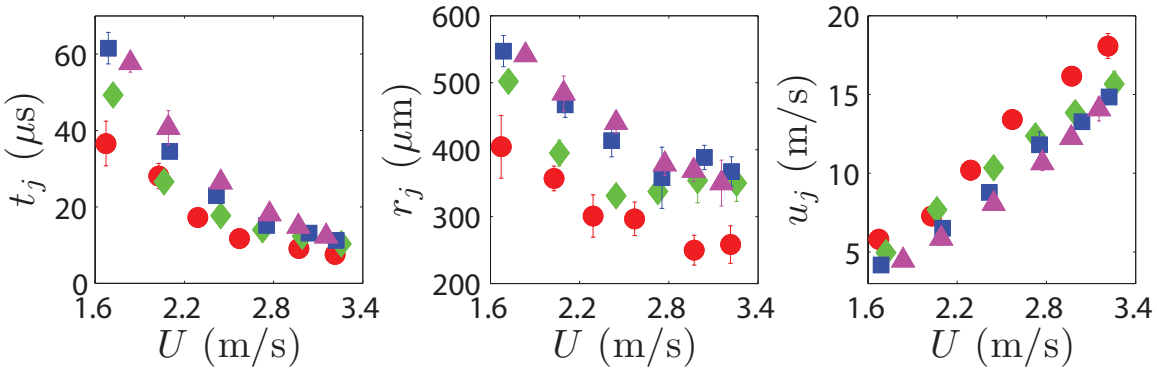

Figure 4.5: The emergence time t_j, radial position r_j, and speed u_j of the ejecta sheet plotted versus impact velocity. Symbols correspond to different fluids: red circles for SO1 (0.49 cP), green diamond for SO2 (0.82 cP), blue square for SO3 (1.3 cP), pink triangles for SO4 (2.7 cP). The error bars represent the variability of the data for a fixed set of parameters which is primarily due to the uncertainty in time of first contact between the drop the layer.

increasing kinetic energy of the drop, the ejecta sheet ought to be more energetic and thus faster, and a faster jet will out run the mass front earlier and closer to the origin. The dependence on the viscosity is also what one would expect qualitatively on the basis of energy conservation and the magnitude of jet Reynolds number $Re_j = u_j\delta/\nu$ where δ is the jet thickness. From measurements $\delta \approx 10$ μm and $Re_j \gtrsim 100$. At these values of Re_j we expect the dissipation to lie between the purely viscous and purely inertial regimes which would account for the weak dependence on viscosity.

Empirically we find that scaling t_j by $\sqrt{\nu}$ collapses all the experiments to a single curve as shown in Fig 4.6(a). Furthermore, that curve is well-represented by a power law in the impact speed with an exponent of -2.6.

From this collapse of the emergence time data it follows that the ejecta sheet speed at emergence will also collapse. By construction $u_j = u_m(t_j)$. For $t \ll R/U$ it follows that $u_m \sim \sqrt{U/t}$, and thus $u_j \sim \nu^{-1/4}U^{1.8}$. The data shown in Fig 4.6(b) verifies this scaling. Interestingly, any reasonable and consistent manner of defining u_j produces the same scaling. For example, we tried (i) defining u_j as the earliest measured velocity of the jet, (ii) t_j as the moment when the vertical position of the

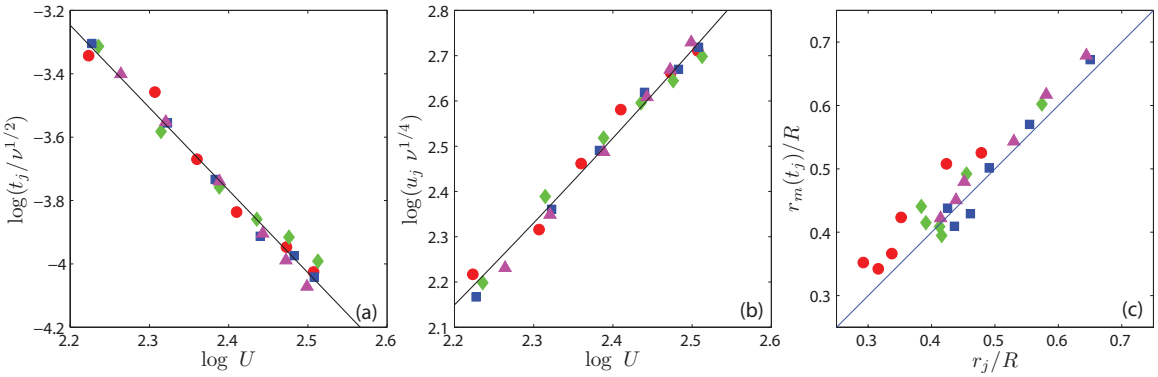

Figure 4.6: (a & b) Scaled emergence time t_j and speed u_j versus impact speed U plotted on a log-log scale. The solid lines are fits to power laws which yield exponents of -2.6 and 1.8, respectively. (c) Mean radius dictated by mass balance versus the emergence position, both scaled by the radius of the drop.

jet is zero (see Fig 4.4) and obtaining u_j by extrapolation, and (iii) choosing $t_j = 0$ and obtaining u_j by extrapolation. In all cases, the scaling of the jet speed is the same, and thus more robust than is apparent from our particular treatment.

Figure 4.6(c) shows the mean radius r_m (see Appendix A) versus the emergence radial position. These data show that the jet emerges closer to the center than the theoretical value of r_m. This is consistent with the inward (i.e. into the fluid) curvature of the meniscus connecting the drop and the fluid layer prior to the emergence of the ejecta sheet. The curvature of the front is expected due to surface tension (*Oguz and Prosperetti* [1989]). Nonetheless, the rearmost segment of the meniscus lags behind the mean radius and we observe that it is from this trailing front that the ejecta sheet emerges.

The primary points of comparison for our results are the inviscid simulation of *Weiss and Yarin* [1999] and *Davidson* [2002], the experiments of *Thoroddsen* [2002], and the volume-of-fluid simulations of *Coppola et al.* [2011]. In our experiments the threshold for the formation of ejecta sheets is a curve in the *Re*-*We* plane, as shown in Fig 4.3. While this curve bends downward at low *Re* indicating a significant effect of viscosity, at higher *Re* the dependence on viscosity weakens. In so far as this trend

can be extrapolated to the inviscid limit, our data indicates that the ejecta sheet threshold plateaus to $We \simeq 180$ which is reasonably close to the values predicted by *Weiss and Yarin* [1999] ($We \simeq 40$) and *Davidson* [2002] ($We \simeq 200$).

Our results for r_j, t_j, and u_j differ in magnitude significantly from *Thoroddsen* [2002] and *Coppola et al.* [2011], but show qualitatively similar trends. We do not expect numeric agreement given the large difference in We between our respective experiments: We=200-800 in our experiments, We=8000 in *Coppola et al.* [2011], and We=2350 in *Thoroddsen* [2002]. Nonetheless, we expected the same scaling behavior. This was not the case either. We find $t_j \sim \sqrt{\nu}/U^{2.6}$, while *Coppola et al.* [2011] find that their data does not follow a (single) power law. We find that $u_j \sim \nu^{-1/4}U^{1.8}$, while *Coppola et al.* [2011] found that $u_j \sim \nu^{-1/2}U^{1.5}$ in agreement with the viscous scaling $u_j \sim \nu^{-1/2}$ found by *Thoroddsen* [2002]. Given that the simulation of *Coppola et al.* [2011] are for the impact of a cylindrical drop, these differences may be due entirely to geometry.

4.3.3 Secondary Droplets

As summarized in Fig 4.3, when $We \gtrsim 500$ the ejecta sheet disintegrates and produces a spray of secondary droplets. These droplets are much smaller (≈ 15 μm) than the typical droplets formed by a crown splash (250 μm, *Zhang et al.* [2010]). The presence of bulb on the leading edge of the ejecta sheet (see Fig 4.1) is reminiscent of the engorgement of the lamella's leading edge that precedes its breakup due to a capillary instability (*Zhang et al.* [2010]). Moreover, for the particular range of We and Re studied in *Zhang et al.* [2010] the ejecta sheet and lamella form a single jet and it is the contraction of the ejecta sheet segment of this jet which forms the toroidal blob of fluid that ultimately breaks up. While these similarities suggest that the ejecta sheet disintegrates via a capillary instability, due to the speed and short life of the ejecta sheet we were unable to explore this possibility.

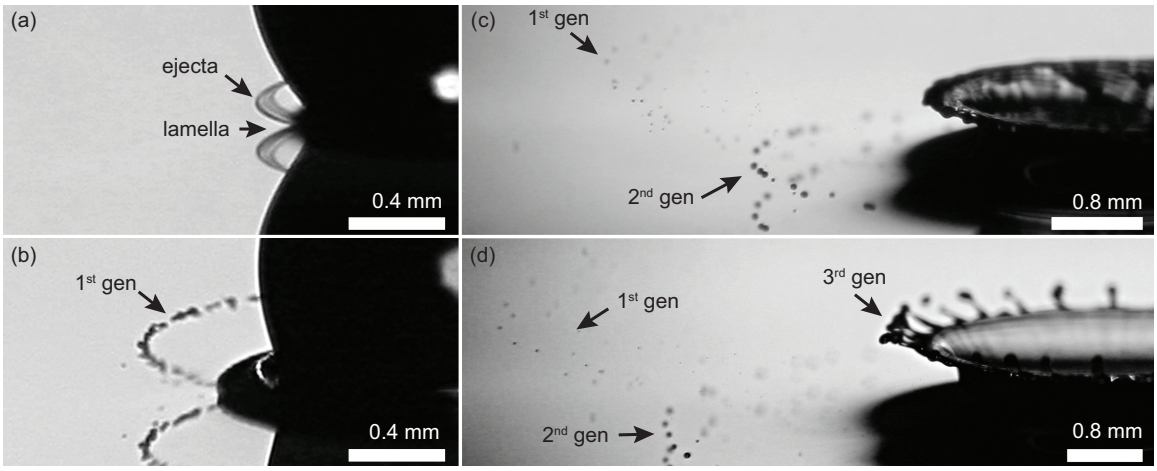

Figure 4.7: Multiple generations of emitted microdroplets from a single impact event for 0.65Cst silicone oil at $We = 798$ & $Re = 8019$ in a reduced pressure environment (0.17 atm) at 60, 100, 500, 700 μs after impact with earliest time at top.

The small size of the secondary droplets produces by the ejecta sheet partially support the speculation by *Deegan et al.* [2008] that the dichotomy in the size distribution of secondary droplets is due to different jets. Their hypothesis was that *microdroplets* could be attributed to the disintegration of ejecta sheet, while *crown droplets* could be attributed to the break-up of the lamella. While this does occur as shown by *Thoroddsen et al.* [2011] and in Fig 4.2(c), more complicated scenarios are also possible. Figure 4.7 shows a single impact event which produces three generations of microdroplets, only one of which is due to the breakup of the ejecta sheet; the other generations come from the lamella in separate breakup events. Interestingly, the clear distinction between generations is obscured at full atmospheric pressure. *Thoroddsen et al.* [2011] observed similar dependencies on the surrounding gas pressure.

4.4 Conclusions

The ejecta sheet and the lamella are not sharply distinguished in the literature. One of the principal results of our study is that it provides definitive evidence (see Fig 4.1) that there are two distinct jets. Following the nomenclature established by

Weiss and Yarin [1999], there is an ejecta sheet, a high speed jet formed almost immediately upon impact (within 100 μs), and a lamella sheet, a slower jet which emerges later (typically 500-1000 μs after impact). Our second principle result is that for low Re the ejecta sheet and lamella form a single continuous structure. Thus, the seeming absence of an ejecta sheet is now revealed as the case where the ejecta sheet becomes the leading edge of a jet comprised of the ejecta sheet and the lamella.

Our measurements of the position, speed, and time of the ejecta sheet when it emerges from the neck show that these quantities scale as power laws in the impact speed and the viscosity. Our results are significantly different from previously reported results at similar Re but higher We. The difference may be indicative of qualitatively different dynamics at higher We or of a strong dependence on the We to which our experiments are insensitive because surface tension was kept constant.

The breakup of the ejecta sheet produces secondary droplets which are much smaller than those typically formed from the lamella. Nonetheless, we observe atypical cases in which the secondary drops from the lamella are almost equal in size to those from the ejecta sheet, and thus size of secondary droplet is not necessarily a good indicator of their origin.

CHAPTER V

Effects of ambient gas pressure on liquid drop impacts

5.1 Introduction

The conventional parametrization neglects the surrounding gas based on the low density ρ_g and dynamic viscosity η_g of the gas relative to those of the liquid; typically $\Sigma = \rho_g/\rho \approx 10^{-3}$ and $\Lambda = \eta_g/\eta \approx 10^{-2}$). This assumption is called into question by the new evidence that in some circumstances the interaction between liquid and gas is crucial. For example, in the case of an impact onto a dry substrate *Xu et al.* [2005] found that a reduction of the gas pressure eliminated the production of secondary droplets. *Thoroddsen et al.* [2011] tested the effects of a partial vacuum on the ejecta sheet, which bent significantly in a more pressurized environment. There have not been systematic studies on drop impacts on a wet substrate with a wide experimental range; I conducted such experiments and reported them in this chapter.

We created drop impacts on a deep pool with a variety of liquids, and the results of an impact are characterized into four regimes in the parameter space of Re and We (*Zhang et al.* [2012a]. We compared drop impacts in two levels of gas pressure: the normal atmosphere and a partial vacuum. The effects of the partial vacuum are found to be regime-dependent.

Fluid	Viscosity (centipoise)	Density (g/cm^3)	Surface tension (dyne/cm)	Σ/Λ in air $\times 10^{-3}$	Σ/Λ in vacuum $\times 10^{-3}$
SO1	0.49	0.759	15.7	1.58/37.7	0.264/37.7
SO2	0.82	0.816	17.2	1.47/22.6	0.245/22.6
SO3	1.3	0.851	17.6	1.41/14.2	0.235/14.2
SO4	1.8	0.871	18.6	1.38/10.3	0.230/10.3
SO5	2.7	0.899	18.4	1.33/6.85	0.223/6.85
SO6	5.2	0.918	19.4	1.31/3.56	0.218/3.56

Table 5.1: Physical properties of experimental fluids and value of Σ, Λ in air (1 atm) and vacuum (0.16 atm)

5.2 Experimental Setup

In our experiments a liquid drop was released from a fixed height into a deep pool of the same liquid. Each drop was formed at the tip of an electrically grounded sewing needle, fed by a hypodermic needle connected to a reservoir. The sharp conical tip of the sewing needle minimized surface oscillations and lateral deflections, which greatly reduced variation of the impact location, and yielded drops of a consistent diameter characteristic to each fluid. Our drops were typically around 2 mm in diameters and showed almost no flattening due to air drag (the percentage difference between the major and minor axis was less than 3%). Impact speeds ranged from 1.1- 3.2 m/s. The interval between successive impacts was kept long compared to the time for waves formed by the prior drop to dissipate.

The drops and underlying liquid pool consists of the same type of silicone oil (Clearco) listed in Table 5.1. I enclosed the experimental system within a vacuum chamber that supported two different levels of pressure: normal (1 atm) and reduced (0.16 atm). The majority of the observations were optically-based, using a high speed video camera (Phantom v11, Vision Research) fitted with a macro lens (Navitar 6000). They were complemented with some X-ray phase contrast images for the benefit of a higher image magnification and easier interpretation. The X-ray images were taken only at normal atmospheric pressure(1 atm); the vacuum environment could not be

established for X-ray imaging due to limitations at the experimental facility.

5.3 Results

5.3.1 Boundary shifts in phase diagram

A typical drop impact event on a deep pool displays behaviors that belong to one of the four regimes in the parameter space of Re and We (*Zhang et al.* [2012a]). Regimes are separated by certain boundaries on the phase diagram; as we change the ambient gas pressure, any change in behavior of the ejecta sheet or lamella will be reflected in the form of boundary shifts between regimes. We plotted the phase diagrams for both pressure levels and superimposed them in Fig 5.1. The results show boundary shifts for all four regimes, a fact that indicates an important role played by the ambient gas pressure.

5.3.2 Formation of ejecta sheet

After the drop hits the surface of the pool, the neck region between the impacting drop and the underlying surface begins to show a bulge at around 20 μs, a very early time compared to the characteristic time $\tau = D/U$ on the order of 1 ms for our experiments. For each type of liquid, there is a critical velocity that sets the boundary between region I and II, below which the bulge remains its shape (Fig 5.2 a), above which the bulge protrudes outward and becomes an ejecta sheet (Fig 5.2 b). Since the transition from the bulge to the ejecta sheet is gradual as the impact velocity increases, we distinguish the former from the latter by comparing two characteristic lengths of the protrusion: a bulge has a longer width (defined by dashed arrow in Fig 5.2) than length (defined by solid arrow in Fig 5.2), while an ejecta sheet has the reversed case (Fig 5.2).

Regime I and II represent the absence and the emergence of the ejecta sheet,

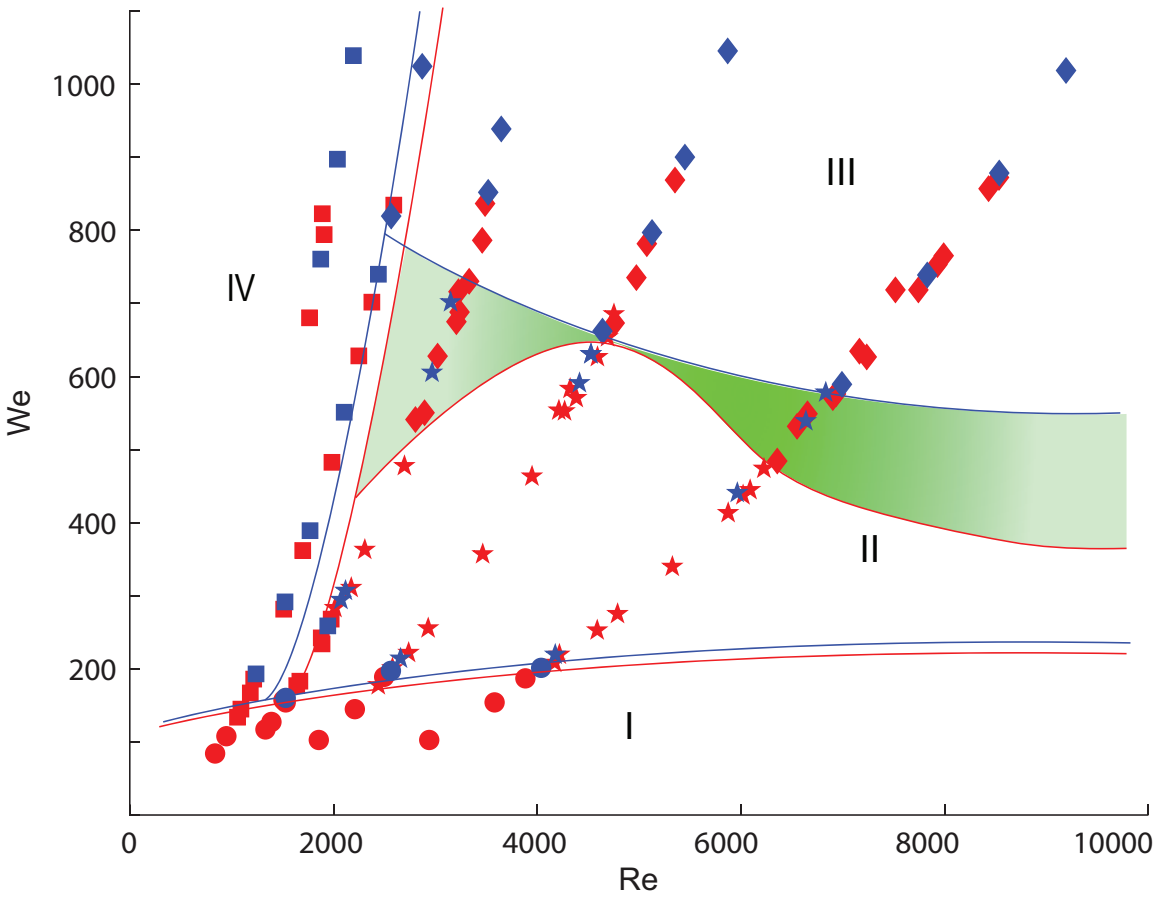

Figure 5.1: Overlapped phase diagrams from various We-Re combinations in vacuum(blue) and air(red). Solid lines are approximate boundaries separating various regimes.

respectively. According to the superimposed phase diagram, the boundary between the two does not shift significantly due to the change of gas pressure. This suggests that emergence of ejecta sheet was not significantly affected by the change in ambient gas pressure. One example of drop impacts event near the boundary is shown in Fig 5.3 (a-b) with no visible change in morphology.

5.3.3 Instability of ejecta sheet

In Regime II, the ejecta sheet forms and remains intact until it folds back to the impacting drop. There are no secondary droplets generated in the process. On the contrary, a drop impact event in Regime III (with higher impact velocity) generates

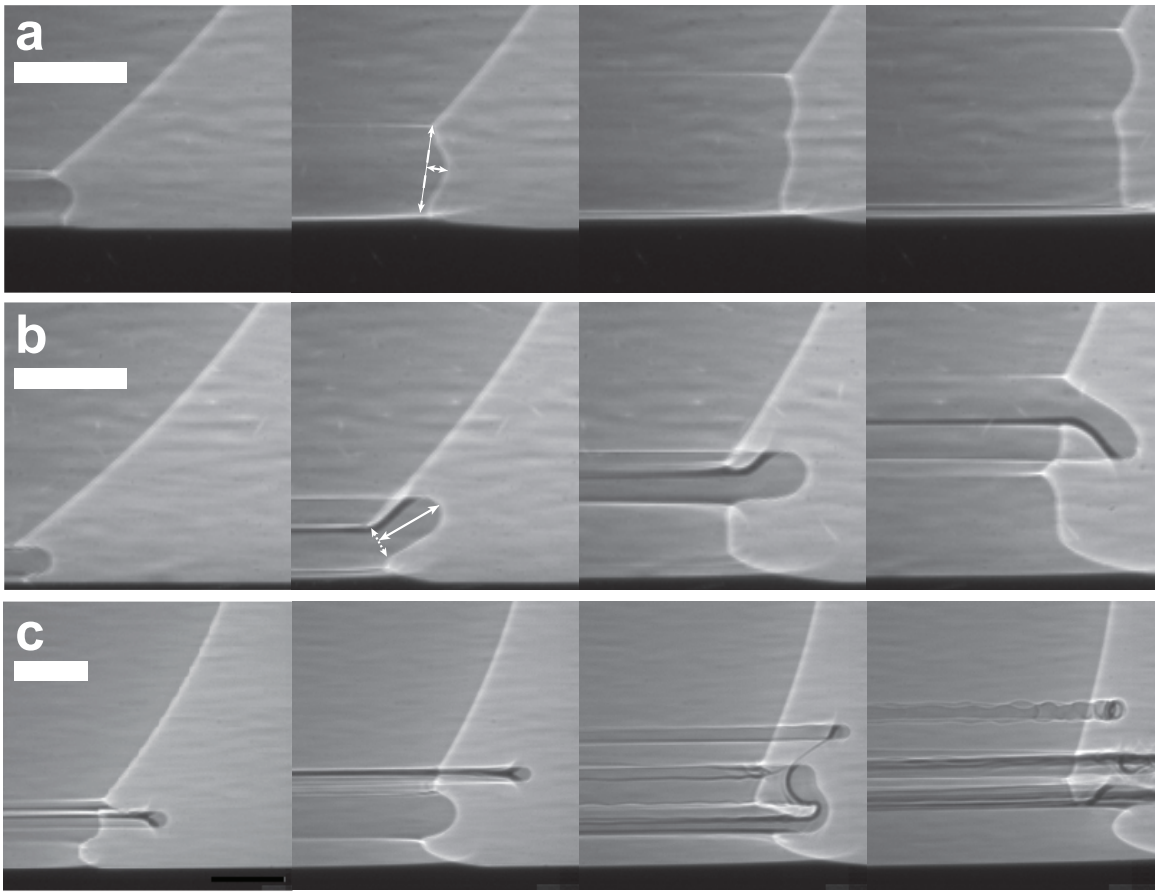

Figure 5.2: X-ray images showing neck region between impacting SO1 drop with diameter $D = 0.18$ cm and a deep pool in atmosphere. a: with a lower velocity a bulge forms ($We = 160$, $Re = 3740$), b: with a higher velocity ejecta sheet forms ($We = 210$, $Re = 4200$), c: with even higher velocity ejecta sheet corrugates and eventually folds back to impacting drop ($We = 470$, $Re = 6400$). The scale bar: 100 μm.

an ejecta sheet more unstable so that it breaks up into secondary droplets. From the phase diagram, there is a significant change in boundary between Regime II and III, which indicates a major role played by the ambient gas pressure in the evolution of the ejecta sheet at higher velocities. There exists a region (marked in green) where the morphology in the partial vacuum are differs from that in the atmosphere: the former does not generate secondary droplets (splash) and the latter does. When we gradually increase the impact velocities, the splash eventually happens for both pressure levels (Fig 5.3 c,d). The droplets generated in the partial vacuum travel

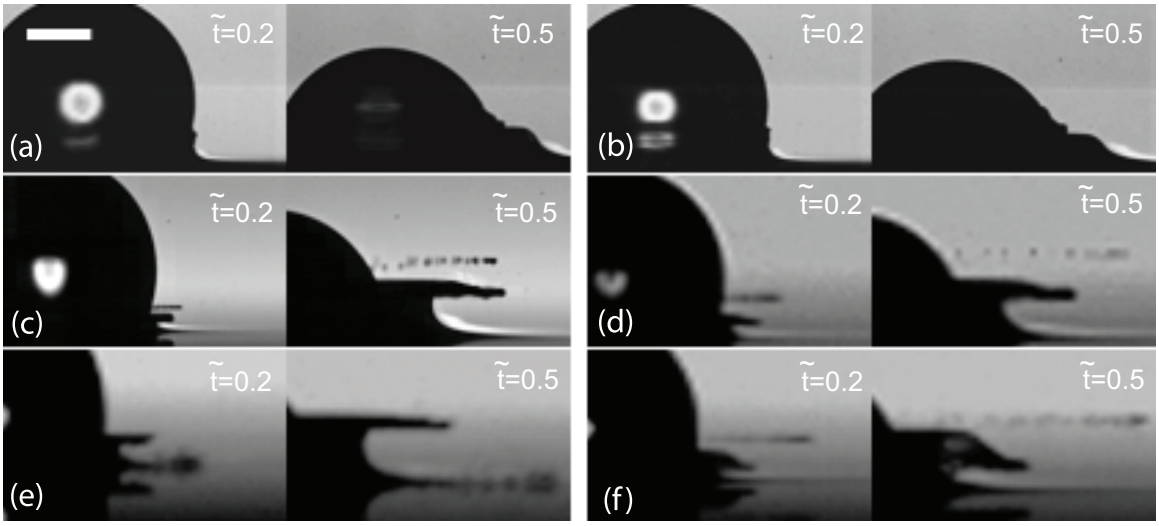

Figure 5.3: Comparison between splash of SO1 drops of $D = 0.17$ cm in normal(a,c,e) and reduced(b,d,f) pressure at three impact speed and dimensionless time $\tilde{t} = 0.2$ and $\tilde{t} = 0.5$. (a)(b): $U = 165$ cm/s, $We = 220$, $Re = 4200$ (c)(d): $U = 270$ cm/s, $We = 600$, $Re = 7000$ (e)(f): $U = 320$ cm/s, $We = 850$, $Re = 8500$. The scale bar stands for 0.5 mm.

faster, which is consistent with less air drag.

The transition from no-splash Regime II to splash Regime III is well illustrated in Fig 5.2 c, which depicts an impact event almost right on the boundary in the phase diagram, and therefore displays features of both regimes. After coming out of the neck region between the drop and the surface, the ejecta sheet folds back due to the surface tension and develops a corrugated rim similar to a crown splash. The torus-shaped rim eventually detaches from the sheet and almost develops into microdroplets before colliding with the impacting drop. With a slightly lower velocity the corrugation is less pronounced and the ejecta sheet remains intact; conversely, with a slightly higher velocity the microdroplets are able to escape from the impacting drop, and thus form a splash. Our data showed this critical velocity is strongly dependent on ambient gas pressure.

5.3.4 Interaction between ejecta sheet and lamella

As we continue to increase the impact velocity far beyond the boundary into Regime III, experiments start to decrease in repeatability by showing a duality of behaviors. Repeated experiments suggest that drop impacts in the atmosphere are more likely to associate with a certain behavior and those in the partial vacuum tend to display the other; though crossovers do occur at times. We compared the statistically-most-probable behaviors associated with both pressure levels. There are at least two features that are significantly different due to change of pressure. First, the trajectories of microdroplets are parallel with the layer surface in the atmosphere (Fig. 5.3 e), but at an angle to the surface in the partial vacuum (Fig. 5.3 f). Second, in both cases the ejecta sheet is followed by a lamella, which remains parallel to the layer surface in the atmosphere but bends significantly downward in the partial vacuum.

In both atmosphere and partial vacuum, different behaviors were observed for events with same impact parameters to the best of our knowledge. We attribute the lack of repeatability to intractable factors such as perturbations caused by the air flow. Fig 5.4 is such an example of the duality of experimental results obtained from the X-ray phase contrast imaging technique. Fig 5.4 a shows an ejecta sheet breaks up at a relatively early time and the microdroplets fly off horizontally in a same manner with Fig 5.3 e. However, for the same impact conditions including the surrounding gas, the ejecta sheet does not break up until a relatively late time (Fig 5.4b). When the ejecta sheet finally breaks, the microdroplets fly at a much higher angle the same way as in Fig. 5.3 f.

The X-ray images in Fig 5.4 reveal features that are obscured and ignored in optical images, therefore enable us to look at the problem from a new perspective. Previous experimental and numerical results put the ejecta sheet on a different timescale with the lamella and ignored the interaction between the two. Our new finding is that

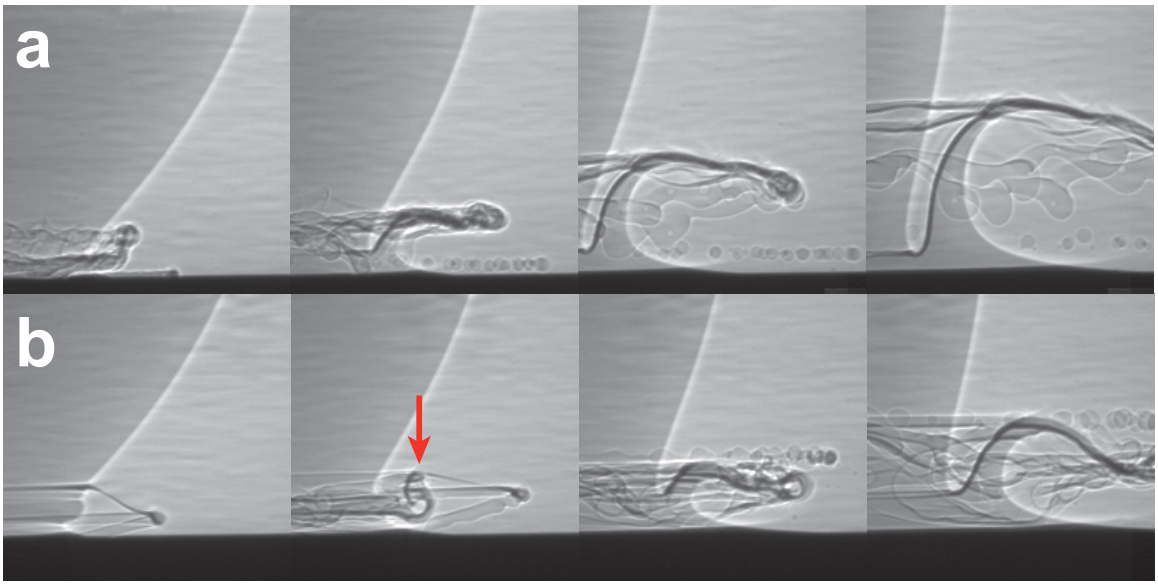

Figure 5.4: Duality of experimental results in atmosphere: a,b have same impact condition: $D = 0.18$ cm, $U = 284$ cm/s, $We = 700$, $Re = 7800$. The scale bar is 100 microns.

the ejecta sheet stays on top of lamella, for a fraction of the lifetime of the ejecta sheet, and pushes the tip of the lamella downward (signified by the red arrow), until the ejecta sheet dissociates into microdroplets and loses this "pushing" effect. In the atmosphere, the ejecta sheet breaks up immediately after impact so that the "pushing" effect does not long enough to bend the lamella, while in the partial vacuum the ejecta sheet lasts longer so that the tip of lamella is pushed downward more significantly.

Depending on the impact velocity, the lamella may also break up into droplets bigger in size than those from the ejecta sheet. Since Regime II and III do not belong to the crown splash regime, the break-up of lamella might be subject to a different type of instability other than the Rayleigh-Plateau instability. For the same impact condition, a drop impact event in the partial vacuum produces droplets more uniform in size, shape and velocity distribution (Fig 5.5).

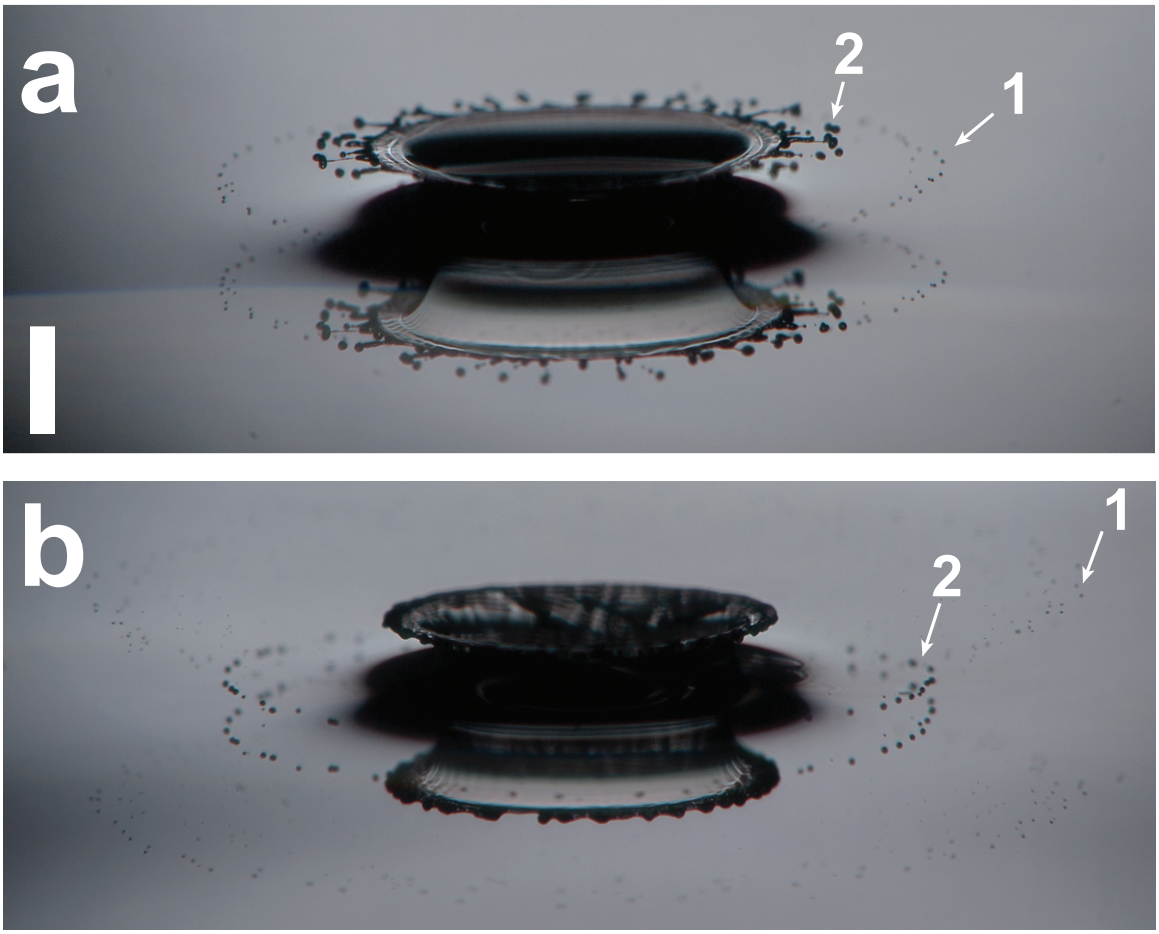

Figure 5.5: Microdroplets (marked as 1) and droplets from lamella (marked as 2) in a: atmosphere and b: partial vacuum. Impact velocity $U = 320$ cm/s, drop diameter $D = 0.17$cm, $We = 800$, $Re = 8000$ and $\tilde{t} = 1$. scale bar: 1 mm.

5.3.5 Crown splash

In Regime IV, the ejecta sheet becomes the leading part of the lamella. Two jets form a single continuous sheet, the rim of which is subject to capillary instability and releases secondary droplets. This process is the so-called crown splash. Crown splash events in different levels of ambient gas pressure also behave differently. First, the tip of the joint liquid sheet bends downward in the atmosphere, while it remains flat in the partial vacuum. The same phenomenon was observed in *Thoroddsen et al.* [2011], in which the authors numerically simulated a bending sheet based on its aerodynamics. Second, for the first time we observed that the rim of the lamella develops stronger

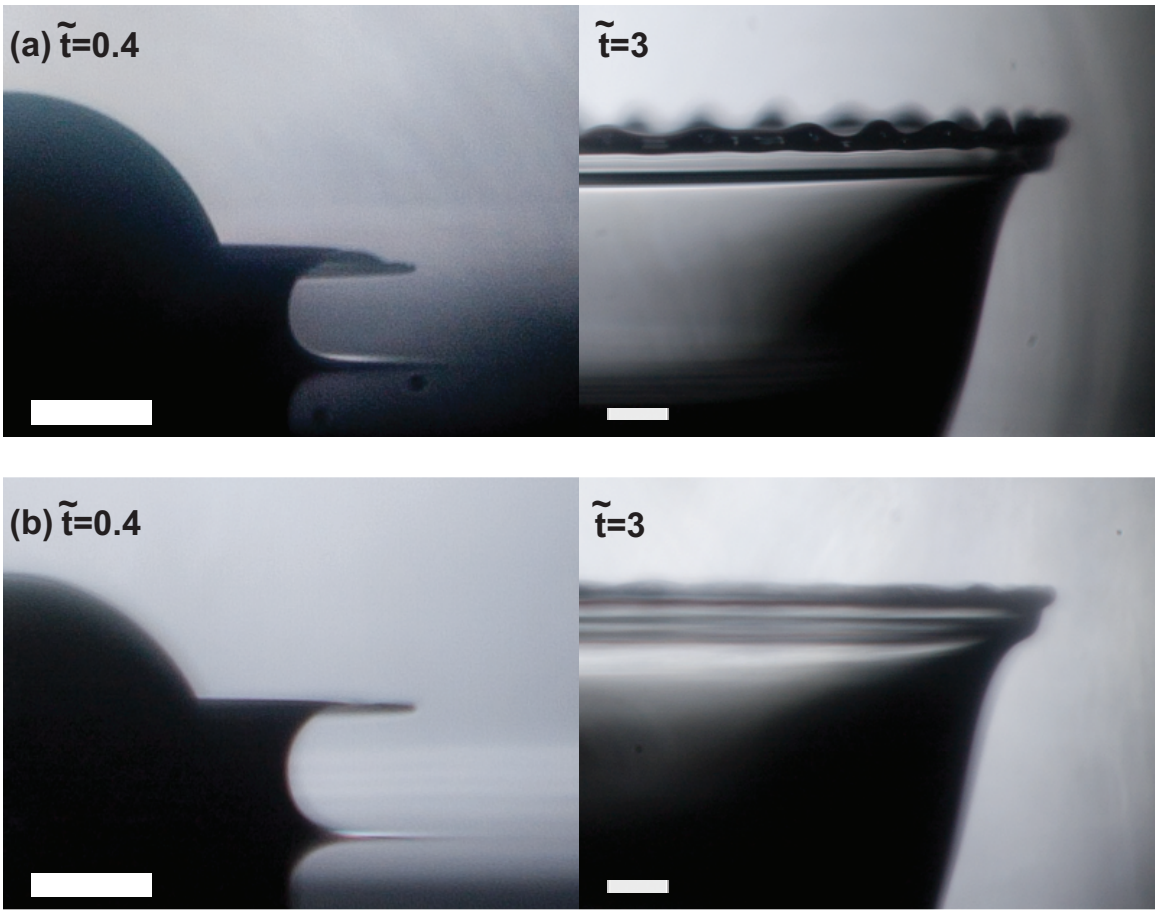

Figure 5.6: Crown splashes created by SO6 with same drop diameter $D = 0.18$ cm, dimensionless layer depth $h = 0.16$ and impact velocity $U = 320$ cm/s at $We = 880$, $Re = 1170$ in normal air pressure(a) and reduced air pressure(b).The scale bars stand for 0.5 mm.

corrugations in the atmosphere than the partial vacuum.

5.3.6 Aerodynamics of ejecta sheet

Our experimental data showed that the ambient gas pressure significantly alters the shape of the ejecta sheet from a high velocity impact but has little effects on that from a low velocity impact. We hereby perform a simple analysis on the aerodynamics of the ejecta sheet that might help us understand the role of ambient gas pressure.

For a reasonable estimate, we assume the leading edge (rim) of the ejecta sheet is a cylinder according to Fig 5.2. Let L be the characteristic length scale of the rim;

the drag force on the rim per unit length is then $F_D = \frac{1}{2}\rho C_D U^2 L$, where U is the characteristic velocity of the ejecta sheet. The drag coefficient of a cylinder C_D is a function of $Re = \frac{\rho U L}{\eta}$, which is on the order of 10 for a typical ejecta sheet. According to *Tritton* [1988] (pp.32-33), for lower Re, $C_D \propto Re^{-1}$, which produces

$$F_D = \frac{1}{2}\rho C_D U^2 L \propto \rho Re^{-1} U^2 L \propto \eta U \tag{5.1}$$

Since the dynamic viscosity of the gas does not change with pressure (*Maxwell* [1866]), the air drag remains independent of ambient gas pressure. This explains the minimal change brought by the partial vacuum at low impact velocities. On the other hand, higher impact velocities result in greater Re and $C_D \approx 1$, which renders

$$F_D = \frac{1}{2}\rho C_D U^2 L = \frac{1}{2}\rho U^2 L \tag{5.2}$$

A greater pressure results in a greater density ρ, which in turn increases the air drag. This is consistent with the fact that the ejecta sheet is bent more significantly in the atmosphere than in the partial vacuum for high velocity impacts.

In addition to the bending effect, we also see that the ejecta sheet is more unstable with a higher gas pressure. *Krechetnikov and Homsy* [2009] proposed that the ejecta sheet is subject to Rayleigh-Taylor instability, which leads to the eventual break-up of the sheet. Assuming this is the case, when the air drag adds on to the deceleration of the ejecta sheet, the most amplified mode grows more rapidly and speeds up the instability on it. However, further investigation is needed before we are certain on the role played by the air drag in the destabilization of the ejecta sheet.

5.4 Discussions

We studied drop impacts on a liquid layer with various impact parameters and found that the ambient gas pressure plays an important role at high impact velocities,

in which the change in the ambient gas pressure leads to a different shape of the ejecta sheet and a different growth rate of the instability on its rim. On the other hand, drop impacts at lower velocities are not susceptible to the change in pressure. In particular, the emergence of the ejecta sheet is independent of the ambient gas pressure, at least with the resolution provided in our experiments. Additionally, both the ejecta sheet and the lamella are more unstable with higher ambient gas pressure, which suggests a higher level of noise introduced to the system with a increasing gas pressure.

There are still several areas to explore in the future. First, we poorly understand the role played by the air drag in the destabilization of the ejecta sheet. The answer to that depends largely on obtaining images that clearly demonstrate the corrugation on the ejecta sheet. Second, we only tested effects of the density of gas but could not effectively change its dynamic viscosity, since it does not strongly depend on the pressure or the type of gas.

CHAPTER VI

Inadequacy of conventional scaling

6.1 Introduction

The primary components of a splash from the impact of a drop with a liquid layer have been known for over a hundred years. *Worthington* [1882] showed that on impact a cylindrically-symmetric jet forms, grows, and disintegrates into a spray of secondary droplets. Nonetheless, many basic details of this process remain obscure. How many jets are there? What sets their size and speed? What is the origin of the symmetry breaking instability? What is the size distribution of droplets that comprise the splash? In order to investigate these issues we used high-speed X-ray and visible imaging to probe one of the simplest splashing scenarios: normal incidence of a single spherical drop onto a deep pool of the same liquid.

That there is more than one jet was first discovered in numerical simulations (*Weiss and Yarin* [1999]) and later confirmed by experiments (*Thoroddsen* [2002]). *Weiss and Yarin* [1999] showed that upon impact a thin fast jet was ejected from the neck between the drop and the incident pool. Here we call this jet the *ejecta*, the jet observed by Worthington – which is slower, emerges later, and produces the so-called crown splash – the *lamella*, and any production of secondary droplets from the disintegration of a jet *splashing*. *Zhang et al.* [2012a] showed that the lamella and ejecta are separate entities at high Reynolds number but join into a single jet at low

	Fluid	Viscosity (cp)	Density (g/cm^3)	Surface tension (dyne/cm)	Drop Diameter (cm)
silicone oil	SO	0.49	0.759	15.7	0.176
pyridine	PYR	0.88	0.957	38.0	0.184
glycerol-water solution	GW	1.30	1.038	66.0	0.224

Table 6.1: Physical properties of experimental fluids.

Reynolds number. Here we show that there is at least one more jet.

The question of the size distribution of secondary droplets is intimately tied to the number of jets, their size, and their instabilities. In the course of determining these parameters we discovered that the standard parameterization based on the Reynolds and Weber number is insufficient to account for the splashing threshold. Furthermore, we identified the onset of the instability that leads to splashing and found that neither can this threshold be accounted for with only the Reynolds and Weber number. We investigated the dependence on the surrounding gas as a potential source of these discrepancies. Our experiments show that the instability threshold is sensitive to the gas's dynamic viscosity, but not its density, unlike the dry drop impact case (*Xu et al.* [2005],*Xu* [2010]).

6.2 Experimental Setup

In our experiments a drop fell through a fixed height on to a deep pool of the same liquid. We used high speed video with visible light and X-rays to observe the ensuing dynamics. Our experiments were conducted with a low-viscosity silicone oil (nominally 0.65 cSt, Clearco), a 11.1:100 v/v glycerol-water mixture, and pyridine (Sigma-Aldrich). We measured the kinematic viscosity of these fluids with a Cannon-Fenske routine viscometer, their density with a Gay-Lussac bottle, and their surface tension with a Wilhelmy plate apparatus. These properties are listed in Table 6.1. These particular liquids were chosen because they had the same Ohnesorge number

Gas	Viscosity (centipoise)	Density (10^{-3} g/cm^3)
air	1.849×10^{-2}	1.1840
helium	1.985×10^{-2}	0.16353
sulfur hexafluoride	1.535×10^{-2}	6.0380

Table 6.2: Physical properties of experimental gases.

$Oh = \eta/\sqrt{\gamma\rho D}$ where η is the dynamic viscosity, γ is the surface tension, ρ is the density, and D is the drop diameter. All experiments were done at ambient temperature: 21 ± 1 ^{o}C for the visible light measurements and 22.3 ± 0.2 ^{o}C for the X-ray measurements. We assumed that the minor variation of the physical parameters between different experiments due to temperature differences was negligible.

While the physical properties of the fluid are fixed, the diameter of the drop depends additionally on the method of production. Each drop was formed on the tip of an electrically grounded sewing needle, fed by a hypodermic needle connected to a reservoir or to a syringe pump when better control of the interval between drops was needed. The sewing needle/hypodermic needle combination is superior to a hypodermic needle by itself because the conical tip of the needle produces drops with less surface oscillations, more uniform drop diameters, and less variability of the impact site. The diameter of the drops for each particular fluid is listed in Table 6.1; variation of the diameter was less than 3% and was primarily due to minor variations in the size of different sewing needles. The drop diameters were typically about 2 mm and showed minor distortion due to air drag when falling through air; for the largest fall heights the horizontal width of the drop was 3% bigger than than its vertical height.

The pool on which the drop impacted was formed in a circular container 10 cm wide and 5 cm deep. Experiments with smaller containers (order 1 cm) did not alter the results, and thus the horizontal and vertical extents of the pool were effectively infinite. Impact speeds ranged from 1.2-3.5ms/s. The interval between successive

impacts was kept long to allow waves from the previous impact to dissipate.

The surrounding gas was changed by enclosing the system within a plastic bag (X-ray measurements) or a chamber (visible measurements) and pushing out the air with either helium or sulfur hexafluoride (SF6). A slow flow of the replacement gas was maintained throughout the experiments and vented through a small orifice at the bottom or top in case of helium or SF_6, respectively, to ensure a pure environment. The properties of gases are listed in Table 6.2 (*Lemmon et al.* [2010]).

Our visible light measurements were obtained with a high speed video camera (Phantom v11, Vision Research) fitted with a 1.4-9.0X zoom lens (Navitar 6000) or a 60 mm f/2.8 macro lens (Nikon). Our X-Ray measurements were conducted at the Advanced Photon Source at Argonne National Laboratory using a phase contrast technique [*Fezzaa and Wang*, 2008b]. The X-rays traversed horizontally through the splash and were imaged on a scintillator crystal with a high speed video camera (SA1.1, Photron). The X-ray data consisted of gray scale images in which greater absorption produced darker shades. In addition, the phase contrast technique highlights the interface of the fluid parallel to the beam with a dark or light halo. The advantage of X-ray imaging is that it reveals the structure of a splash that would be obscured in visible light by reflections and refraction from the interfaces and out-of-focus features.

6.3 Results & Discussion

6.3.1 Inadequacy of conventional scaling

The impact of a drop with a layer of the same fluid is conventionally described by six physical quantities: the impact velocity U, the drop diameter D or radius R, the fluid's properties (γ, ρ, η), and the acceleration due to gravity g. Non-dimensionalizing time with D/U and length with D yields a parametrization in terms of the Weber number $We = \rho DU^2/\gamma$, Reynolds number $Re = \rho DU/\eta$, and Froude

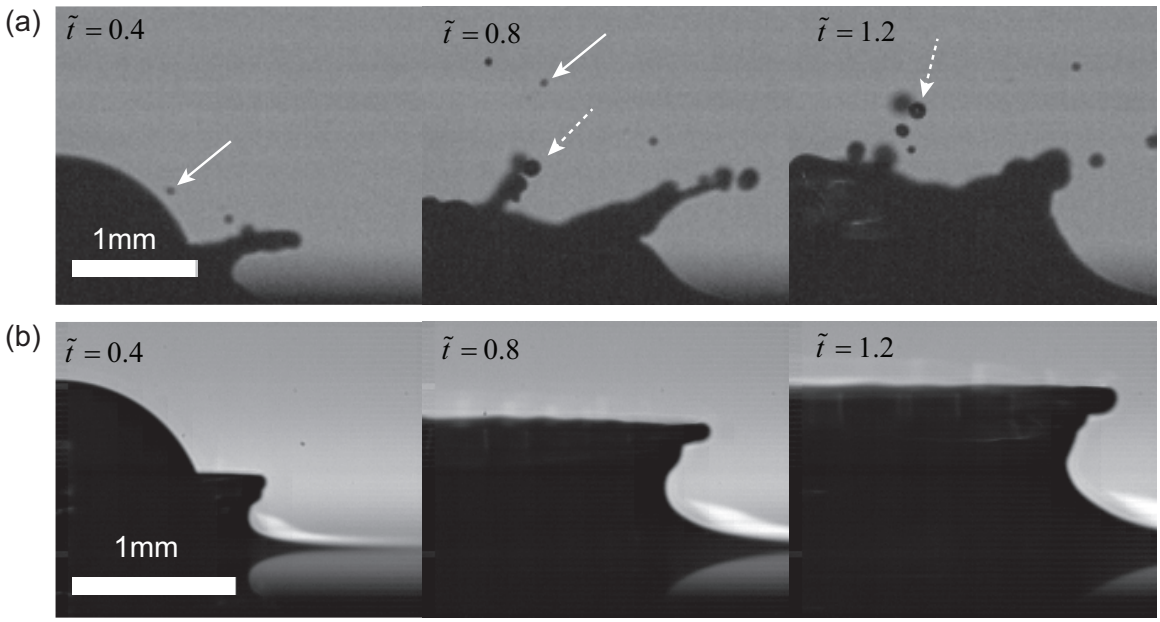

Figure 6.1: Optical images of drop impact with (a) a glycerol-water mixture at $Re = 5450$, $We = 330$ and (b) a low viscosity silicone oil at $Re = 5330$, $We = 340$ at the indicated normalized time $\tilde{t} = Ut/D$. Despite almost identical experimental conditions the event in (a) produces a splash of microdroplets (solid arrows) and intermediate droplets (dashed arrows), while the event in (b) produces no secondary droplets. The images are scaled to equal drop diameters ($D = 0.22$ cm and $D = 0.18$ cm for the GW and SO, respectively), i.e. to the same non-dimensional length scale.

number $Fr = U^2/gD$. Hereafter we refer to this set of non-dimensional numbers as the conventional parameterization. Experiments almost universally ignore the Froude number dependence (see *Cossali et al.* [1997], *Rioboo et al.* [2003], *Deegan et al.* [2008]) because the acceleration due to gravity is negligible on the timescale of a splash. The conventional parameterization also neglects the surrounding gas based on the low density ρ_g and low dynamic viscosity η_g of the gas relative to those of the liquid: typically $\rho_g/\rho \approx 10^{-3}$ and $\eta_g/\eta \approx 10^{-2}$.

We tested the conventional parametrization by observing the qualitative character of splashes from drop impact on a deep pool of the same liquid with three different fluids at the same We and Re number. For any particular fluid $We^{1/2} = Oh \cdot Re$. The fluids in our experiment (SO: silicone oil; GW: glycerol-water mixture; PYR:

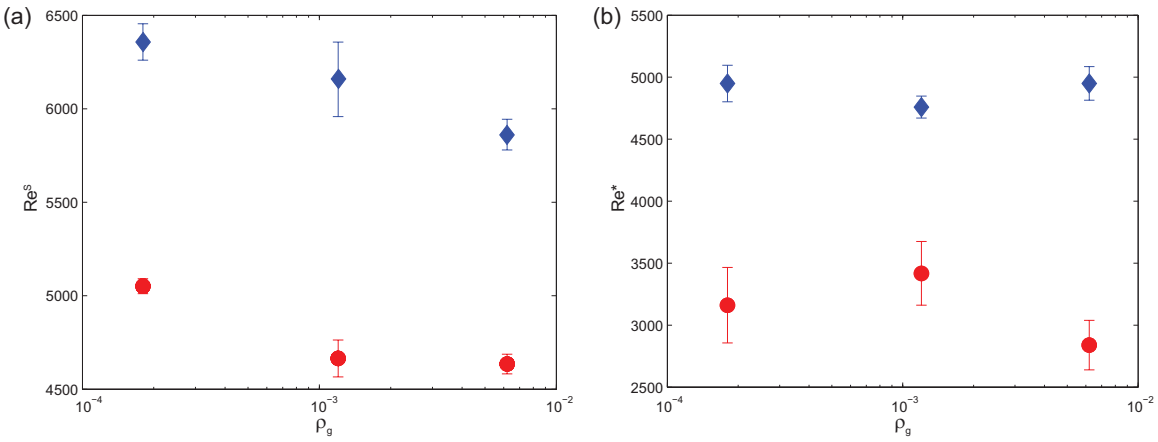

Figure 6.2: (a) Reynolds number threshold for onset of splashing, defined as the appearance of secondary droplets, in GW (red circles) and SO (blue diamonds) versus density of the surrounding gas. These data correspond to helium, air and SF_6 going from left to right. (b) Reynolds number threshold for onset of instability in GW (circles) and SO (diamonds) versus density of the surrounding gas. Note: the symmetry-breaking criterion gives a lower threshold than splashing criterion because at lower values of Re the ejecta is reabsorbed before the instability produces fragmentation.

pyridine) had the same $Oh = 3.4 \times 10^{-3}$. Therefore, experiments with one fluid at any particular combination (We, Re) could be repeated with the other two fluids. If We and Re do indeed provide a complete specification as expected from the conventional parameterization, experiments with any of the three fluids ought to be identical at the same Re. (Given that in our experiments $We = Oh^2 \cdot Re^2$ and Oh is a constant, Re is sufficient to specify the experiment; hereafter we only report Re).

Figure 6.1 shows impact events for GW (above) and SO (below) with almost equal $Re \approx 5400$. The impact in GW produces a splash while the one in SO does not. Moreover, Fig 6.2 shows that Re^s, defined as Re at which secondary droplets first appear, is 1500 greater for SO than GW. This discrepancy suggest that the conventional scaling is inadequate.

We find further confirmation of this discrepancy using X-ray imaging. Figure 6.3 shows the evolution of the ejecta as it emerges from the neck between the drop and the substrate fluid at $Re \approx 4500$. The ejecta for GW displays non-axisymmetric

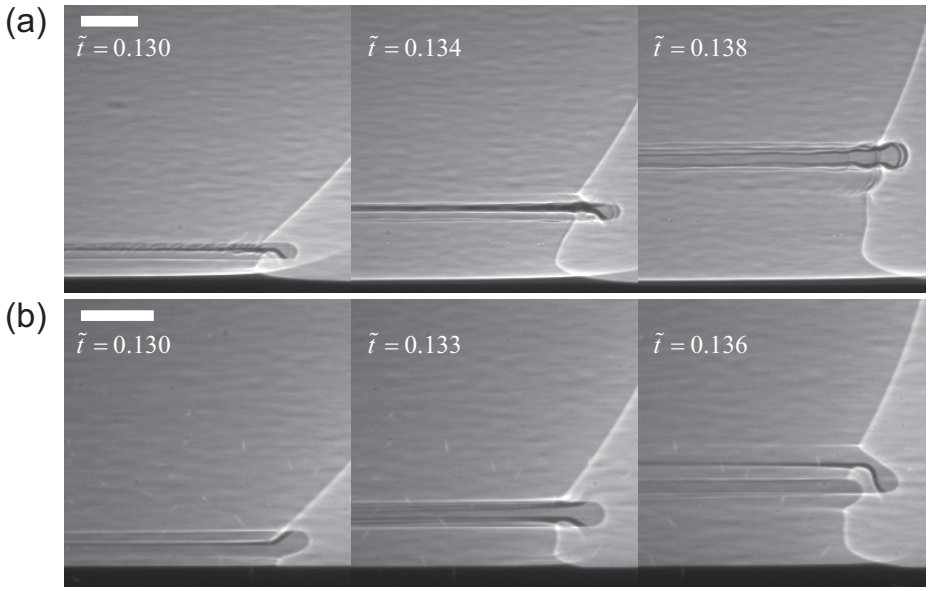

Figure 6.3: Ejecta sheet emerging from the neck connecting a drop (dark gray) and the pool (black) for (a) GW at $Re = 4540$, $We = 230$ and (b) SO at $Re = 4430$, $We = 230$ at the indicated scaled time $\tilde{t} = Ut/D$. The images are scaled to equal drop diameters ($D = 0.22$ cm and $D = 0.18$ cm for the GW and SO, respectively). The scale bars correspond to 100 μm. The X-rays are highly attenuated after traversing the full width of the pool and thus the pool appears as a black band at the bottom of each image.

structure which grows into a pronounced corrugation. In contrast, the ejecta from SO is smooth, exhibiting no signs of instability. The instability in GW first appears at $Re = 3400$. We define a new threshold Re^* as the Re at which the ejecta first shows signs of instability. This threshold is plotted for the GW and SO in Fig 6.2; again, we find that Re^* for GW is about 1500 lower than for SO.

The splashing threshold is higher than the instability threshold because for $Re^* < Re < Re^s$ the ejecta collides with the bulk of the drop and is reabsorbed before the corrugations develop into droplets. For $Re > Re^s$ the corrugation visible in Fig 6.3 breaks-up into the small secondary drops shown in Fig 6.1, which we call *micro-droplets*; the larger drops, which we call *intermediate droplets* are from a different source; we return to this issue is Section 6.3.5.

Our X-ray measurement were for GW and SO. To assure ourselves that the ob-

	X-Ray method	Optical method
GW	3420	3730
PYR	n/a	4030
SO	4760	5160

Table 6.3: *Re* threshold in air as determined with X-ray and optical imaging.

served discrepancy in the fluid was not due to some unrecognized peculiarity of either fluid, we added a third fluid pyridine. Health and safety constraints precluded using pyridine at the Advanced Photon Source. Instead, we employed a visible light method to determine the instability threshold. We focused with a high magnification lens on the contact region of the drop and the pool, and determined the onset the instability from the appearance of a spatial modulation of the light reflected from the rim of the ejecta. As shown in Table 6.3, the light based detection of the threshold is less sensitive than with X-rays but nonetheless is accurate to better than 10% in the cases for which we could cross-check with X-ray measurements. Table 6.3 shows that all three fluids exhibit a different instability threshold confirming the threshold shift observed with just two fluids.

The discrepancy in both the splashing and instability thresholds indicates that something is missing from the conventional scaling. We considered whether temperature variations, drag induced vortices in the drop, drag induced deformations of the drop, or oscillations of the drops could account for the discrepancy. We estimated that these effect are at most 1-2% effects which is far too small to account for the observed shifts of 30-40% in the thresholds.

6.3.2 Role of the surrounding gas

There is mounting evidence that the surrounding gas, despite its tenuous physical properties, can qualitatively affect splashing. Notably, for drop impact on a dry substrate *Xu et al.* [2005] found that a reduction of the gas pressure eliminated splashing,

and for impact on a wet substrate *Thoroddsen et al.* [2011] showed that drag from the surrounding gas distorts the shape of the lamella, so much so in some cases that the lamella collides with the pool. We thus set about determining if the gas mattered, and if so, which particular property was responsible for the threshold shifts.

Augmenting the conventional parametrization to include the gas introduces two additional dimensionless parameters: the density ratio ρ_g/ρ and the viscosity contrast $\Lambda = \eta_g/\eta$. We examined the effect of these parameters in our experiments. As in air, we determined the lowest Re at which instability appears on the ejecta of GW and SO in two gases (He and SF6) using X-ray imaging. These data are plotted versus gas density in Fig 6.2. Despite varying the density by almost two decades, Re^* remains unchanged within the uncertainty of our measurement. We concluded that the gas density is insignificant in determining the onset of the symmetry breaking instability that leads to splashing. Note that the gas density does influence the threshold of splashing Re^* (Fig 6.2a), which happens much later the instability onset.

In particular, the result rules out drag from the gas as a potential cause of Re^* shift. The Reynolds number for the ejecta in gas is $Re_j = \rho_g u_j \delta/\eta_g$, where δ and u_j are the ejecta thickness and speed. From measurements $u_j \approx 10U$ (*Zhang et al.* [2012a]) and $\delta \approx 10^{-2}D$, and $Re_j \approx 10^{-2}Re \approx 30$ for typical experimental values of Re. For this value of Re_j the drag is in the inertial regime and proportional to the gas density, but since there was no observable effect of the gas density it follows the drag is not responsible for the shift.

The insensitivity of the instability threshold of the ejecta to the density of the gas shows that if the gas is influencing the experiments then it can only be through a coupling of the gas and fluid that depends exclusively on the ratio of their viscosities. The viscosity of the gases does not change significantly (see Table 6.2), but the viscosity of the fluids do. Figure 6.4 shows a plot of the optically determined instability threshold Re^*_{op} versus Λ. These data show that the threshold increases linearly with

Λ, i.e. the threshold is shifted upward for a greater viscosity of the gas relative to that of the fluid.

6.3.3 The trapped disk of gas

The dependence of the threshold on the gas viscosity but not density hints at the action of a low Reynolds number flow in the gas. The most conspicuous location for the latter is the gap between the drop and the pool. Indeed, prior to impact the gas between the drop and the pool must be drained from between the two bodies. *Smith et al.* [2003], *Mandre et al.* [2009], *Duchemin and Josserand* [2011] showed numerically that in the case of drop impact on a solid substrate the lubrication pressure leads to the formation of a dimple at the base of the drop. These calculations are consistent with experimental observations of a trapped bubble for drop impact on a solid surface (*Chandra and Avedisian* [1991], *Driscoll and Nagel* [2011], *Van Der Veen et al.* [2012], *Kolinski et al.* [2012]). Extrapolating these results to the case of drop impact on a liquid surface suggests that the disk of air observed by *Thoroddsen et al.* [2003] and in our experiments is caused by the same mechanism: the lubrication pressure of the surrounding gas causing a local deformation of the liquid surfaces.

We measured the initial size of the disk for all three liquids at various impact speeds. In these experiments the impact was viewed from directly below through the liquid and container, both of which were transparent. The disk shrinks within ≈ 30 μs by an order of magnitude to form a spherical bubble. In order to identify the initial radius of the disk, we filmed multiple impact events for the same experimental conditions at 210,000 frames-per-second, measured the radius of the disk for each event from the first video frame in which it appears (i.e. when it is largest), and selected the largest of these as the initial disk size R_b. The typical size of R_b, 2×10^{-2} cm, is consistent with magnitude expected from balancing lubrication pressure and inertia (see Appendix B).

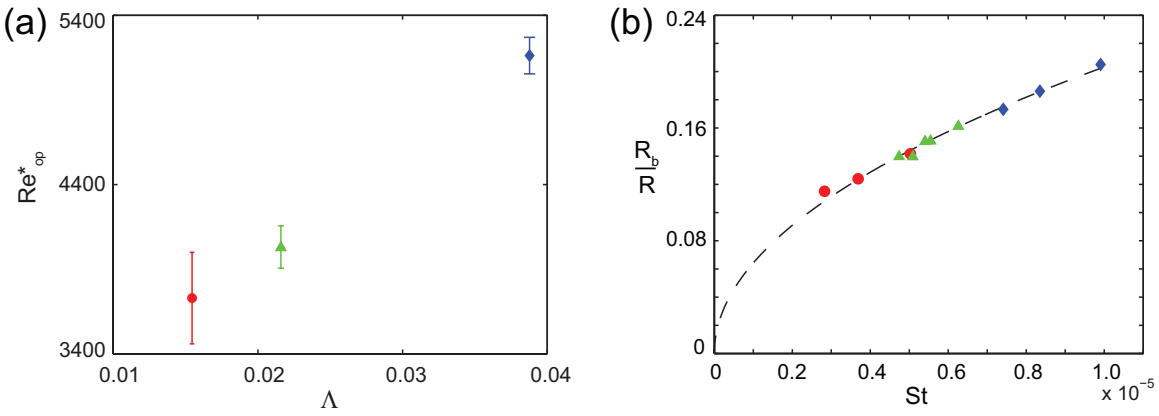

Figure 6.4: (a) Reynolds number threshold determined optically versus viscosity contrast for GW (red circle), pyridine (green triangle) and SO (blue diamond) in air at 1 atm. (b) Maximum disk radius normalized by the drop radius versus Stokes number for GW (red circles), Pyridine (green triangles) and SO (blue diamonds). The dashed curve is the best fit to power law which yields and exponent of 0.5. Note: R_b increases with Λ.

The disk radii normalized by the drop radius are plotted in Fig 6.4 versus Stokes number $St = \eta_g/\rho U D$. The data for all liquids collapse to a single curve in agreement with the scaling based on the Stokes number predicted in the dry impact problem (*Mandre et al.* [2009], *Duchemin and Josserand* [2011]). Although we find $R_b \sim St^{0.5}$, our data covers less than a decade and thus the difference in our measured exponent and the 1/3 of *Mandre et al.* [2009], *Duchemin and Josserand* [2011] may not be significant. Since $St = \Lambda/Re$, these data show that R_b increases with Λ. Moreover, the magnitude of the bubble size is consistent with a balance of the lubrication pressure and inertia.

6.3.4 Connection between gas disk and ejecta

The scaling of the disk radius with Λ suggests a connection between the gas disk and the evolution of the ejecta. Certainly it is plausible that if the gas is interfering with the merger of the drop and the pool, the ejecta would be affected. We speculate on how this might influence the threshold for the instability Re^* on the ejecta.

Increasing the gas viscosity increases the size of the trapped disk as demonstrated

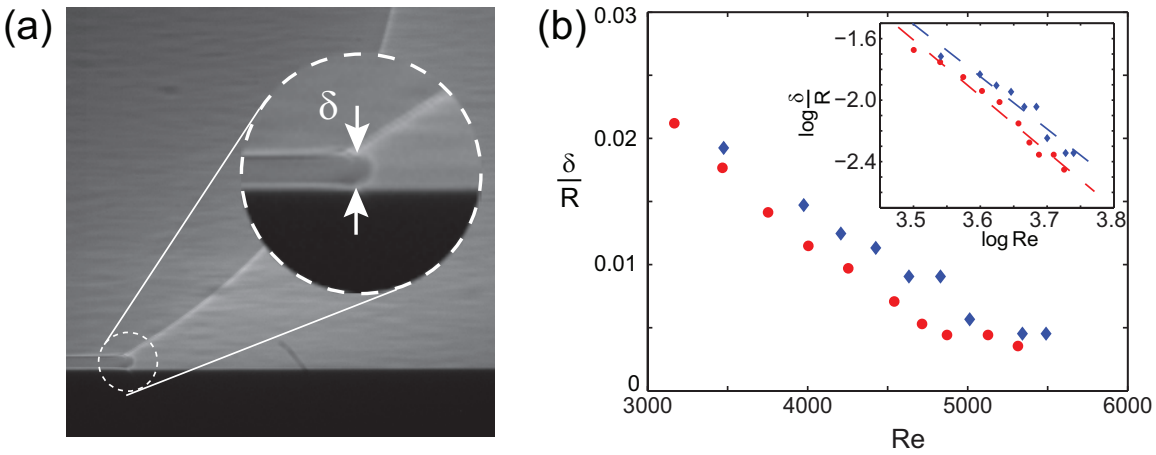

Figure 6.5: (a) Example of ejecta thickness measurement. (b) Thickness of ejecta sheet normalized by the drop radius versus Reynolds number for GW (red circles) and SO (blue diamonds). Note: the thickness is systematically larger for SO than GW at the same Re. Inset: same data plotted on a log-log scale. Dashed lines are best fits to a power law ARe^{α} which yield $A = 0.25 \times 10^{11}$ and $\alpha = -3.4$ for SO and $A = 1.3 \times 10^{11}$ and $\alpha = -3.6$ for GW.

by our measurements. A bigger disk means that point of first contact between the drop and the pool is pushed further from the center. From volume conservation we expect that a bigger area of first contact will lead to a thicker ejecta: the outflow through the ejecta $2\pi R_b \delta u_j$ must balance the inflow from the drop $\pi R_b^2 U$, and thus $\delta u_j = R_b U/2$.

While in principle either δ or u_j could compensate for an increase in R_b, in practice we find that the ejecta thickens. We measured the ejecta's thickness when it first emerges from the neck connecting the drop and the pool. An example of this is shown in Fig 6.5(a). The precision of this measurement is limited at 10% by pixelation. The thickness of the tip of the ejecta varied by less than 10% in subsequent frames (20 μs apart) in accord with the limited Taylor-Culick contraction expect at these short timescales. The thickness data is plotted in Fig 6.5(b) versus Re. These data show that the ejecta is systematically thicker at all Re for the liquid with the bigger R_b, i.e. SO.

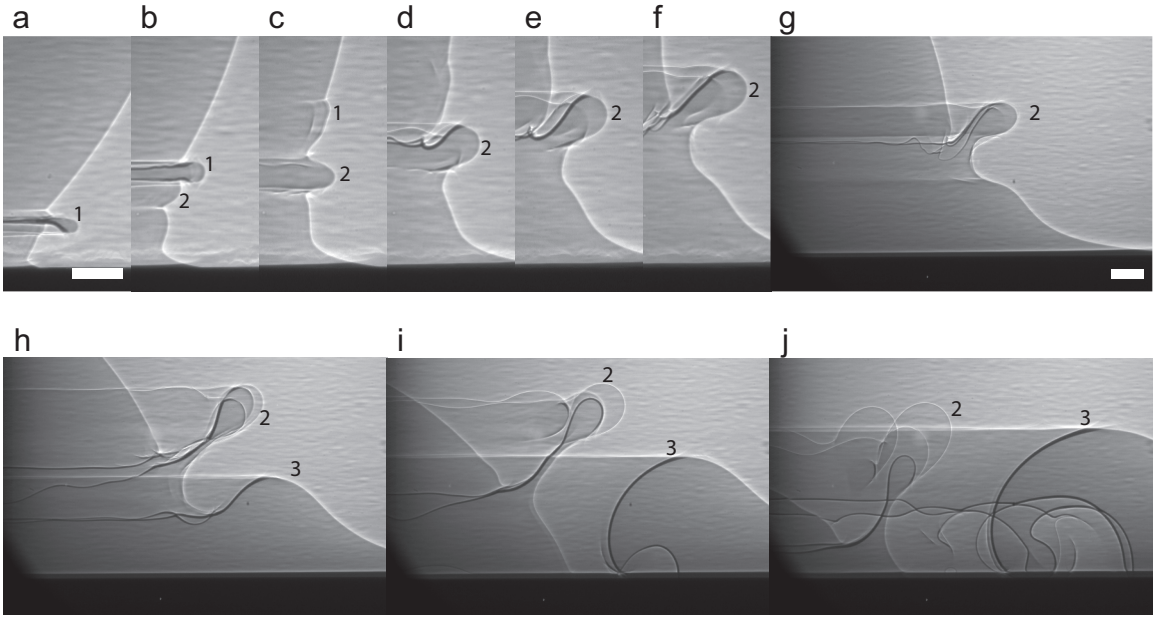

Figure 6.6: X-Ray phase contrast images showing ejecta (1), secondary ejecta (2) and lamella (3) of GW splash at $We = 230$, $Re = 4540$ with scaled time $\tilde{t} = Ut/D$. The scales bars in (a) and (g) equal 100 μm. The sequences (a-f) and (g-j) are from different impact events with the same experimental conditions. Note: the primary ejecta sheet is present in only the first two frames before being absorbed into drop between frame (b) and (c) leaving the ripples on the drop surface visible i (c). The lamella comes out much later in frame (h). (a) $\tilde{t}$=0.13; (b) $\tilde{t}$=0.17; (c) $\tilde{t}$=0.21; (d) $\tilde{t}$=0.24; (e) $\tilde{t}$=0.28; (f) $\tilde{t}$=0.32; (g) $\tilde{t}$=0.34; (h) $\tilde{t}$=0.50; (i) $\tilde{t}$=0.66; (j) $\tilde{t}$=0.82.

To complete the argument we assume that the instability is caused by capillarity as in the case of the crown splash *Zhang et al.* [2010]. This assumption is consistent with the timescale at which we observe the appearance of the instability: the inverse growth rate for the Rayleigh-Plateau instability in non-dimensional time units is $\sqrt{We(\delta/R)^3}$ and is ≈ 1. A greater δ (thicker ejecta sheet) results in a longer characteristic time for the development of the instability and thus a more stable ejecta sheet. In summary: higher gas viscosity produces a bigger disk; a bigger disk produces a thicker ejecta; and a thicker ejecta is more stable.

6.3.5 Multiplicity of jets

The splash in Fig 6.1 shows two distinctly sized sets of secondary droplets. Neither set of droplets are due to the lamella which at that time is just beginning to rise from the pool. X-Ray images in Fig 6.6 show two distinct jets from which the two sets of droplets detach. The first to appear and smaller set of droplets visible in Fig 6.1 are the result of the disintegration of the ejecta labeled with the numeral "1" in Fig 6.6. (At Re=4540 the impact event in Fig 6.6 is below the splashing threshold and thus the jets do not break up.) The second set of droplets emerge later and come from the disintegration of a second jet, labeled with the numeral "2" in Fig 6.6. Long after this second jet has emerged, the lamella begins to form. Hence, the second jet is distinct from both the ejecta and the lamella.

6.4 Conclusions

We conducted experiments of drop impact into a deep pool of the same liquid with three different liquids at the same We and Re in the high-Re/low-We regime. We demonstrated that the conventional scaling based on Re and We is insufficient to predict either the threshold for the generation of secondary droplets or the threshold for the instability which leads to the production of secondary droplets. Though the density of the surrounding gas seemed a likely candidate to explain the observed deviations based on previous results *Xu et al.* [2005], our experiments show that the effect of density is negligible. Instead our experiments show that the ratio of the dynamic viscosity of the gas and the liquid correlates well with the observed shift in the splashing threshold. We proposed that the disk trapped between the drop and the pool when these merge is responsible for this shift. We also discovered a third jet, distinct from the ejecta and lamella, which produces droplets of intermediate size to those from the ejecta and lamella.

CHAPTER VII

Conclusion

In Chapter I, I formulated an idealized problem: a spherical liquid drop made of Newtonian fluid impacts normally onto a uniform liquid layer of the same liquid. For the experimental range in our study, we safely ignored the compressible effects of liquid and the influence from gravity. The problem is described by the Navier-Stokes equation with boundary conditions, the solution of which often requires numerical methods. I also characterized the problem using a dimensionless group based on the dimensional analysis. We then gave a brief introduction on various features of the problem followed by related numerical and experimental techniques.

I studied the dynamics of the lamella, using a high speed X-ray phase contrast imaging technique described in Chapter II. With the ability to detect the interface between liquid and air, I obtained quantities such as the thickness and the velocity field of the lamella experimentally for the first time. Our data support the previous results on the crown radius, but disagree with those on the base radius. We found that for a very short period of time after impact, the behavior of the lamella is independent of the layer depth. This is probably due to the fact that the impacting does not feel the layer bottom before a certain response time. We later used the same experimental technique to probe various features of the problem and proposed future work that may benefit from this novel observation method.

The crown splash has a clean and representative morphology since the ejecta sheet and the lamella joint into one and only jet. As the jet expands its rim becomes larger due to the surface tension pulling the edge back into the jet and is susceptible to a capillary instability. The mechanism for such instability was the focus of Chapter III. By performing many experiments for same parameter values, we showed that the power spectrum of the corrugation matches that predicted by the Rayleigh-Plateau instability. The corrugation on the rim is determined by the most unstable wavelength of this instability, and there is an almost one-to-one correspondence between the bumps on the rim in the linear phase and the secondary droplets in the nonlinear phase. Our calculation did not contain adjustable parameters; some values used in the calculation (rim radius and crown radius) were obtained experimentally.

In studies reported in Chapter IV, I investigated the drop impact problem on a deep pool with different liquids and impact velocities. The ejecta sheet and the lamella were not sharply defined in the literature, we provided definitive evidence that they are two distinct jets. In particular, the ejecta sheet and the lamella are separate entities at high Reynolds number and joint into a single continuous jet at low Reynolds number. I studied the dynamics of ejecta sheet by measuring quantities such as the emergence time, the radial position and the speed. We found those quantities scale as power laws with impact speed and viscosity. We also observed secondary droplets of almost equal size from both the ejecta sheet and the lamella. We therefore concluded that size of secondary droplets is not a good indicator of their origin. We still have very limited understanding on origin of the instability on the rim of the ejecta sheet.

Properties of the surrounding gas were often ignored in the literature, except for a few cases where a partial vacuum was reported to alter the morphology of splash. In Chapter V, for a wide experimental range I compared results from impacts within air at two different levels of pressure. I found that ambient gas density alters the shape

of the ejecta sheet and the lamella on a timescale of the drop penetration, however, it does not seem to change emergence of ejecta sheet, at least with the resolution provided in our experiments. The corrugations on both the ejecta sheet and the lamella are more prominent in the higher pressure. Our data suggest a higher level of noise in the system caused by an increasing gas pressure. The dynamic viscosity does not depend strongly on the gas density, and therefore was virtually untested in our experiments.

In research presented in Chapter VI, we focused on the problem in the high-Re/low-We regime, where the instability on the ejecta sheet is prominent. We created drop impacts with same Re and We for various combinations of liquid and gas in an effort to effectively change the density ratio and the dynamic viscosity ratio. We showed that ratio of dynamic viscosity is critical in determining the threshold of instability at a very early time after impact, while the effects of gas density ratio is minimal. Our results put conventional scaling that is based solely on the properties of liquid into question. Additional dimensionless number(s) that describe gas properties must be incorporated into the description of the problem. We also discovered a third jet that produces droplets of intermediate size to those from the ejecta sheet and the lamella.

APPENDICES

APPENDIX A

Illustration of a drop penetrating the layer

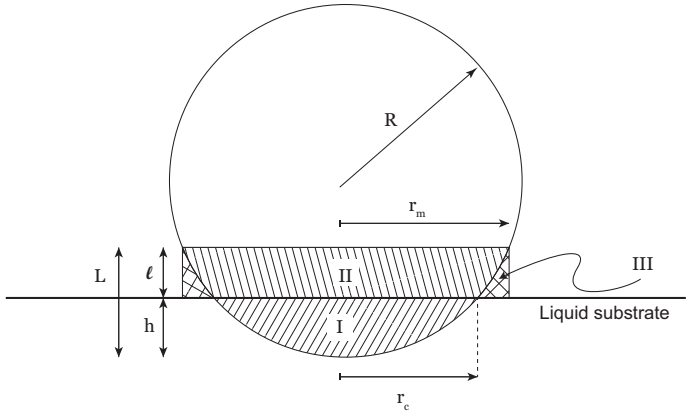

Figure A.1: Graphic illustrating the geometry of a sphere crossing a plane. When a drop collides with a liquid surface, the volume in region I is displaced. Provided the liquid substrate remains equal or above its initial flat configuration, which it does in our experiments, the minimum radius which can contain this volume is r_m. We call the edge of domain III the *front*.

As the drop penetrates the liquid substrate, the volume that lies below the substrate level must be displaced radially. We compute the mean radius r_m that contains this displaced volume. Referring to Fig. A.1, the volume below the liquid substrate's surface V_I must be contained in the annular volume V_{III}. Therefore, $V_I = V_{III}$. Furthermore, by geometry $V_{III} = \pi r_L^2(L-h) - V_{II}$, $V_{II} = V_{cap}(R,L) - V_I$, and $V_I = V_{cap}(R,h)$ where $V_{cap}(r,x)$ is the volume of a spherical cap of height x from a

sphere of radius r: $\frac{1}{3}\pi x^2(3r-x)$. Solving for L yields:

$$L = \frac{3}{4}(R+h)\left\{1 - \sqrt{1 - \frac{16}{3}\frac{Rh}{(R+h)^2}}\right\} \tag{A.1}$$

from which $r_m = \sqrt{2RL - L^2}$ can be computed.

For our experiments $h = Ut$. To leading order at small times $t \ll R/U$: $L \simeq 2Ut$, $r_m \simeq 2\sqrt{URt}$, and $u_m = \frac{d}{dt}r_m \simeq \sqrt{\frac{UR}{t}}$. For reference, the geometrical contact point between the drop and the liquid substrate $r_c \simeq \sqrt{2}\sqrt{URt}$. Similar expressions were derived by *Oguz and Prosperetti* [1989].

APPENDIX B

Estimation of the size of gas disk trapped between the drop and the liquid

We estimate the radius of disk of gas trapped between the drop and the pool by balancing the inertial and lubrication forces. Consider the flow in the gap between the drop and the pool shown in Fig B.1(a). The lubrication equations (*Batchelor* [2000]) are

$$\partial_r p \approx \eta_g \partial_z{}^2 u \tag{B.1}$$

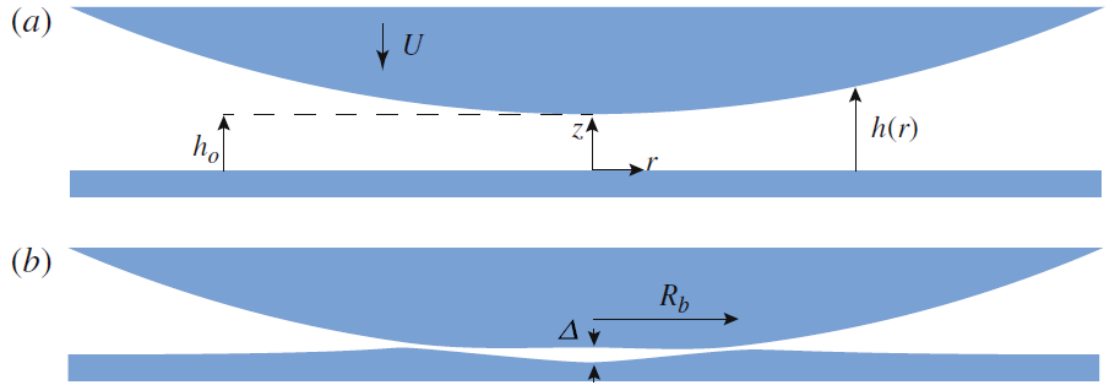

Figure B.1: Schematic of the gas as the drop approaches the pool when (a) the drop is far from pool and (b) the air squeezed between the two bodies causes the interfaces to distort.

$$\partial_z p \approx 0 \tag{B.2}$$

where r and z are the radial and vertical coordinates defined in Fig B.1(a), $u(r,z)$ is the radial velocity component of the gas, and p is the pressure. Solving for p and using volume conservation yields

$$p = 12\eta_g U \int_r^\infty \frac{r\mathrm{d}r}{h^3} \tag{B.3}$$

Approximating the gap profile with a parabola $h \approx h_0 + (r^2/2R)$, the pressure at r is

$$p(r) = \frac{6\eta_g U R}{\left(h_0 + \frac{1}{2}\frac{r^2}{R}\right)^2} \tag{B.4}$$

and the lubrication force $F_L = \int_0^{R_b} 2\pi r p(r)\mathrm{d}r$ over a patch of size R_b when $h_0 = \Delta$ is

$$F_L = 6\pi\eta_g U R\left(\frac{R_b}{\Delta}\right)^2 \frac{1}{1+\frac{{R_b}^2}{R\Delta}} \tag{B.5}$$

Balancing the work by the force against the change in kinetic energy of the fluid pushed aside by the gas yields

$$\frac{1}{2}\rho {R_b}^2 \Delta U^2 = F_L \Delta \tag{B.6}$$

and after rearrangement

$${R_b}^2\Delta = 24\pi St R^3 - \Delta^2 R \tag{B.7}$$

The radius of the disk shrinks by a factor ten as it contracts into a spherical bubble. Assuming the volume of the gas is conserved, we estimate $\Delta \approx 10^{-3} R_b$.

Using R=0.1 cm and $St = 5 \times 10^{-6}$ gives R_b=0.016cm, in good agreement with the typical measured value of 2×10^{-2} cm.

BIBLIOGRAPHY

BIBLIOGRAPHY

Al-Durrah, M. M., and J. M. Bradford (1982), Parameters for describing soil detachment due to single waterdrop impact, *Soil Sci. SOc. AM. J.*, *46*, 836–840.

Allen, R. F. (1988), The mechanics of splashing, *Journal of Colloid and Interface Science*, *124*(1), 309–316.

Aziz, S. D., and S. Chandra (2000), Impact, recoil and splashing of molten metal droplets, *International Journal of Heat and Mass Transfer*, *43*(16), 2841–2857.

Batchelor, G. K. (2000), *An Introduction to Fluid Dynamics*, Cambridge University Press.

Bowden, F. P., and J. E. Field (1964), The brittle fracture of solids by liquid impact, *Proceedings of the Royal Society of London. Series A, Mathematical and Physical Sciences*, *282*(1390), 331–352.

Bremond, N., and E. Villermaux (2006), Atomization by jet impact, *Journal of Fluid Mechanics*, *549*, 273–306.

Brodie, H. J. (1975), *The Bird's Nest Fungi*, 80 pp., Toronto, Ontario: University of Toronto Press.

Chandra, S., and C. T. Avedisian (1991), On the collision of a droplet with a solid-surface, *Proceedings of the Royal Society of London Series a-Mathematical Physical and Engineering Sciences*, *432*(1884), 13–41.

Chandrasekhar, S. (1981), *Hydrodynamic and Hydromagnetic Stability*, Dover Publications.

Coppola, G., G. Rocco, and L. de Luca (2011), Insights on the impact of a plane drop on a thin liquid film, *Physics of Fluids*, *23*(2), 022,105.

Cossali, G. E., A. Coghe, and M. Marengo (1997), Impact of a single drop on a wetted solid surface, *Experiments in Fluids*, *22*(6), 463–472.

Cossali, G. E., G. Brunello, A. Coghe, and M. Marengo (1999), Impact of a single drop on a liquid film: experimental analysis and comparison with empirical model, *Italian Congress of Thermofluid Dynamics UIT, Ferrara, 30 June-2 July 1999*.

Cossali, G. E., M. Marengo, A. Coghe, and S. Zhdanov (2004), The role of time in single drop splash on thin film, *Experiments in Fluids*, *36*(6), 888–900.

Culick, F. E. C. (1960), Comments on a ruptured soap film, *Journal of Applied Physics*, *31*(6), 1128–1129.

Davidson, M. R. (2000), Boundary integral prediction of the spreading of an inviscid drop impacting on a solid surface, *Chemical Engineering Science*, *55*(6), 1159–1170.

Davidson, M. R. (2002), Spreading of an inviscid drop impacting on a liquid film, *Chemical Engineering Science*, *57*(17), 3639–3647.

Deegan, R. D., P. Brunet, and J. Eggers (2008), Complexities of splashing, *Nonlinearity*, *21*(1), C1–C11.

Driscoll, M. M., and S. R. Nagel (2011), Ultrafast interference imaging of air in splashing dynamics, *Phys. Rev. Lett.*, *107*.

Driscoll, T. A. (1996), Algorithm 756: A matlab toolbox for schwarz-christoffel mapping, *ACM Transcations on Mathematical Software*, *22*(2), 168–186.

Duchemin, L., and C. Josserand (2011), Curvature singularity and film-skating during drop impact, *Physics of Fluids*, *23*(9), iSI Document Delivery No.: 829YD Times Cited: 1 Cited Reference Count: 18 Duchemin, Laurent Josserand, Christophe Amer inst physics Melville.

Edgerton, H. E. (1977), *Stopping time: the photographs of Harold Edgerton*, Abrams, New York.

Edgerton, H. E., and J. R. Killian (1954), *Flash! Seeing the Unseen by Ultra-High-Speed Photography*, Branford, Boston.

Eggers, J., and E. Villermaux (2008), Physics of liquid jets, *Rep. Prog. Phys.*, *71*, 036,601.

Fezzaa, K., and Y. Wang (2008a), Ultrafast x-ray phase-contrast imaging of the initial coalescence phase of two water droplets, *Physical Review Letters*, *100*, 104,501, doi: 10.1103/PhysRevLett.100.104501.

Fezzaa, K., and Y. J. Wang (2008b), Ultrafast x-ray phase-contrast imaging of the initial coalescence phase of two water droplets, *Physical Review Letters*, *100*(10), 104,501.

Francois, S. P., and K. J. Mysels (1962), On the dimpling during the approach of two interfaces, *Phys. Chem.*, *66*, 190.

Frohn, A., and R. Roth (2000), *Dynamics of Droplets*, Springer-Verlag, Berlin.

Fujimoto, H., S. Ito, and I. Takezaki (2002), Experimental study of successive collision of two water droplets with a solid, *Experiments in Fluids*, *33*(3), 500–502.

Fullana, J. M., and S. Zaleski (1999), Stability of a growing end rim in a liquid sheet of uniform thickness, *Physics of Fluids*, *11*(5), 952–954.

Gentner, F., R. Rioboo, J. P. Baland, and J. De Coninck (2004), Low inertia impact dynamics for nanodrops, *Phys. Fluids*, *20*, 4748–55.

Gueyffier, D., and S. Zaleski (1998), Finger formation during droplet impact on a liquid film, *C.R. Acad. Sci., Ser. IIb: Mec., Phys., Chim., Astron*, *326*(12), 839–844.

Harlow, F. H., and J. P. Shannon (1967), The splash of a liquid drop, *J. Appl. Phys.*, *38*, 3855–3866.

Harlow, F. H., and J. E. Welch (1964), Numerical calculation of time dependent viscous incompressible flow of fluid with free surface, *Phys. Fluids*, *8*, 2182–2189.

Henrici, P. (1974), *Applied and Computational Complex Analysis*, John Wiley and Sons, New York.

Hirt, C. W., and B. D. Nichols (1981), Volume of fluid (vof) method for the dynamics of free boundaries, *Journal of computational physics*, *39*, 201–225.

Howison, S. D., J. R. Ockendon, J. M. Oliver, R. Purvis, and F. T. Smith (2005), Droplet impact on a thin fluid layer, *Journal of Fluid Mechanics*, *542*, 1–23.

Josserand, C., and S. Zaleski (2003), Droplet splashing on a thin liquid film, *Physics of Fluids*, *15*(6), 1650–1657.

Kadanoff, L. P. (2000), Making a splash, breaking a neck: the development of complexity in physical systems, *University of Chicago Record*, *35*, 2.

Keller, J. B., A. King, and L. Ting (1995), Blob formation, *Physics of Fluids*, *7*(1), 226–228.

Kelvin, L. (1871), Hydrokinetic solutions and observations, *Philosophical Magazine*, *42*, 362–77.

Kim, H. Y., and J. H. Chun (2001), The recoiling of liquid droplets upon collision with solid surfaces, *Phys. Fluids*, *13*, 643–59.

Kolinski, J. M., S. M. Rubinstein, S. Mandre, M. P. Brenner, D. A. Weitz, and L. Mahadevan (2012), Skating on a film of air: drops impacting on a surface, *Phys. Rev. Lett.*, *108*(7).

Krechetnikov, R. (2009), Rayleigh-taylor and richtmyer-meshkov instabilities of flat and curved interfaces, *Journal of Fluid Mechanics*, *625*, 387–410.

Krechetnikov, R. (2010), Stability of liquid sheet edges, *Physics of Fluids*, *22*, 092,101.

Krechetnikov, R., and G. M. Homsy (2009), Crown-forming instability phenomena in the drop splash problem, *J Colloid Interface Sci*, *331*(2), 555–9.

Lavergne, G., and B. Platet (1999), Droplet impingement on cold and wet wall, *Proc. 15th Ann. Conf. on Liquid Atomization and Spray Systems, Darmstadt*.

Lemmon, E. W., M. L. Huber, and M. O. McLinden (2010), *NIST standard reference database 23: Reference fluid thermodynamic and transport properties.*

Leng, L. J. (2001), Splash formation by spherical drops, *Journal of Fluid Mechanics*, *427*, 73–105.

Lesser, M. B. (1981), Analytic solutions of liqid-drop impact problems, *Proceedings of the Royal Society of London. Series A, Mathematical and Physical Sciences*, *377*, 289–308.

Lesser, M. B. (1983), The impact of compressible liquids, *Ann. Rev. Fluid Mech.*, *15*, 97–122.

Levin, Z., and P. V. Hobbs (1971), Splashing of water drops on solid and wetted surfaces - hydrodynamics and charge separation, *Philos. Trans. R. Soc. London, Ser. A*, *269*(1200), 555.

Mandre, S., M. Mani, and M. P. Brenner (2009), Precursors to splashing of liquid droplets on a solid surface, *Physical Review Letters*, *102*(13).

Mao, T., D. Kuhn, and H. Tran (1997), Spread and rebound of liquid droplets upon impact on flat surfaces, *AIChE J.*, *43*, 2169–79.

Maxwell, J. C. (1866), The bakerian lecture: On the viscosity or internal friction of air and other gases, *Phil. Trans. R. Soc. Lond.*, *156*, 249–268.

Mundo, C., M. Sommerfeld, and C. Tropea (1995), Droplet-wall collisions: experimental studies of the deformation and breakup process, *International Journal of Multiphase Flow*, *21*(2), 151–173.

Nikolopoulos, N., A. Theodorakakos, and G. Bergeles (2004), Normal impingement of a droplet onto a wall film: a numerical investigation, *Intenational Journal of Heat and Fluid Flow*, *26*(1), 119–132.

Oguz, H. N., and A. Prosperetti (1989), Surface-tension effects in the contact of liquid surfaces, *Journal of Fluid Mechanics*, *203*, 149–171.

Oguz, H. N., and A. Prosperetti (1990), Bubble entrainment by the impact of drops on liquid surfaces, *Journal of Fluid Mechanics*, *219*, 143–179.

Oguz, H. N., and A. Prosperetti (1993), Drop impact and the underwater noise of rain, *Natural Physical Sources of Underwater Sound*, pp. 669–682.

Okumura, K., F. Chevy, D. Richard, D. Quere, and C. Clanet (2003), Water spring: a model for bouncing drops, *Europhys. Lett.*, *62*, 237–43.

Pasandideh-Fard, M., Q. Y. M., S. Chandra, and J. Mostaghimi (1996), Capillary effects during droplet impact on a solid surface, *Phys. Fluids*, *8*, 650–59.

Pasandideh-Fard, M., S. D. Aziz, S. Chandra, and J. Mostaghimi (2001), Cooling effectiveness of a water drop impinging on a hot surface, *Int. J. Heat Fluid Flow*, *22*(2), 201–210.

Peregrine, D. H. (1981), The fascination of fluid-mechanics, *Journal of Fluid Mechanics*, *106*(MAY), 59–80.

Platikanov, D. (1964), Experimental investigation on the "dimpling" of thin liquid films, *J. Phys. Chem.*, *68*, 3619.

Range, K., and F. Feuillebois (1998), Influence of surface roughness on liquid drop impact, *J. Colloid Interface Sci.*, *203*, 16–30.

Rayleigh, L. (1878), On the instability of jets, *Proceedings of the London Math Society*, *4*, 10.

Rayleigh, L. (1883), Investigation of the character of the equilibrium of an incompressible heavy fluid of variable density, *Proceedings of the London Math Society*, *14*, 170–77.

Rein, M. (1993), Phenomena of liquid drop impact on solid and liquid surfaces, *Fluid Dynamics Research*, *12*(2), 61–93.

Rein, M. (2002), *Interactions between drops and hot surfaces. In Drop-Surface Interactions. CISM Courses and Lectures*, 456, Springer-Verlag, Vienna.

Reznik, S. N., and A. L. Yain (2002a), Spreading of a viscous drop due to gravity and capillarity on a horizontal or an inclined dry wall, *Phys. Fluids*, *14*, 118–32.

Reznik, S. N., and A. L. Yain (2002b), Strong squeezing flow between parallel plates leads to rolling motion at the contact line, *Int. J. Multiph. Flow*, *28*, 911–25.

Reznik, S. N., and A. L. Yain (2002c), Spreading of an axisymmetric viscous drop due to gravity and capillarity on a dry horizontal wall, *Int. J. Multiph. Flow*, *28*, 1437–57.

Richard, D., and D. Quere (2000), Bouncing water drops, *Europhys. Lett.*, *50*, 769–75.

Richtmyer, R. D. (1960), Taylor instability in shock acceleration of compressible fluids, *Communications on Pure and Applied Mathematics*, *13*, 297–319.

Rieber, M., and A. Frohn (1999), A numerical study on the mechanism of splashing, *Int. J. Heat Fluid Flow*, *20*(5), 455–461.

Rioboo, R., C. Tropea, and M. Marengo (2001), Outcomes from a drop impact on solid surfaces, *Atomization and Sprays*, pp. 155–65.

Rioboo, R., M. Marengo, and C. Tropea (2002), Time evolution of liquid drop impact onto solid, dry surfaces, *Experiments in Fluids*, *33*(1), 112–124.

Rioboo, R., C. Bauthier, J. Conti, M. Voue, and J. De Coninck (2003), Experimental investigation of splash and crown formation during single drop impact on wetted surfaces, *Experiments in Fluids*, *35*(6), 648–652.

Roisman, I. V., and C. Tropea (2002), Impact of a drop onto a wetted wall: Description of crown formation and propagation, *Journal of Fluid Mechanics*, *472*, 373–97.

Roisman, I. V., and C. Tropea (2005), Fluctuating flow in a liquid layer and secondary spary created by an impacting spray, *International Journal of Multiphase Flow*, *31*(179-200).

Roisman, I. V., B. Prunet-Forch, C. Tropea, and M. Vignes-Adler (2002), Multiple drop impact onto a dry solid substrate, *Journal of Colloid and Interface Science*, *256*, 396–410.

Roisman, I. V., T. Gambaryan-Roisman, O. Kyriopoulos, P. Stephan, and C. Tropea (2007), Breakup and atomization of a stretching crown, *Physical Review E*, *76*(2).

S., B., D. J., T. L., G. R., and M. B. (1997), A boundary element method for viscous gravity currents, *Int. J. Numer. Methods Fluids*, *25*.

Savva, N., and J. W. M. Bush (2009), Viscous sheet retraction, *Journal of Fluid Mechanics*, *626*, 211–240.

Scheller, B. L., and D. W. Bousfield (1995), Newtonian drop impact with a solid surface, *AIChE J*, *41*.

Schiaffino, S., and A. A. Sonin (1997), Molten droplet deposition and solidification at low weber numbers, *Phys. Fluids*, *9*.

Sikalo, S., H. D. Wilhelm, I. V. Roisman, S. Jakirlic, and C. Tropea (2005), Dynamic contact angle of spreading droplets: experiments and simulations, *Phys. Fluids*, *17*(062103).

Smith, F. T., L. Li, and G. X. Wu (2003), Air cushioning with a lubrication/inviscid balance, *J. Fluid Mech.*, *482*, 291–318.

Spillman, J. J. (1984), Spray impaction, retention and adhesion - an introduction to basic characteristics, *Pesticide Science*, *15*(2), 97–106.

Stow, C. D., and M. G. Hadfield (1981), An experimental investigation of fluid flow resulting from the impact of a water drop wth an unyielding dry surface, *Proc. R. Soc. Lond. A*, *373*, 419.

Stow, C. D., and R. D. Stainer (1977), The physical products of a splashing water drop, *Journal of the Meteorological Society of Japan*, *55*, 518.

Taylor, G. (1959), The dynamics of thin sheets of fluid. iii. disintegration of fluid sheets, *Proc. R. Soc. London, Ser. A*, *253*(1274), 313–321.

Taylor, G. I. (1950), The instability of liquid surfaces when accelerated in a direction perpendicular to their plane, *Proc. R. Soc. Lond.*, *A*(121), 192–196.

Thoraval, M. J., K. Takehara, T. G. Etoh, S. Popinet, P. Ray, C. Josserand, S. Zaleski, and S. T. Thoroddsen (2012), von karman vortex street within an impacting drop, *Physical Review Letters*, *108*(264506).

Thoroddsen, S. T. (2002), The ejecta sheet generated by the impact of a drop, *Journal of Fluid Mechanics*, *451*, 373–381.

Thoroddsen, S. T., and J. Sakakibara (1998), Evolution of the fingering pattern of an impacting drop, *Physics of Fluids*, *10*(6), 1359–1374.

Thoroddsen, S. T., T. G. Etoh, and K. Takehara (2003), Air entrapment under an impacting drop, *Journal of Fluid Mechanics*, *478*, 125–134.

Thoroddsen, S. T., M. J. Thoraval, K. Takehara, and T. G. Etoh (2011), Droplet splashing by a slingshot mechanism, *Physical Review Letters*, *106*(3).

Tritton, D. J. (1988), *Physical Fluid Dynamics*, Oxford University Press, USA.

Tropea, C., and I. V. Roisman (2000), Modeling of spray impact on solid surfaces, *Atomization Sprays*, *10*.

Trujillo, M. F., and C. F. Lee (2001), Modeling crown formation due to the splashing of a droplet, *Physics of Fluids*, *13*(9), 2503–2516.

Van Dam, D. B., and C. Le Clerc (2004), Experimental study of the impact of an ink-jet printed droplet on a solid substrate, *Phys. Fluids*, *16*(3403).

Van Der Veen, R. C. A., T. Tran, D. Lohse, and C. Sun (2012), Direct measurements of air layer profiles under impacting droplets using high-speed colour interferometry, *Phys. Rev E*, *85*(026315).

Vander Wal, R. L., G. M. Berger, and S. D. Mozes (2006), The splash/non-splash boundary upon a dry surface and thin fluid film, *Experiments in Fluids*, *40*(1), 53–59.

Wang, A.-B., and C.-C. Chen (2000), Splashing impact of a single drop onto very thin liquid films, *Physics of Fluids*, *12*(9), 2155–2158.

Wanninkhof, R., W. E. Asher, D. T. Ho, C. Sweeney, and W. R. McGillis (2009), Advances in quantifying air-sea gas exchange and environmental forcing, *Annual Review of Marine Science*, *1*, 213–244.

Weiss, D. A., and A. L. Yarin (1999), Single drop impact onto liquid films: neck distortion, jetting, tiny bubble entrainment, and crown formation, *Journal of Fluid Mechanics*, *385*, 229–254.

Wilkins, S. W., T. E. Gureyev, D. Gao, A. Pogany, and A. W. Stevenson (1996), Phase-contrast imaging using polychromatic hard x-rays, *Nature*, *384*, 335.

Worthington, A. M. (1879), On the spontaneous segmentation of a liquid annulus, *Proc. Phys. Soc. London*, *30*, 49–60.

Worthington, A. M. (1882), On impact with a liquid surface, *Proc. Phys. Soc. London*, *34*, 217–230.

Worthington, A. M. (1908), A study of splashes, *London: Longmans, Green*, p. 129.

Worthington, A. M., and R. S. Cole (1897), Impact with a liquid surface, studied by the aid of instantaneous photography, *Philos. Trans. R. Soc. London, Ser. A*, *189*, 137–148.

Xu, H., Y. Liu, P. He, and H. Wang (1998), The tar model for calculation of droplet/wall impingement, *J. Fluids Eng.*, *120*.

Xu, L. (2010), Instability development of a viscous liquid drop impacting a smooth substrate, *Physical Review E*, *82*(2).

Xu, L., W. W. Zhang, and S. R. Nagel (2005), Drop splashing on a dry smooth surface, *Physical Review Letters*, *94*, 184,505.

Yarin, A. L. (2006), Drop impact dynamics: Splashing, spreading, receding, bouncing, *Annual Review of Fluid Mechanics*, *38*, 159–192.

Yarin, A. L., and D. A. Weiss (1995), Impact of drops on solid-surfaces - self-similar capillary waves, and splashing as a new-type of kinematic discontinuity, *Journal of Fluid Mechanics*, *283*, 141–173.

Zhang, L. V., P. Brunet, J. Eggers, and R. D. Deegan (2010), Wavelength selection in the crown splash, *Physics of Fluids*, *22*(12), 122,105.

Zhang, L. V., J. Toole, K. Fezzaa, and R. D. Deegan (2012a), Evolution of the ejecta sheet from the impact of a drop with a deep pool, *Journal of Fluid Mechanics*, *690*, 5.

Zhang, L. V., J. Toole, K. Fezzaa, and R. D. Deegan (2012b), Splashing from drop impact into a deep pool:multiplicity of jets and the failure of conventional scaling, *Journal of Fluid Mechanics*, *703*, 402.

Zhao, H., A. Brunsvold, and S. T. Munkejord (2011), Investigation of droplets impinging on a deep pool: transition from coalescence to jetting, *Experiments in Fluids*, *50*, 621–635.